REPUBLIC OF TURKEY

ADANA SCIENCE AND TECHNOLOGY UNIVERSITY

GRADUATE SCHOOL OF NATURAL AND APPLIED SCIENCES

DEPARTMENT OF NANOTECHNOLOGY AND ENGINEERING SCIENCES

INVESTIGATION OF SOME PHYSICAL PROPERTIES OF Ga-DOPED AND (Ga-K)-CO-DOPED CdS THIN FILMS

SALTUK BUĞRA TÖRELİ

M. Sc. THESIS

Adana 2018

REPUBLIC OF TURKEY

GRADUATE SCHOOL OF NATURAL AND APPLIED SCIENCES

DEPARTMENT OF NANOTECHNOLOGY AND ENGINEERING SCIENCES

INVESTIGATION OF SOME PHYSICAL PROPERTIES OF Ga-DOPED AND (Ga-K)-CO-DOPED CdS THIN FILMS

Saltuk Buğra TÖRELİ

MASTER OF SCIENCE

SUPERVISOR

ASSOC. PROF. DR. Salih YILMAZ

Adana 2018

Approval of the Graduate School of Natural and Applied Sciences

Director

Assoc. Prof. Dr. Osman SİVRİKAYA

I certify that this thesis satisfies all the requirements as a thesis for the degree of Master of Science.

Chairman of the Department

Asst. Prof. Dr. Hatice İmge OKTAY BAŞEĞMEZ

This is to certify that I have read this thesis and that in my opinion it is fully adequate, in scope and quality, as a thesis for the degree of Master of Science.

Supervisor

Assoc. Prof. Dr. Salih YILMAZ

Adana Science and Technology University

Examining Committee Members

Asst. Prof. Dr. Mustafa AKYOL

Adana Science and Technology University

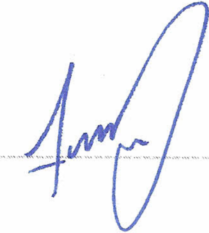

Asst. Prof. Dr. Mehmet Ali OLĞAR

Niğde Ömer Halisdemir University

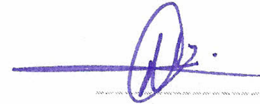

I hereby declare that presented materials and results in this document are original and I have strictly abided by the academic and ethical rules while preparing this thesis. I affirm that I have prepared this work by rules of the Thesis Writing Guideline of Graduate School of Natural and Applied Sciences. I also declare that except for the information known in general, I have properly submitted knowledge in this thesis by necessary citations.

Name and Surname: Saltuk Buğra TÖRELİ

Signature:

INVESTIGATION OF SOME PHYSICAL PROPERTIES OF Ga-DOPED AND (Ga-K)-CO-DOPED CdS THIN FILMS

TÖRELİ, Saltuk Buğra

M.Sc., in Nanotechnology and Engineering Sciences

May 2018, 75 pages

ABSTRACT

In this study, Ga-doped CdS thin films and (Ga-K)-co-doped CdS thin films were synthesized on glass slides via spray pyrolysis route and their structural, morphological, optical and electrical properties at different concentrations were investigated. A constant substrate temperature of 400 °C was selected for thin film growth process. As influences of 2 at.%, 4 at.%, 6 at.% and 8 at.% Ga concentrations on some physical properties of CdS thin films were examined, it was seen that better optical and electrical properties were obtained for 2 at.% Ga-doped CdS sample. Therefore, for all (Ga-K)-co-doped CdS thin films, Ga concentration was fixed to 2 at.%. However, the concentration level of K in CdS:Ga samples was increased from 1 at.% to 5 at.% in an increment of one percent in order to detect of influences of K on some physical properties of CdS:Ga thin films. It was confirmed that all the films had hexagonal wurtzite structure. The data also revealed that the preferred orientation was along (101) plane since it was the most intense peak. It was seen that a more uniform and smooth surface morphology was achieved after adding 5 at.% K content. The best optical transmission value, almost 85% transparency, was recorded in CdS:Ga thin films doped with 3 at.% and 4 at.% K levels. As a result of examining all the samples optically and electrically, it was deduced that 4 at.% K-doped CdS:Ga thin films are more suitable for optoelectronic applications.

Keywords: *Spray pyrolysis, CdS thin films, Ga-doping, (Ga-K)-co-doping, optical properties and electrical properties.*

Ga-KATKILI VE (Ga-K)-ÇİFT KATKILI CdS İNCE FİLMLERİN BAZI FİZİKSEL ÖZELLİKLERİNİN İNCELENMESİ

TÖRELİ, Saltuk Buğra

Yüksek Lisans Tezi, Nanoteknoloji ve Mühendislik Bilimleri

Mayıs 2018, 75 sayfa

ÖZET

Bu çalışmada, Ga-katkılı CdS ve (Ga-K) çift katkılı CdS ince filmleri kimyasal püskürtme yöntemi ile cam altlıklar üzerinde sentezlendi ve farklı konsantrasyonlarda, yapısal, morfolojik, optik ve elektriksel özellikleri incelendi. İnce film büyütme işlemi için 400 °C'lik sabit bir altlık sıcaklığı seçildi. %2, %4, %6 ve %8 Ga katkısının CdS ince filmleri üzerine etkisi incelendiğinde, %2 Ga katkılı CdS numunesi için daha iyi optik ve elektriksel özellikler elde edildiği görüldü. Bu nedenle, tüm (Ga-K) çift katkılı CdS ince filmleri için Ga katkısı %2'de sabit tutulmuştur. Bununla birlikte, K'nın CdS:Ga ince filmlerinin bazı fiziksel özellikleri üzerindeki etkilerini tespit etmek için, CdS:Ga numunelerindeki K konsantrasyonu seviyesi yüzde bir artışlar ile %1'den %5'e kadar arttırıldı. Tüm ince filmlerin hegzagonal wurtzit yapıda oldukları teyit edildi. Veriler ayrıca, en şiddetli pik olmasında ötürü tercihli yönelimin (101) düzlemi boyunca olduğunu ortaya koymuştur. %5 K içeriği ilave edildikten sonra daha düzgün ve pürüzsüz bir yüzey morfolojisinin elde edildiği görüldü. En iyi optik geçirgenlik değeri, yaklaşık %85 geçirgenlik, %3 ve %4 K seviyelerinde katkılanmış CdS:Ga ince filmlerinde kaydedildi. Örneklerin tümünün optik ve elektriksel olarak incelenmesi neticesinde, %4 K-katkılı CdS:Ga ince filmlerin optoelektronik uygulamalar için daha uygun olduğu sonucuna varılmıştır.

Anahtar Kelimeler: *Kimyasal püskürtme, CdS ince filmler, Ga-katkısı, (Ga-K)-çift katkısı, optik özellikler ve elektriksel özellikler.*

ACKNOWLEDGEMENTS

I would like to thank my supervisor, Assoc. Prof. Dr. Salih YILMAZ, for his advice and encouragement during the thesis. This work has been done with the help of his valuable guidance. I am also grateful for his constructive criticism and willing attitude provide my improvement in this arduous task. Additionally, I am very thankful for Assoc. Prof. Dr. İsmail POLAT, Prof. Dr. Emin BACAKSIZ and Assoc. Prof. Dr. Murat TOMAKİN due to their supports on sample preparation and experimental measurements in the thesis. In addition to their extensive scientific knowledge, they are also very polite persons. Lastly, I am sending a special thank to my parents, they supported me all the time within this period.

TABLE OF CONTENTS

ABSTRACT .... **i**

ÖZET .... **ii**

ACKNOWLEDGEMENTS .... **iii**

TABLE OF CONTENTS .... **iv**

LIST OF FIGURES .... **vii**

LIST OF TABLES .... **ix**

NOMENCLATURE .... **x**

CHAPTER 1 INTRODUCTION **1**

1.1 Brief History and Different Generations of Solar Cells 1

1.2 Fundamental Properties of Semiconductors 4

1.2.1 Intrinsic semiconductors 5

1.2.2 Extrinsic semiconductors 9

1.2.2.1 P-type semiconductors 9

1.2.2.2 N-type semiconductors 10

1.3 Energy Bands in Solids 11

1.3.1 Introduction 11

1.3.2 Donor and acceptor energy levels 13

1.3.3 Formation of energy bands in solids 14

1.3.4 Direct and indirect band gap materials 15

1.3.5 Fermi-Dirac distribution 16

1.3.6 Effective mass 18

1.4 Fundamental Properties of CdS Material 19

1.5 Objective of Research 20

CHAPTER 2 LITERATURE REVIEW **21**

CHAPTER 3 MATERIALS AND METHODS **28**

3.1 Spray Pyrolysis Deposition Technique 28

3.1.1 Introduction 28

3.1.2 Influence of spray parameters 28

3.1.2.1 Substrate temperature 29

3.1.2.2 Nozzle to substrate distance 29

3.1.3 Setup components 29

3.1.3.1 Nozzle 30

3.1.3.2 Substrate heater 30

3.1.3.3 Temperature controller 30

3.2 Preparation of Thin Films 31

3.2.1 Substrate cleaning process 31

3.2.2 Synthesis of CdS:Ga thin films 31

3.2.3 Synthesis of (Ga-K)-co-doped CdS thin films 31

3.3 Characterization Techniques 32

3.3.1 X-ray diffraction (XRD) 32

3.3.2 Scanning electron microscopy (SEM) 35

3.3.2.1 Components of SEM 36

3.3.2.2 Electron-material interaction 39

3.3.3 Energy dispersive X-ray spectroscopy (EDS) 41

3.3.4 Optical characterization 41

3.3.5 Electrical characterization 44

CHAPTER 4 RESULTS AND DISCUSSION 46

4.1 Investigation of Physical Properties of Ga-doped CdS Thin Films 46

4.1.1 XRD investigation of CdS:Ga thin films 46

4.1.2 SEM investigation of CdS:Ga thin films 48

4.1.3 EDS investigation of CdS:Ga thin films 49

4.1.4 Optical investigation of CdS:Ga thin films 51

4.1.5 Electrical investigation of CdS:Ga thin films 54

4.2 Investigation of Physical Properties of (Ga-K)-co-doped CdS Thin Films 55

4.2.1 XRD investigation of (Ga-K)-co-doped CdS thin films 55

4.2.2 SEM investigation of (Ga-K)-co-doped CdS thin films.................................... 58

4.2.3 EDS investigation of (Ga-K)-co-doped CdS thin films.................................... 59

4.2.4 Optical investigation of (Ga-K)-co-doped CdS fhin films 61

4.2.5 Electrical investigation of (Ga-K)-co-doped CdS thin films............................. 65

CHAPTER 5 CONCLUSIONS... 66

REFERENCES... 67

VITA.. 74

PUBLICATIONS 75

LIST OF FIGURES

Figure 1.1. a) A silicon atom with its four valence electrons. **b)** Silicon atoms make the covalent bonding with the neighboring silicon atoms. 7
Figure 1.2. Energy band diagram of an intrinsic semiconductor when the temperature is **a)** 0 K and **b)** higher than the 0 K. 8
Figure 1.3. a) A boron atom with its three valence electrons. **b)** Silicon atoms make the covalent bonding with the neighboring boron atom. 9
Figure 1.4. a) A phosphorus atom with its five valence electrons. **b)** Silicon atoms make the covalent bonding with the neighboring phosphorus atom. 10
Figure 1.5. Energy band diagram of **a)** conductor, **b)** semiconductor and **c)** insulator. ... 12
Figure 1.6. ε-k graph of a semiconductor. 12
Figure 1.7. a) Donor energy level in an n-type semiconductor. **b)** Acceptor energy level in a p-type semiconductor. 13
Figure 1.8. Illustration of the energy band formation in solids by considering the Si atoms. 14
Figure 1.9. Band diagram of a direct band gap material. 15
Figure 1.10. Band diagram of an indirect band gap material. 16
Figure 1.11. a) Schematic energy band diagram. The Fermi function versus energy plots in the case of **b)** T = 0 K **c)** T > 0 K and **d)** high temperatures. 17
Figure 1.12. Two crystal lattice structures of CdS. **a)** Cubic zinc blende structure. **b)** Hexagonal wurtzite structure. 19
Figure 3.1. Schematic diagram of the homemade spray pyrolysis system. 30
Figure 3.2. Schematic diagram of an X-ray tube. 33
Figure 3.3. Rigaku D/Max-IIIC diffractometer. 34
Figure 3.4. JEOL JSM-6610 SEM device equipped with the Oxford Instruments EDS. https://www.jeol.co.jp/en/products/detail/JSM-6610series.html. 36
Figure 3.5. Schematic diagram of an SEM device. 37
Figure 3.6. The signals arising after the interaction between the electron beam and sample. 40
Figure 3.7. SpectraMax M5 device. 43
Figure 3.8. Dongwoo Optron device. 43
Figure 3.9. Schematic of four point probe method. 44
Figure 4.1. XRD data of **a)** CdS, **b)** $Cd_{0.98}Ga_{0.02}S$, **c)** $Cd_{0.96}Ga_{0.04}S$, **d)** $Cd_{0.94}Ga_{0.06}S$ and **e)** $Cd_{0.92}Ga_{0.08}S$ thin films. 47

Figure 4.2. SEM images of **a)** CdS, **b)** $Cd_{0.98}Ga_{0.02}S$, **c)** $Cd_{0.96}Ga_{0.04}S$, **d)** $Cd_{0.94}Ga_{0.06}S$ and **e)** $Cd_{0.92}Ga_{0.08}S$ thin films. **f)** indicates 60° tilted view of $Cd_{0.96}Ga_{0.04}S$ sample. 49
Figure 4.3. EDS spectrum of $Cd_{0.94}Ga_{0.06}S$ sample. 50
Figure 4.4. Transmittance data of CdS and $Cd_{0.98}Ga_{0.02}S$, $Cd_{0.96}Ga_{0.04}S$, $Cd_{0.94}Ga_{0.06}S$, $Cd_{0.92}Ga_{0.08}S$ thin films. 51
Figure 4.5. Tauc's plot of CdS and $Cd_{0.98}Ga_{0.02}S$, $Cd_{0.96}Ga_{0.04}S$, $Cd_{0.94}Ga_{0.06}S$ and $Cd_{0.92}Ga_{0.08}S$ thin films. 52
Figure 4.6. RTPL data of CdS and $Cd_{0.98}Ga_{0.02}S$, $Cd_{0.96}Ga_{0.04}S$, $Cd_{0.94}Ga_{0.06}S$ and $Cd_{0.92}Ga_{0.08}S$ thin films. 54
Figure 4.7. XRD data of **a)** 1 at.% K-doped $Cd_{0.97}Ga_{0.02}S$, **b)** 2 at.% K-doped $Cd_{0.96}Ga_{0.02}S$, **c)** 3 at.% K-doped $Cd_{0.95}Ga_{0.02}S$, **d)** 4 at.% K-doped $Cd_{0.94}Ga_{0.02}S$, **e)** 5 at.% K-doped $Cd_{0.93}Ga_{0.02}S$ thin films. 56
Figure 4.8. SEM plain views of **a)** 1 at.% K-doped $Cd_{0.97}Ga_{0.02}S$, **b)** 2 at.% K-doped $Cd_{0.96}Ga_{0.02}S$, **c)** 3 at.% K-doped $Cd_{0.95}Ga_{0.02}S$, **d)** 4 at.% K-doped $Cd_{0.94}Ga_{0.02}S$, and **e)** 5 at.% K-doped $Cd_{0.93}Ga_{0.02}S$ thin films. 59
Figure 4.9. EDS spectrum of 4 at.% K-doped $Cd_{0.94}Ga_{0.02}S$ thin films. 60
Figure 4.10. a) SEM plan view of 4 at.% K-doped $Cd_{0.94}Ga_{0.02}S$ thin films including mapping of S, K, Ga and K elements on the surface, individual mapping results of **b)** S, **c)** K, **d)** Ga and **e)** Cd elements. 61
Figure 4.11. Transmission plots of 1 at.% K-doped $Cd_{0.97}Ga_{0.02}S$, 2 at.% K-doped $Cd_{0.96}Ga_{0.02}S$, 3 at.% K-doped $Cd_{0.95}Ga_{0.02}S$, 4 at.% K-doped $Cd_{0.94}Ga_{0.02}S$ and 5 at.% K-doped $Cd_{0.93}Ga_{0.02}S$ thin films. 62
Figure 4.12. Tauc's plot conclusions of 1 at.% K-doped $Cd_{0.97}Ga_{0.02}S$, 2 at.% K-doped $Cd_{0.96}Ga_{0.02}S$, 3 at.% K-doped $Cd_{0.95}Ga_{0.02}S$, 4 at.% K-doped $Cd_{0.94}Ga_{0.02}S$ and 5 at.% K-doped $Cd_{0.93}Ga_{0.02}S$ thin films. 63
Figure 4.13. RTPL graphs of 1 at.% K-doped $Cd_{0.97}Ga_{0.02}S$, 2 at.% K-doped $Cd_{0.96}Ga_{0.02}S$, 3 at.% K-doped $Cd_{0.95}Ga_{0.02}S$, 4 at.% K-doped $Cd_{0.94}Ga_{0.02}S$ and 5 at.% K-doped $Cd_{0.93}Ga_{0.02}S$ thin films. 64

LIST OF TABLES

Table 4.1. Lattice parameters (*a* and *c*) and the crystallite sizes of CdS, $Cd_{0.98}Ga_{0.02}S$, $Cd_{0.96}Ga_{0.04}S$, $Cd_{0.94}Ga_{0.06}S$, $Cd_{0.92}Ga_{0.08}S$ thin films. 48

Table 4.2. Actual atomic concentrations of Cd, S, and Ga elements in CdS and $Cd_{0.98}Ga_{0.02}S$, $Cd_{0.96}Ga_{0.04}S$, $Cd_{0.94}Ga_{0.06}S$, $Cd_{0.92}Ga_{0.08}S$ thin films. 50

Table 4.3. Carrier concentration and resistivity values of CdS and $Cd_{0.98}Ga_{0.02}S$, $Cd_{0.96}Ga_{0.04}S$, $Cd_{0.94}Ga_{0.06}S$, $Cd_{0.92}Ga_{0.08}S$ thin films. 55

Table 4.4. Lattice parameters, crystallite sizes and thicknesses of 1 at.% K-doped $Cd_{0.97}Ga_{0.02}S$, 2 at.% K-doped $Cd_{0.96}Ga_{0.02}S$, 3 at.% K-doped $Cd_{0.95}Ga_{0.02}S$, 4 at.% K-doped $Cd_{0.94}Ga_{0.02}S$ and 5 at.% K-doped $Cd_{0.93}Ga_{0.02}S$ thin films. 57

Table 4.5. Actual and nominal atomic contents of Cd, S, Ga, and K in 1 at.% K-doped $Cd_{0.97}Ga_{0.02}S$, 2 at.% K-doped $Cd_{0.96}Ga_{0.02}S$, 3 at.% K-doped $Cd_{0.95}Ga_{0.02}S$, 4 at.% K-doped $Cd_{0.94}Ga_{0.02}S$ and 5 at.% K-doped $Cd_{0.93}Ga_{0.02}S$ thin films. 60

Table 4.6. Carrier concentration and resistivity values of 1 at.% K-doped $Cd_{0.97}Ga_{0.02}S$, 2 at.% K-doped $Cd_{0.96}Ga_{0.02}S$, 3 at.% K-doped $Cd_{0.95}Ga_{0.02}S$, 4 at.% K-doped $Cd_{0.94}Ga_{0.02}S$ and 5 at.% K-doped $Cd_{0.93}Ga_{0.02}S$ thin films................................. 65

NOMENCLATURE

a, c	Lattice parameters
B	Magnetic field
D	Crystallite size
E	Energy of the electron
E_A	Acceptor energy level
E_D	Donor energy level
E_C	Energy level at the conduction band edge
E_V	Energy level at the valence band edge
E_F	Fermi energy level
E_G	Band gap
e	Electric charge
$f(\varepsilon)$	Fermi distribution function
$\hbar$	Reduced Planck’s constant
I	Electric current
K	Scherrer constant
k	Wave vector
k_B	Boltzman constant
m_0	Free electron mass
m_e	Mass of the electron
${m_e}^*$	Effective mass of the electron
${m_h}^*$	Effective mass of the hole
N_C	Effective density of states in conduction band
N_V	Effective density of states in valence band
n	Electron concentration
n_i	Electron density for intrinsic semiconductor
p	Hole concentration
p_i	Hole density for intrinsic semiconductor
T	Temperature
V	Potential difference
V_H	Hall voltage
$V(r)$	Potential energy
λ	Wavelength of the X-ray
β	Full width at half maximum
θ	Diffraction angle

μ Chemical potential

μ_e Electron mobility

μ_h Hole mobility

σ Electrical conductivity

σ_e Electrical conductivity due to electrons

σ_h Electrical conductivity due to holes

ρ Resistivity

CHAPTER 1 INTRODUCTION

1.1 Brief History and Different Generations of Solar Cells

Fossil fuels and nuclear power plants still continue to pollute our planet. Due to increasing world population and energy dependent electronic devices, the demand for the energy always is in an increasing trend. To tackle these problems and to find out the sources which are efficient, non-polluting and renewable properties, scientists and engineers have worked for years using such energy sources of sun, wind, water, geothermal and biomass. Among these, the sun could be a better choice because it provides a vast amount of energy to the Earth surface. It can be benefited from this tremendous solar energy in two ways, solar thermal and solar photovoltaic (PV). Furthermore, the solar panels which can be used to convert the energy of the sun to electricity are versatile in terms of mounting; they can be mounted on the land, roof or even water (sea, ocean, etc.).

PV technology actually has a long past in contrast to people's knowledge. The history started actually in 1839. In this time, physicist Alexandre Edmond Becquerel discovered the photovoltaic effect. According to this, when the two platinum electrodes in an electrically conducting solution (electrolyte) were exposed to the sunlight, an electric current was created. Therefore, he was the inventor of the first photovoltaic cell. However, this current was relatively weak and not practical for any purpose.

In the 1860s, physicist Augustin Mouchot invented the first parabolic trough solar collector. He thought that coal resources were finite and they would run out one day. However, as the revolution in transportation mechanism evolved, the coal price had fallen in time. As a result of the cheaper coal price, his work was seen as superfluous and the government withdrew the financial support of him.

Later, an electrical engineer Willoughby Smith observed photoconductivity of the element selenium (Se) in 1873. While he was working for a device which detected flaws in the underwater cable, he noticed that the performance of Se bars used in the device altered both at daytime and night. Then, he made some experiments with Se bars in the dark and light conditions. He realized that electrical resistance of Se depended on the amount of sunlight on which actually falling and it varied with changing of the light intensity. This was published as an article at the same year.

In 1883, Charles Edgar Fritts fabricated the world's first solar cell. The first layer consisted of a metal plate. On top of it, there was a thin film layer of Se. Fritt coated the Se layer with the thin film of gold to complete the solar cell. The efficiency of this cell was less than 1% (Fraas and Partain, 2010).

Heinrich Hertz discovered then the photoelectric effect during in an experiment in 1887. When a metal surface was exposed to an ultraviolet light, it would bring about the escapes of electrons from the surface of the metal. He observed that there was an unexplained interaction between light and matter in terms of classical physics.

This mystery was solved in 1905. Einstein published a paper which explained the photoelectric effect mathematically. He submitted that light was composed of discrete packets of energy so-called light quanta, at the present time known as photons.

A long-time later, an American engineer Russell Shoemaker Ohl made an outstanding discovery in 1940 at the Bell Laboratories. He discerned that among the silicon (Si) samples, only the Si wafer which cracked from the middle produced a current when sunlight were falledon it, but other samples didn't produce. This situation could be explained as follows: the impurity quantities were different on the one side of the cracked Si sample than that ofthe other side. After the division of sample into two regions because of the crack, positively and negatively doped sides were formed. It was basically a p-n junction and different charges created an electric field between these sides. To provide the current flow on the cell, the circuit was completed after the creation of electric field. This solar cell had almost 1% efficiency (Pandey et al., 2015) and it was a sign of the upcoming success.

In 1954, the first modern solar cell based on the Si, monocrystalline (mono c-Si), was invented by three scientists at the Bell Laboratories. It was a milestone in the history of PV and this cell had nearly 6% efficiency (Chapin et al., 1954). This efficiency was practical in order to supply the energy into the panels at satellites, for instance. It can be said that the generations of solar technology started with this development.

There are three generations of solar cells. The first generation solar cells (FGSCs) which are also called traditional solar cells are the oldest solar cell technology and are manufactured from the crystalline Si wafers. The types of Si are either mono c-Si or multicrystalline (mc-Si) in this generation. While a mono c-Si cell is manufactured from the single Si crystal, a mc-Si cell is composed of different crystals of Si being fused. According to laboratory results, mono c-Si cells had slightly better efficiency value, 25.8% (Richter et al., 2017), than the mc-Si cells, 22.3% (Benick et al., 2017), since the ultra high purity Si (99.9%) was used in mono c-Si cells. But this makes them more expensive because hard and complex manufacture processes (Czochralski process) cause the waste of high amounts of Si. However, mc-Si is frequently used more in PV panels because they are high efficiency. Also, their production cost is low in contrast to mono c-Si since the mc-Si panels are produced with a casting process by following some steps instead of using the Czochralski process. These are melting of raw silicon first, then pouring into a square mold,

cooling and slowly solidifying them and lastly cutting them as square wafers. However, one drawback of mono c-Si based solar cells is degradation in efficiency at the high temperatures. A major disadvantage for the FGSCs is the wasting of most of the photon energy as heat. Today, the FGSCs overwhelmingly dominate the PV market due to their broad spectral absorption range, high conversion efficiencies, high carrier mobility, stability, reliability and long life span.

The second generation solar cells (SGSCs), also known as thin film (TF) solar cells, composed of the layers with several micrometers in thickness and are mostly made from the amorphous silicon (a-Si). Besides that, the compound semiconductors of cadmium telluride (CdTe), copper indium diselenide (CIS), copper indium gallium diselenide (CIGS) and Cu_2ZnSnS_4 (CZTS) are the other materials being used. TF based solar cells have the limited stability and exhibit lower performances than those of FGSCs. However, they are inexpensive, unlike the Si-based solar cells, due to the lower material consumption. Up to research-cell efficiency values of 22.1% and 22.6% were achieved for CdTe and CIGS solar cells (Green et al., 2018), respectively, showing near values to those of c-Si cells. CdTe solar cells are the second solar cell technology which is used most commonly after Si-based technologies. That means that it is the most frequently utilized material in TF technology. CdTe solar cells have the low cost advantage for the cell production. The problems with these type of solar cells are that cadmium (Cd) is a toxic and heavy metal and telluride (Te) is a scarce material. The maximum theoretical efficiency for CZTS material is 32.4% (Shockley and Queisser, 1961). So far, the maximum efficiency of CZTS cell obtained by using only S was 9.2% while the maximum efficiency of CZTSSe cell attained by using S and Se together was 12.6%. On the other side, the efficiency of 14.0% was reported for a-Si solar cells (Sai et al., 2015). Due to the relatively low efficiencies of them, they are used in low-power consuming electronic devices like a pocket calculator. TF solar modules can be manufactured as flexible since considerably thin layers of material are used. Therefore, they are applicable to many different surfaces. The main effort behind the second generation technology was to reduce the cost at the first generation.

The third generation solar cells (TGSCs) are based on both organic and inorganic materials like polymers, small molecules, Si, etc. For instance, nanocrystal solar cells, photoelectrochemical cells, polymer-based solar cells, dye-sensitized solar cells are in this category. Highly efficient but expensive multi-junction solar cells (MJSCs) are also regarded within this generation. These cells possess the topmost laboratory-based efficiency (46% for four-junction or more cells) (Green et al., 2018) when compared with the efficiencies of the other cells. The idea behind the MJSCs is simple. It cannot be benefited from all incoming electromagnetic energy in the visible region via the other solar cell technologies

since there are one or several layers designed as collecting only a specific and small portion of the solar spectrum. But in case of MJSCs, there are layers which consist of different band gap semiconductors. These are optimized to gather more photons, from the energy level of low to high, which means a broad spectrum. As a result of the increase in the photon absorption with different layers, photon conversion increases and hence this causes to enhance the overall efficiencyof the cells. However, the stability and performance of TGSCs are generally not good as in those of FGSCs and SGSCs. The main concept in TG is to improve the utilization of incoming photons more efficiently than those of FGSCs and SGSCs by reducing the production costs.

1.2 Fundamental Properties of Semiconductors

Materials are classified as conductors, semiconductors and insulators according to their electrical conductivity. Semiconductors are solid materials that have unique properties and an incredible influence on the development of novel electronic devices. Many electric appliances of today contain them as integrated. In general terms, semiconductors are materials which have an electrical conductivity level somewhere between conductors and insulators. The name of the semiconductor is originated from this intermediate level of electrical conductivity. In other definition of this term can be explained according to the energy band model. They behave as an insulator at absolute zero temperature (at T = 0K) because the valence band is full of electrons but the conduction band is completely empty due to the low temperature (Kelsall et al., 2005). Above the zero Kelvin, however, the valence band is filled nearly while the conduction band is filled partially. The gap that separates the valence band from conduction band is called forbidden energy gap. In conductors, these two bands overlap. Therefore, the promotion of the electrons to conduction band is simple. In semiconductors, the band gap (E_G) is typically smaller than 4 eV and for many semiconductors, it is in the order of 1 eV, but, insulators have a relatively large energy gap, usually bigger than 4 eV (Yu et al., 2010). Hence, the electrons in the valence band cannot easily cross such a large energy barrier and require a quite high energy to pass it. This explains the reason for poor electrical conductivity in insulators.

For conducting materials, the electrical resistivities are in the order of 10^{-6} Ω.cm and for insulators, above 10^{14} Ω.cm (Kittel, 2005). As for the semiconducting materials, it is in the range of 10^{-2}-10^{9} Ω.cm (Kittel, 2005). Also, the electrical conductivity of a semiconductor can be changed in several ways; for example with altering the temperature, applying an electric field and adding impurities.

Semiconductors are either in elemental and compound type. The well-known elements belonging the group IV of the periodic table such as Si, germanium (Ge), diamond (C) and grey tin (Sn) are termed as elemental semiconductors. The compound semiconductors can be binary, ternary and quaternary. III-V binary compounds are formed with the combination of group III elements like boron (B), aluminium (Al), gallium (Ga), indium (In) with group V elements like (nitrogen) N, phosphorus (P), arsenic (As), antimony (Sb). Aluminium arsenide (AlAs), boron nitride (BN), gallium arsenide (GaAs) and gallium nitride (GaN) can be given as examples.

Semiconductor materials are divided into two main groups depending on their purity. These are intrinsic and extrinsic.

1.2.1 Intrinsic semiconductors

Intrinsic type of semiconductor is chemically very pure, that means there are almost no impurities in solid, and the semiconducting property is naturally presented. It is named sometimes undoped semiconductor besides of the term of pure semiconductor. Si, Ge, C, and Sn are in this category.

An intrinsic semiconductor exhibits a low electrical conductivity because there are no or rather few free charge carriers within it for the conduction. These charge carriers in semiconductors are both electrons and holes. Actually, a hole represents the opposite charge of the electron, meaning the deficit of electron. In an intrinsic semiconductor, the density of electrons equals the density of holes $(n_i = p_i)$ since the transition of an electron from the valence band to the conduction band after a thermal excitation leaves a hole in the valence band and this causes an equality in charge carrier numbers.

The electrical conductivity of intrinsic semiconductors is temperature dependent. At T = 0 K temperature, pure semiconductors don't convey the electric current. As the temperature is increased, atoms gain energy and hence, the increase in the vibration amplitudes around the equilibrium positions, some bonds break so that electrons pass to the conduction band and become free. The thermal energy at any temperature is measured by $k_B T$. Since $\mathrm{k_B T}$ is low at room temperature (only 0.026 eV), generated electron and hole densities are small in semiconductors. Therefore, thermal treatment at room temperature is not sufficient for the conduction and it is necessary to be risen up to the higher temperatures. If we make only thermal treatment, since the energy gap is relatively large in some crystals, the semiconductor has to be heated excessively up due to its relatively small $\mathrm{k_B T}$ value. For instance, a material which has a forbidden energy gap of 4 eV $(E_G = 4\ eV)$ has to be heated

to a very high temperature. By that way, its own electrons are able to be stimulated and can overcome the energy gap.

Assumed band gap value is

$$E_G = 4\ eV \tag{1.1}$$

and the thermal energy must equal at least to the band gap of the material

$$k_B T \geq E_G \tag{1.2}$$

where k_B is Boltzmann constant and equals to 8.617330 x 10^{-5} eV.K^{-1}, T is the temperature in Kelvin and so, T is founded as

$$T \cong 46.418\ K \tag{1.3}$$

However, materials cannot withstand such a high temperature. For this reason, introducing of impurity atoms into the material is performed to solve the problem. Thus, the electrons can be promoted from valence band to conduction band.

To exemplify the intrinsic semiconductor, let's consider a Si atom. The electronic configuration of Si atom is

$$Si:\ 1s^2 2s^2 2p^6 3s^2 3p^2 \tag{1.4}$$

and the valence electrons are extremely important due to being responsible for the electrical conductivity of semiconductors. It is easily seen each Si atom has four valence electrons in the outermost shell. They complete their outermost shells by making covalent bonding with neighboring Si atoms in order to attain a stable electron configuration and form a solid crystal structure. After sharing the electrons of adjacent Si atoms, a Si atom thus has a

stable noble gas structure with its eight valence electrons. The valence band becomes full of electrons hereafter and since all the valence electrons are bonded firmly due to covalent bonds, there are no free electrons remaining that can contribute to electrical conductivity. This situation is true for the absolute zero temperature. Figure 1.1 shows the Si atoms which make the covalent bonding.

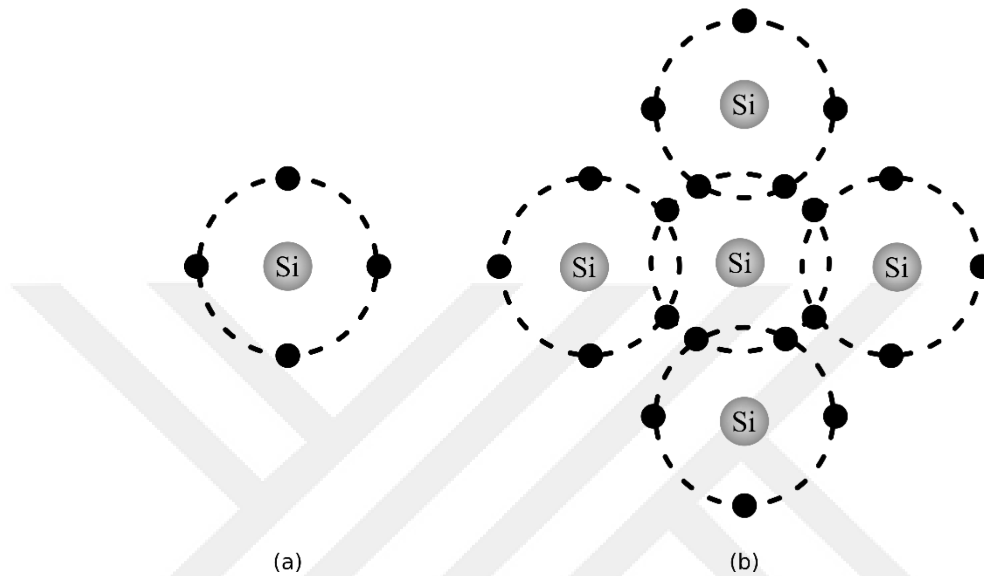

Figure 1.1. a) A silicon atom with its four valence electrons. **b)** Silicon atoms make the covalent bonding with the neighboring silicon atoms.

However, covalent bonds start to break above the zero Kelvin and some electrons are able to surpass the forbidden gap of Si (band gap for Si is 1.1 eV) and begin to jump from valence band to the conduction band. Such situation is demonstrated in Figure 1.2. These electrons are called as conduction electrons and are crucial in terms of their roles playing in semiconductor devices; they can easily move in the crystal and it causes an electrical conductivity as these electrons can carry the electrical currents. Yet, it is not enough for potential applications. To be able to obtain more electrical conductivity with Si atoms, the crystal structure is deliberately doped with suitable impurity atoms which distort the pure structure.

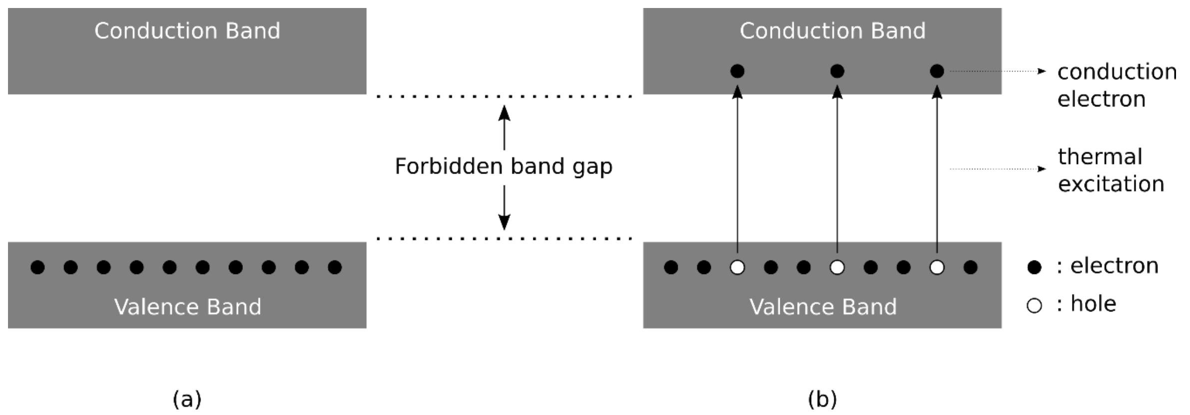

Figure 1.2. Energy band diagram of an intrinsic semiconductor when the temperature is **a)** 0 K and **b)** higher than the 0 K.

For intrinsic semiconductors, electron and hole concentrations are formulated by

$$n_i = p_i = (N_C N_V)^{1/2} e^{\left(\frac{-E_G}{2k_B T}\right)} \tag{1.5}$$

where

$$N_C = 2\left(\frac{2\pi m_e k_B T}{h^2}\right)^{\frac{3}{2}} \text{ and } N_V = 2\left(\frac{2\pi m_h k_B T}{h^2}\right)^{\frac{3}{2}} \tag{1.6}$$

where N_C is the effective number of levels per unit volume in conduction band, N_V is the effective number of levels per unit volume in valence band, m_e and m_h is the effective mass of an electron and a hole, respectively.

With the conductivity resulting from electrons ($\sigma_e = ne\mu_e$) and holes ($\sigma_h = pe\mu_h$), the electrical conductivity of intrinsic semiconductors (σ) is calculated in the following manner

$$\sigma = \sigma_e + \sigma_h = ne\mu_e + pe\mu_h \tag{1.7}$$

where n and p are concentration of electrons and holes respectively, μ_e and μ_h are electron and hole mobilities respectively and e is the electric charge.

1.2.2 Extrinsic semiconductors

Once foreign atoms are incorporated into an intrinsic semiconductor it transforms to an extrinsic semiconductor. Most semiconductors used in the modern devices are extrinsic. This is because electrical and optical properties of pure semiconductors can be readily controlled in desired level by modifying their purity.

To dope pure semiconductors with III or V group elements from periodic table allows increase the electrical conductivity. It is sufficient to add the impurity atoms in very small quantities to affect the electrical conductivity remarkably. This adding process is called as doping and added atoms are called as dopant impurities. Both electrons and holes are current carriers in semiconductors and their concentrations can be changed after the doping process.

Two types of extrinsic semiconductors can be manufactured by doping of group IV elements with suitable dopants. These are p-type and n-type semiconductors.

1.2.2.1 P-type semiconductors

P-type semiconductor formation is illustrated in Figure 1.3.

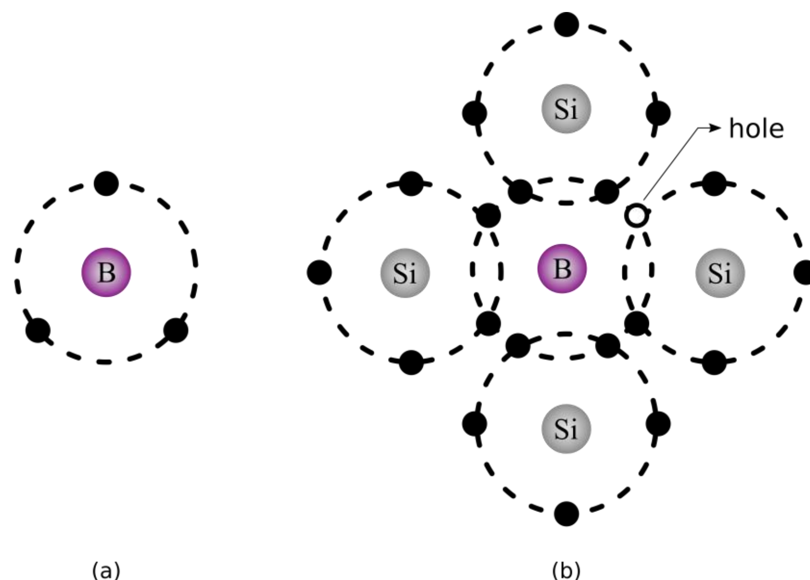

Figure 1.3. a) A boron atom with its three valence electrons. **b)** Silicon atoms make the covalent bonding with the neighboring boron atom.

When a trivalent atom like B, Al, Ga, etc. is incorporated into a Si atom or a Ge atom, a hole is formed inasmuch as there is only three valence electrons of the trivalent elements while Si or Ge has four valence electrons. That is, these three valence electrons of group III element make covalent bonds with these three of four electrons of group IV element.

Even if dopant atoms (acceptor atoms) are added as a slight quantity, hole concentration surpasses the electron concentration notably $(p \gg n)$. Hence, holes become majority carriers in a p-type semiconductor while electrons are minority carriers. An electron can be easily accepted from valence band to the acceptor energy level E_A.

A p-type semiconductor is created by this way and due to outnumbering of the holes, contributions of electrons to electrical conductivity are ignored. Thus, electrical conductivity is determined as following

$$\sigma = pe\mu_h \tag{1.8}$$

1.2.2.2 N-type semiconductors

N-type semiconductor formation is illustrated in Figure 1.4.

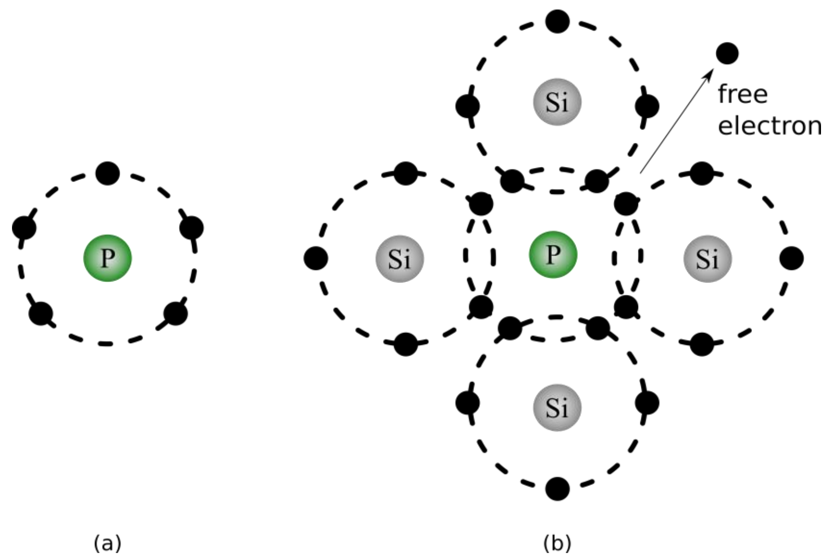

Figure 1.4. a) A phosphorus atom with its five valence electrons. **b)** Silicon atoms make the covalent bonding with the neighboring phosphorus atom.

When a pentavalent atom like P, As, Sb, etc. is added to a Si atom or a Ge atom, one electron becomes free since Si has four valence electrons while a pentavalent atom has five valence electrons. That is, these four valence electrons of a group IV element make covalent bonds with these four of five valence electrons of a group V element. This extra electron is loosely bound to their host atom and a small thermal energy is sufficient to promote it from the donor energy level E_D to the conduction band. In conclusion, this electron can move freely within the crystal and contributes to the electrical conductivity.

If dopant atoms (donor atoms) are added slightly, electron concentration outnumbers the hole concentration $(n \gg p)$ and an n-type semiconductor is created. The electrons are majority carriers in a n-type semiconductor while holes are minority carriers.

By virtue of outnumbering of the electrons, contributions of the holes to electrical conductivity are ignored. Therefore, electrical conductivity is determined as follows

$$\sigma = ne\mu_e \tag{1.9}$$

1.3 Energy Bands in Solids

1.3.1 Introduction

The electrical and optical properties of materials are closely related to the electronic band structure of the materials (Gluszak, 1996). Energy bands can be considered as a great number of closely and largely located energy levels. If these bands are fully occupied or completely empty, the crystal acts as an insulator. The reason is that when the electric field is applied, electrons cannot move because there are no unoccupied states for the electrons in the band.

The energy band diagrams that play an vital role in classifying the materials as conductor, semiconductor, and insulator are shown in Figure 1.5.

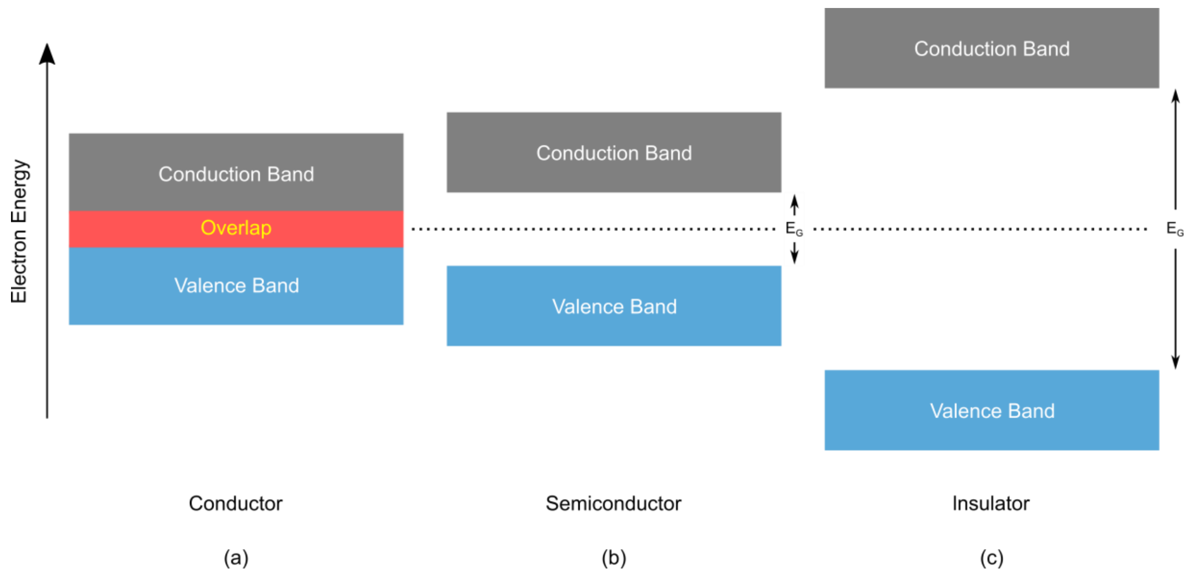

Figure 1.5. Energy band diagram of **a)** conductor, **b)** semiconductor and **c)** insulator.

The band gap in semiconductors is an energy range between the maximum of the valence band and the minimum of the conduction band and signifies that electrons cannot exist in this energy gap.

The energy-dispersive curve, (ε-k) for a semiconductor is shown in Figure 1.6.

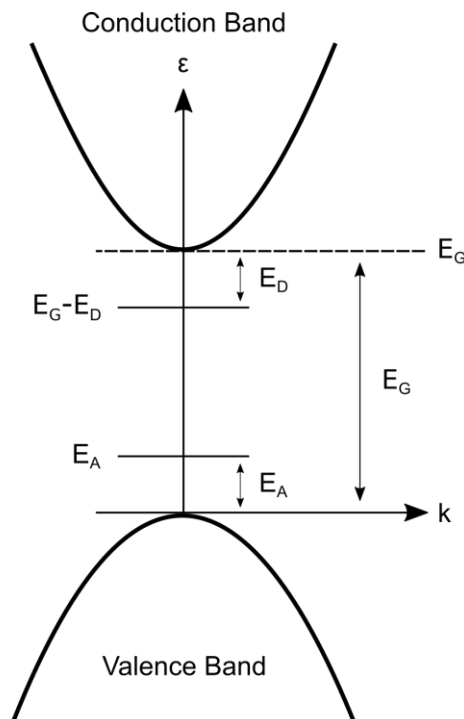

Figure 1.6. ε-k graph of a semiconductor.

Energy-momentum relation for electrons in the conduction band is

$$\varepsilon = E_G + \frac{\hbar^2 k^2}{2m_e} \tag{1.10}$$

and for holes in the valence band is

$$\varepsilon = -\frac{\hbar^2 k^2}{2m_h} \tag{1.11}$$

1.3.2 Donor and acceptor energy levels

When an electron which is loosely bounded to the donor atom gets a sufficient amount of energy (donor ionization energy), it becomes completely free by jumping the conduction band. This energy is expressed as E_D.

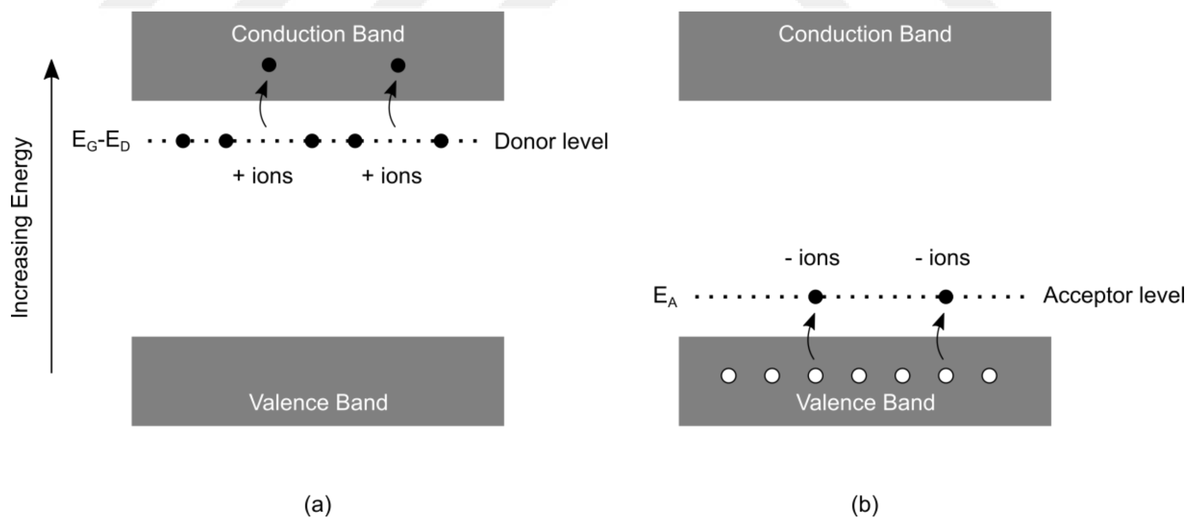

Figure 1.7. a) Donor energy level in an n-type semiconductor. **b)** Acceptor energy level in a p-type semiconductor.

On the other hand, deficient of the acceptor atom can be completed by receiving an electron from the valence band and this energy difference (E_A) is termed as acceptor ionization energy. The donor and acceptor energy levels can be seen in Figure 1.7.

1.3.3 Formation of energy bands in solids

The band formation in semiconductors can be explained simply by considering an isolated Si atom. The Si atom has two electrons in 3s subshell and two electrons in 3p subshell. When another Si atom comes to near the Si atom, 3s and 3p energy states are split into two levels seen in the Figure 1.8 due to the requirement of Pauli exclusion principle. Unlike the other subshells (2s and 2p), these 3s and 3p subshells belong to both of the Si atoms.

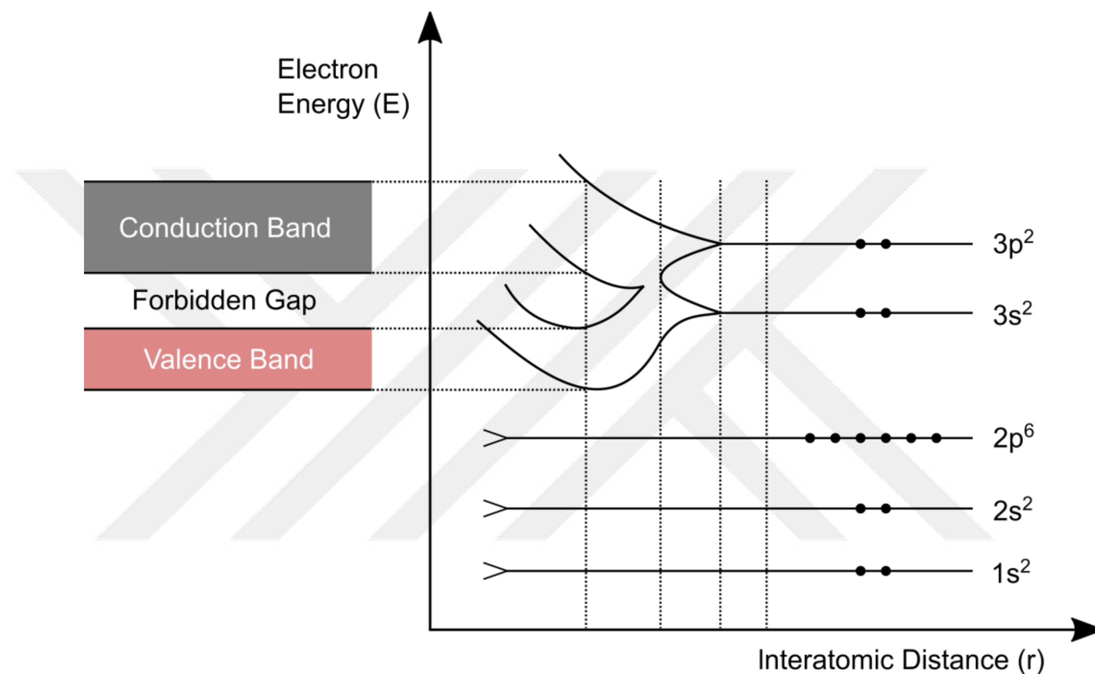

Figure 1.8. Illustration of the energy band formation in solids by considering the Si atoms.

When the number of Si atoms ascends, 3s and 3p orbital energies are split as the number of atoms as and these energy states possess all Si atoms. Moreover, as the number of atoms coming together increases (crystal formation), s and p orbitals are split up to the Avogadro's number, that is, the bands overlap at first and then separate. Eventually, continuous energy bands including the discrete energy levels are generated. It is noted that the electrons should be considered as a part of the whole crystal instead of thinking of them as part of atoms. The region between the energy bands formed by splitting of s and p (and also upper bands if exist) orbitals is forbidden energy gap where electrons cannot be found. The further splitting of the energy bands for Si atoms is seen in Figure 1.8.

Band structure of semiconducting materials is divided into direct and indirect band gap categories and type of it determines the optical properties of a semiconductor.

1.3.4 Direct and indirect band gap materials

Direct band gap semiconductors are semiconductors in which the maximum of the valence band and the minimum of the conduction band lie in same k-value $(k = 0)$ and the band structure of a direct band gap material is demonstrated in Figure 1.9. GaAs, InAs, InP, InN, etc. are examples of the direct band gap semiconductors. The momentum is conserved in the direct transition at the stage of both promotion and recombination processes of an electron. E_C and E_V are conduction band edge and valence band edge, respectively.

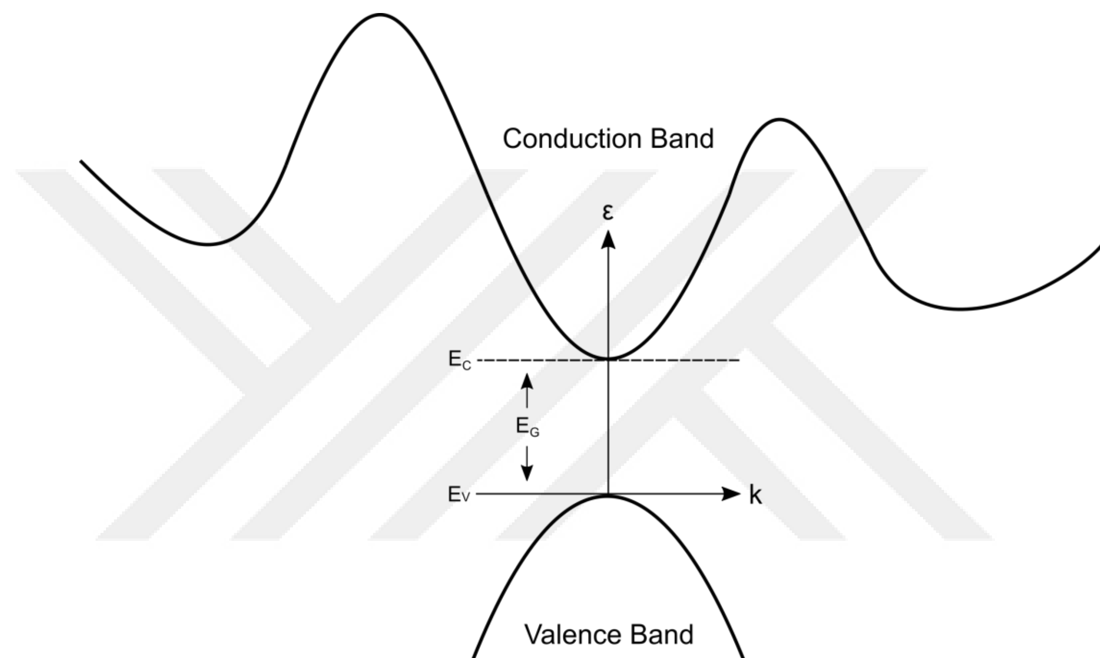

Figure 1.9. Band diagram of a direct band gap material.

Indirect band gap semiconductors are semiconductors in which the maximum of the valence band and the minimum of the conduction band lie in different k-values $(k \neq 0)$. The band structure of an indirect band gap material is demonstrated in Figure 1.10. The elemental semiconductors Si and Ge are the examples of indirect band gap materials. On the other hand, to the compounds, AlAs, etc. can be given. Momentum must also be conserved in the indirect transition. To satisfy the conservation of momentum law, it is necessary the accompanying of the phonons. During the process, energy is lost as heat generally (Gluszak, 1996) and therefore, indirect band gap semiconductors are not preferable for optoelectronic applications.

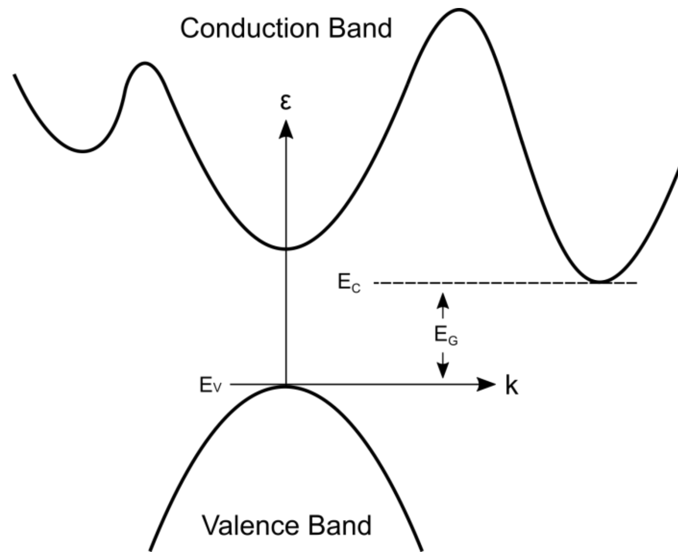

Figure 1.10. Band diagram of an indirect band gap material.

1.3.5 Fermi-Dirac distribution

Fermions like electron and proton comply with the Fermi-Dirac statistic. Since they obey the Pauli exclusion principle, two fermions cannot be found at the same quantum state in an atom (Gluszak, 1996). Therefore, they occupy first to start to fill the orbitals from the lowest available energy levels. The distribution function for the fermions is

$$f(\varepsilon) = \frac{1}{e^{\varepsilon - \mu / k_B T} + 1} \tag{1.12}$$

where ε is energy and μ is chemical potential in here. $f(\varepsilon)$ gives the occupation probability of a state at the ε energy level by a fermion at the temperature T in a thermal equilibrium and this value ranges between 0 and 1. Temperature-dependent Fermi function graphs are demonstrated by Figure 1.11.

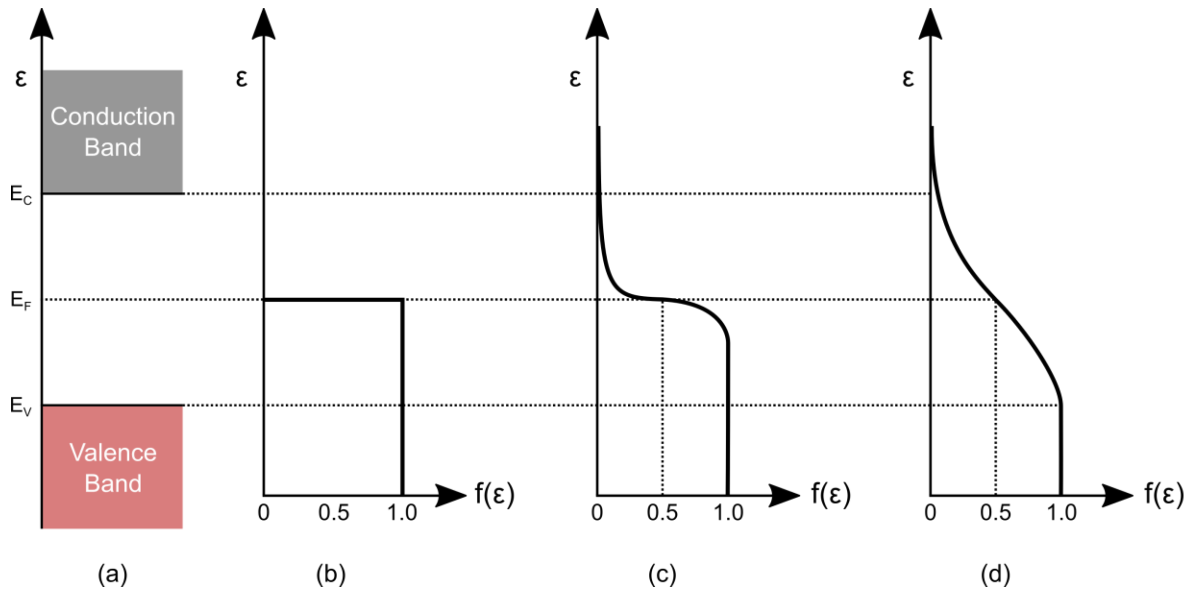

Figure 1.11. a) Schematic energy band diagram. The Fermi function versus energy plots in the case of **b)** T = 0 K **c)** T > 0 K and **d)** high temperatures.

In the case of $\varepsilon = E_F$, the probability of an electron that occupies an energy state at the Fermi level is $1/2$ regardless of the temperature T.

At absolute zero, it is a step function. All the available energy states up to E_F are filled by electrons, which means that the occupation of the electrons is certain and they cannot find above the E_F.

When the temperature is nearly 0 K and in the case of $\varepsilon - \mu \gg k_B T$, the probability of an electron that occupies an energy state above the Fermi level approaches to 0 and is expressed with the following approximation

$$f(\varepsilon) \approx e^{(\mu-\varepsilon)/k_B T} \tag{1.13}$$

Yet, in the case of $\varepsilon - \mu \ll k_B T$, the probability of an electron that occupies an energy state below the Fermi level is approaches to 1 and can be estimated with following approximation

$$f(\varepsilon) \approx 1 - e^{(\varepsilon-\mu)/k_B T} \tag{1.14}$$

As the temperature rises, more electrons are excited and occupation probability of electrons at the energy states below the Fermi level starts to decrease since some electrons can jump the energy barrier.

1.3.6 Effective mass

The electrons and holes in the crystal are not completely free. Even if it is a weak interaction, electrons and holes interact with the charged ions in the crystal (Gluszak, 1996). Therefore, they have potential energy besides the kinetic energy. Unlike the free particles, it is hard to describe mathematically the particles which have potential energy. The effective mass concept is used for simplicity and both electrons and holes are considered as particles having different masses from their free cases.

In solids, the effective mass depends on the energy and wave vector. It can be used to determine the band structure of solids. The behavior of the electrons in the crystal is stated in terms of a wave equation known as Schrödinger wave equation by

$$-\frac{\hbar}{2m_0}\nabla^2 ¥ + V(r)¥ = E¥ \qquad (1.15)$$

where $\hbar$, m_0, $V(r)$ and E are respectively, reduced Planck constant, free electron mass, potential energy and energy of electron, respectively.

In the crystal, the effective mass of electrons is

$$m_e{}^* = \frac{\hbar^2}{\left(\frac{\partial^2 E_C}{\partial k^2}\right)} \qquad (1.16)$$

and the effective mass of holes is

$$m_h{}^* = \frac{\hbar^2}{\left(\frac{\partial^2 E_V}{\partial k^2}\right)} \qquad (1.17)$$

1.4 Fundamental Properties of CdS Material

II-VI binary compounds are formed with combinations of group II and IV elements. zinc oxide (ZnO), zinc sulfide (ZnS), cadmium sulfide (CdS) and CdTe are some common examples. Depending on the thermodynamic parameters, group II-VI compounds can crystallize in two phases; cubic zinc blende and for many of them; hexagonal wurtzite structure (Adachi, 2005). The common crystal structures of the CdS are zinc blende and wurtzite phases. It is attainable to zinc blende structure of CdS at the room temperature while its wurtzite structure can be reached in the case of higher temperatures (Khallaf et al., 2009a) and mostly, CdS crystallizes in form of the hexagonal wurtzite structure. In terms of thermodynamic point of view, the wurtzite structure is most stable form (Hodes, 2002). On the other hand, the zinc blende is a metastable state at room temperature. The two crystal structures of the CdS are given in Figure 1.12. The hexagonal wurtzite CdS thin films are more preferable for the solar cell applications (Lee, 2004).

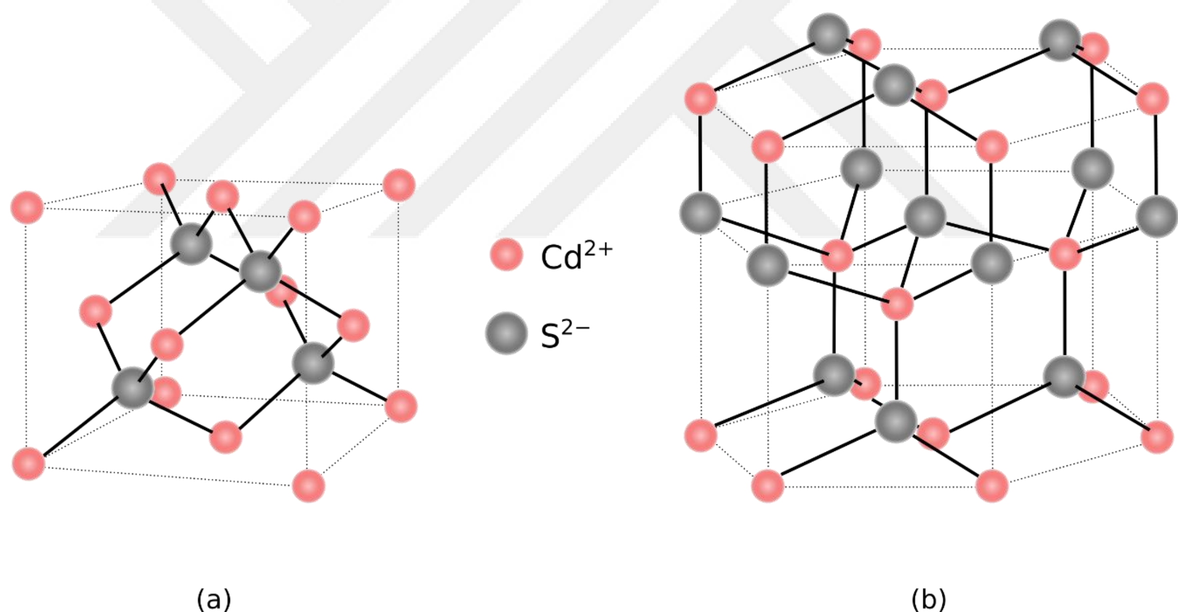

Figure 1.12. Two crystal lattice structures of CdS. **a)** Cubic zinc blende structure. **b)** Hexagonal wurtzite structure.

There are two other structures which CdS can crystallize; cubic rock salt and distorted rock salt. These two are pressure dependent and CdS can be transformed to these structures only under high-pressure conditions (Ziabari and Ghodsi, 2012).

CdS has a direct band gap for both (zinc blende and wurtzite) cases. The use of direct band gap materials such as CdS is the correct choice for semicondor-based optoelectronic devices since direct transition leads to the high optical absorption

(Mageswari et al., 2012a). In this way, it is avoided from unnecessary losses and can be produced efficient devices. In the indirect transition, after the excitation of an electron, electron can move from the valence band to the conduction band with the creation of a phonon. That causes to the lower optical absorption.

CdS is a wide band gap compound semiconductor. At room temperature, the band gap of the bulk CdS is 2.42 eV (absorption edge at 512 nm). The exciton Bohr radius of the bulk CdS is 2.5 nm (Sekhar et al., 2015). Furthermore, pure CdS is non-stoichiometric semiconductor (Wu et al., 2010) and exhibits an n-type conductivity owing to native defects or sulfur vacancies (V_S) and cadmium interstitials (I_{Cd}) (Narasimman et al., 2016).

1.5 Objective of Research

CdS has attracted considerable attention thanks to their tunable electronic and optical properties. As a window layer, n-type CdS is frequently used together with CdTe to form heterojunction solar cells (Rmili et al., 2013). Since it has attracted much interest owing to its unique properties, the reported studies which contain CdS thin films in the optoelectronic applications such as solar cells and light emitting diodes (LEDs) are particularly abundant in the literature.

However, after the literature survey, it was seen that there was no study on Ga-doped and (Ga-K)-co-doped CdS thin films by using the spray pyrolysis method. Therefore, it is aimed in this study to make some improvements on physical properties of CdS thin films by doping single and dual elements. Initially, it is examined the effects of 2 at.%, 4 at.%, 6 at.% and 8 at.% Ga concentrations on some physical properties of CdS thin films in order to find out Ga-doped CdS sample which possesses an optimum optical and electrical properties. Upon determination of optimum value of Ga content in CdS thin films, K contents of 1 at.%, 2 at.%, 3 at.%, 4 at.% and 5 at.% are selected to form (Ga-K)-co-doped CdS thin films having the best optical and electrical characteristics. To achive this purpose, it is planned to see enhancement in the optical and electrical properties of (Ga-K)-co-doped CdS samples. Our ultimate purpose is to reveal the suitability of the produced CdS:Ga and CdS:(Ga, K) thin films as a window layer in the inorganic-based solar cells.

CHAPTER 2 LITERATURE REVIEW

Among II-VI compounds, CdS is an attractive material for doping and this process is carried out with a variety of methods, including sputtering (Paudel et al., 2012), chemical bath deposition (CBD) (Lee et al., 2003), laser ablation (Dushkina et al., 2000), spray pyrolysis (Sivaraman et al., 2014), etc. The importance of addition of foreign atoms into the host material stems from the fact that the characteristic of undoped material can be changed through this way. The properties of CdS samples like optical, electrical, etc., can be controlled by doping with one or more elements and hence, they can become more suitable for optoelectronic applications.

Single element doped CdS studies including metallic or non-metallic elements are frequently encountered in literature. Several studies regarding with the positive contribution of anionic impurities to the electrical conductivity and transparency of CdS thin films have been reported by the researchers. Such studies have been done for donor type of dopants such as fluorine (F), chlorine (Cl), bromine (Br) and iodine (I).

Flores et al. (2013) synthesized F-doped CdS thin films through CBD and investigated the properties of them in terms of structural, topographical, optical and electrical properties. The structural analysis showed that the CdS thin films were in the hexagonal wurtzite structure. The F-doping increased the sulfur (S) deficiencies and it led to a decrease in the resistivity of CdS thin films because free carriers increased. A similar fall in the resistivity after F-doping has been reported. Yılmaz (2015a) grew F-doped CdS through the spray pyrolysis route. XRD investigation proved the strong preferred peak along (101) plane. SEM micrographs showed an increase in the grain size after 2 at.%, 4 at.% and 6 at.% F levels. The best carrier concentration and lowest resistivity being as 7.62 x 10^{12} cm^{-3} and 8.54 x 10^4 Ω.cm found respectively and a better transmittance value than those of others (over the 30%) is determined for 2 at.% F-doping. Also, band gap increment was observed besides an increase in the grain size. Altosaar and co-workers (2005) produced chemically bath deposited CdS thin films with dopants of Cl and I. Through the SEM, both thin film thickness and average grain size were calculated. They found that Cl-doped CdS samples had considerably low resistivity (almost two orders lower) in comparison to undoped CdS. However, CdS thin films deposited from CdI_2 bath were thinner and showed the highest resistivity. Cl atoms doped CdS thin films were fabricated by Sivaraman et al. (2015) by spray pyrolysis method by changing the doping level from 2 at.% to 8 at.% step by step to search for the effect of Cl-doping on the physical properties of CdS thin films. A regular decrease was observed in the particle size to 18.12 nm for 8 at.% Cl. They detected a variation in surface morphology from a porous structure (for

undoped CdS) to flower and needle-shaped nanostructures (after different Cl-dopings). From elemental analysis, it was deduced that the incorporation of Cl caused S deficiencies. Over the 80 % transmittance was exhibited for 8 at.% Cl-doped CdS thin films. A gradual band gap widening with Cl concentration were observed. Also, they found an electrical resistivity as low as 0.094 x 10^4 Ω.cm. Wu et al. (2010) synthesized Cl-doped n-type CdS nanowires by the thermal co-evaporation method. A growth direction along the [$2\bar{1}\bar{1}1$] with wurtzite structure was observed for Cl-doped CdS NWs. They found that Cl-doping dramatically affected the photoconductivity of CdS NWs in a good way. The crystal structures and morphologies were found as similar to all the produced CdS NWs. The examination of Br (2 at.%, 4 at.%, 6 at.% and 8 at.%) influences on some properties of CdS thin films was carried out by Narasimman and co-workers (2017). The coating of the thin films was made by spray technique. For the characterization of the CdS:Br thin films, XRD, SEM, UV-vis-NIR spectrophotometer and two-point probe setup were used. There was a strong preferential orientation along the (002). They computed the preferential orientation factor $f(002)$ for all samples and calculated values demonstrated that 6 at.% Br-doped CdS sample had the highest $f(002)$, indicating the improved crystallinity. Another indication of the enhanced crystalline quality was the increased crystallite size when Br-doping content approaching 6 at.%. A continuous decrement in the electrical resistivity was observed by introducing of Br into CdS. The optical transparency of 6 at.% Br-doped CdS sample was the highest, almost 89%. They found that the results were decent for optoelectronic applications.

The population of the studies on alkali metals doped CdS thin films were scarce. Mayorova et al. (2014) focused on the effect of lithium (Li), sodium (Na), potassium (K) and rubidium (Rb) alkali metal impurities on the properties of photoconductivity of CdS films at the substrate temperature of 450 °C. They found that unlike CdS:Li one, steady-state photocurrent increased for all CdS:Na, CdS:K and CdS:Rb thin films when compared to undoped CdS. Klyuev and Maiorova (2007) investigated the luminescence properties and achieved 3-5 times better luminescence intensity than that of undoped CdS films for CdS:Li, CdS:Na, CdS:K and CdS:Cs thin films. Moreover, they observed that, as the dopant impurities increased, the luminescence intensities increased for CdS:K and CdS:Cs films, these films weren't affected by the deposition temperature. Bidadi et al. (1996) analyzed the influence of Li and Na on the CdS in terms of electrical and luminescence aspects. The photoconductivity for CdS:Li and CdS:Na samples were observed at a broad spectrum which was between 525 and 700 nm, maximum at 550 nm. Sandoval et al. (2013) grew CdS:Li nanoparticles through thermolysis method. They characterized Li-doped CdS nanoparticles in terms of optical and structural view. The Li content was selected as 3 at.%,

5 at.%, 7 at.% and 10 at.%. The variation in the energy band gap from 2.7 to 3.6 eV was observed. A peak value at almost 465 nm for all the CdS:Li samples was noticed from the photoluminescence (PL) spectra. The highest emission intensity was found for CdS sample which had 3 at.% Li content. Kumar and co-workers (2017) prepared Na-doped CdS thin film through photochemical deposition. From XRD study, CdS:Na thin film was seen to be in the cubic phase. A spherical surface morphology was obtained at first, then turned into rod-like with Na incorporation. A wider optical absorption for CdS:Na thin film was attained. The carrier concentration of pure CdS film increased from 10^{13} cm^{-3} to 1.28 x 10^{15} cm^{-3} after Na-doping. Also, they found a decrement in the electrical resistivity, from 10^5 Ω cm for undoped CdS to 1.22 x 10^2 Ω.cm for CdS:Na.

Various studies searching for the influences of other element dopings, such as alkaline earth metals, transition metals, etc., on the electrical and optical properties of CdS thin films were conducted by the researchers. For instance, Sivaraman et al. (2014) doped CdS with magnesium (Mg) by selecting Mg-contents as 2 at.%, 4 at.%, 6 at.% and 8 at.%. The deposition method was spray pyrolysis. The properties of the prepared thin films of CdS:Mg were investigated. Due to the higher texture coefficient, the comment that 6 at.% Mg-doped CdS sample had better crystalline quality was made. They detected that the microstructure had a strong dependence on the Mg-doping level, it varied from a highly porous surface (0 at.%) to the needle-shaped nanorods (6 at.%) and this conclusion was in accordance with XRD data. Furthermore, they found the minimum resistivity value, 1.87 x 10^2 Ω.cm, for the same concentration level. Shah et al. (2012) made a research seeking the influence of copper (Cu) on the physical properties of CdS thin films. Cu deposition was employed by the close-spaced sublimation (CSS) route. The grain size increased with increasing Cu content and it was confirmed with XRD and SEM measurements. A considerable reduction in the electrical resistivity was attained after Cu level increased and this resistivity drop was at several orders of magnitude when compared to the resistivity of as-deposited CdS. They found the highest mobility value as 1.15 x 10^3 cm^2/V.s. The variation in optoelectrical properties of CdS after the introduction of silver (Ag) doping was investigated by Nazir et al. (2014) to unveil the suitability of CdS:Ag thin films for solar cell applications. The technique they used to grow CdS:Ag thin films was CSS. The Ag content was increased from 2 at.% to 5 at.% with steps of 1 at.%. XRD measurement confirmed the polycrystalline behavior of prepared films with the preferred orientation along (111) plane. The significant drop in resistivity from 3 x 10^6 Ω.cm to the 3.6 x 10^3 Ω.cm was obtained with increasing Ag level to 5 at.%. They found the band gap of 5 at.% Ag-doped CdS thin films as 2.30 eV. Anbarasi and co-workers (2014) conducted a study that investigated the effect of (zinc) Zn on CdS thin films in terms of structural, morphological, optical and electrical

properties. The dopings for spray deposited Zn were 2 at.%, 4 at.%, 6 at.% and 8 at.%. From XRD analysis, it was determined that all CdS and CdS:Zn thin films had a hexagonal phase with the preferred orientation along the (002) plane and preferential orientation wasn't affected from Zn concentration. Optical studies showed that high transmittance values were observed for undoped and Zn-doped CdS samples in the visible region. CdS:Zn (2 at.%) sample displayed the highest transmittance, almost over 85%, around 600 nm. However, 8 at.% Zn-doped CdS exhibited not only good optical transmittance but also a large band gap (2.6 eV) and the lowest resistivity value (0.574 x 10^{-3} Ω.cm). They deduced that CdS:Zn thin films could be a good selection for the heterojunction solar cells (as a window layer) and optoelectronic devices. CdS thin films at various levels of lead (Pb) concentrations (2 at.%, 4 at.%, 6 at.% and 8 at.%) were constructed with spray pyrolysis method using the perfume atomizer and these films were characterized by Anbarasi et al. (2016). They achieved an electrical resistivity as low as 0.068 x 10^{1} Ω.cm with 6 at.% Pb-doped sample. In addition to obtaining an optimum band gap value of 2.42 eV, also the best transmittance value among all thin films was attained almost as 85% for this doping level.

There are also some studies of group IIIA elements doped CdS thin films. As is known, pure CdS has a high resistivity about 10^{7}-10^{8} Ω.cm (Anbarasi et al., 2016). Therefore, it is necessary to diminish the resistivity to be practicable for the solar cells and it was reported that the resistivity decreased after the incorporation of group III elements into CdS. For instance, Lee et al. (2003) fabricated B-doped CdS thin films via the CBD. The change of structural, electrical and optical properties of CdS thin films were investigated upon B-doping. They achieved a dramatic decrease in resistivity of CdS thin films when B level was increased. The minimum resistivity value was 2 Ω.cm. CdS with Al content of 2 at.%, 4 at.%, 6 at.% and 8 at.% was studied by Muthusamy et al. (2014). It was realized from XRD pattern that CdS:Al thin films had the mixed phases of cubic and hexagonal while undoped CdS had a cubic phase. Two distinct bands were seen from PL spectra of CdS and CdS:Al thin films. One was at 409 nm while the other located at 547 nm. Furthermore, they found that 6 at.% Al-doped CdS thin films showed the highest PL intensity among the other doped thin films.

However, studies on Ga-doped CdS are scarce. For instance, Wu and co-workers (2011) constructed Ga-doped CdS nanoribbons via a convenient route on silica substrates to fabricate a heterojunction structure for nano-optoelectronic applications. They found that all CdS:Ga NR/Si heterojunctions showed an excellent device performance by virtue of high stability, high efficiency and fast response speed. CdS:Ga thin films were synthesized through CBD by Khallaf et al. (2009b). All prepared films were characterized in various ways. For all CdS:Ga thin films, a red shift was observed in the absorption edge. They

achieved a level of low resistivity of 1.2 x 10^{-2} Ω.cm and a level of high carrier concentration 2.96 x 10^{19} cm^{-3} at their Ga-doped CdS work. Bala and co-workers (2015) synthesized Ga-doped CdS nanocomposites by in situ-chemical route at room temperature. In their research, they focused on the optical properties of the produced CdS nanocomposites and compared the experimental results with theoretical results. Cai et al. (2011) reported such a behaviour after increasing of Ga concentration. They synthesized Ga-doped n-type CdS nanowires (NWs) by means of thermal evaporation method and investigated the suitability of CdS:Ga NWs for nano-optoelectronic applications. They achieved a considerable enhancement in device performance.

Atay and co-workers (2003) produced undoped and In-doped CdS thin films with ultrasonic spray pyrolysis. In levels at their work were chosen as 25 at.%, 35 at.% and 45 at.%. The best conductivity was seen for the sample of CdS:In (45 at.%). There was almost no change in the band gap values after In-dopings. By using two-probe technique, the results were found as 4.72 x 10^{8} Ω cm and 1.06 x 10^{3} Ω cm for CdS and CdS:In (45 at.%), respectively.

The simultaneous doping of CdS material with two elements can also be a good approach to improve some physical properties of CdS thin films. In the literature, it was seen such studies that elements of Al, Cu, Na, Cl, Mg, Zn, F, iron (Fe), Ga and K were used as dual dopants in CdS. CdS thin films as dual-doped with Cl and Al were constructed by Akintunde (2000) and it was investigated the influences of Al and Cl on the electrical and optical properties of CdS thin films. The weight percentage of Cl was fixed at 0.0007. However, the concentration was changed from 0.0002 to the 0.01 wt.% for Al. When Al concentration was increased to 0.001 wt.%, the dark electrical conductivity of Al-doped CdS:Cl thin films increased up to 3.10 x 10^{-4} $(Ω.cm)^{-1}$. Moreover, the band gap and transmittance values were found as good enough for the potential applications like solar cells. In addition to pure CdS thin films, CdS:Cu and CdS:(Cu, Al) thin films grown with CBD by Hemathangam et al. (2016). Cu level was 4 at.% in CdS for single doping and Cu and Al contents were 4 at.% and 2 at.% in CdS, respectively for dual doping. They found that the cubic structure of pure CdS and $Cd_{1-x}Cu_xS$ (x=0.04) turned into a mix of cubic and hexagonal structure for $Cd_{1-x-y}Cu_xAl_yS$ (x=0.04, y=0.02). Average crystallite size was found for (Cu, Al)-co-doped CdS sample as 2.66 nm. In the visible region, the high transmittance was exhibited by all thin films. The band gap of CdS: (Cu, Al) sample was 2.49 eV. Yılmaz et al. (2015b) prepared thin films of CdS, CdS:Al, CdS:Na and CdS:(Al, Na) with spray pyrolysis. Al and Na contents were applied as 4 at.% for single and co-doped studies. The hexagonal wurtzite structure for all the prepared thin films was found with the (101) preferred orientation. A band gap value of 2.08 eV was calculated after (Al, Na)-co-doping. The carrier

concentration and resistivity for $Cd_{0.92}Al_{0.04}Na_{0.04}S$ were obtained as 2.38 x 10^{12} cm^{-3} and 1.62 x 10^{5} Ω cm, respectively. Sivaraman and co-workers (2016a) analyzed the effect of dual doping of Mg and Cl on structural, morphological, optical and electrical properties of CdS thin films. Both Mg and Cl concentration levels were selected as the values of 2 at.%, 4 at.%, 6 at.% and 8 at.%. They observed small decrement on the lattice parameters with increasing dopant contents of Mg and Cl. The morphological investigation demonstrated the existence of an alteration from needle-shaped grains, for CdS, to nanosized grains as the (Mg, Cl) dual doping contents increased. Absorption spectra showed that (2 at.% Mg, 2 at.% Cl)-co-doped CdS sample had higher absorbance than that of the other (Mg, Cl)-co-doped CdS thin films. Also, a blue shift was observed in optical band gaps for all co-doped CdS thin films in comparison to pure CdS thin film. The minimum resistivity was 1.332 x 10^{1} Ω.cm for (6 at.% Mg, 6 at.% Cl)-co-doped CdS sample. CdS: (Cl, Zn) thin films were fabricated by Selvan et al. (2016) via spray pyrolysis. Zn concentration was fixed constant as 2 at.% for all thin films. The level of Cl, however, was changed from 0 at.% to 8 at.%. The (002) preferred orientation was observed. Cl-doping made a positive contribution by means of decreasing the resistivity values of CdS:Zn thin films. For instance, the lowest resistivity was found to be 0.614 x 10^{-3} Ω.cm for 6 at.% Cl-doped CdS:Zn sample. Also transparency enhanced, especially for 8 at.% Cl-doped one. The blue shift in the optical band gap was observed as Cl content was increased in CdS:Zn. The band gap value of 6 at.% Cl-doped CdS:Zn was 2.84 eV. The suitability of co-doped films for the optoelectronic applications was revealed due to their high transparency, wide band gap and low electrical resistivity. Dual doped CdS (Mg, F) thin films were prepared by Sivaraman et al. (2016b). The substrate temperature for thin film preparation was at 400 °C and thin films were spray deposited. The Mg and F contents were chosen as 2 at.%, 4 at.%, 6 at.% and 8 at.%. They surveyed the effect of these on physical properties of the prepared CdS thin films. Crystallite size decreased continually with the increase of dual content of Mg and F. SEM showed that a variation from irregular-shaped grains to the needle-shaped grains with increasing contents of Mg and F. The electrical resistivity of the samples decreased in general after dual doping. The non-stoichiometric nature was seen for thin films of CdS: (Mg, F) from EDS spectra. They were achieved to enhance the optical and electrical properties of spray deposited CdS thin films by simultaneous doping of Mg and F elements. Therefore, CdS: (Mg, F) thin films can be used as a window layer in HJSCs. Liu and co-workers (2007) synthesized dual doped (Zn, Fe) CdS thin films by low-pressure metal-organic chemical vapor deposition (CVD) method and investigated influences of Zn element on optical and electrical properties of Fe-doped CdS films. XRD revealed the strong preferred orientation along (0002) for all films. Pitchaimani et al. (2016) fixed Fe content as 2 at.% but changing the Zn level as 2 at.%, 4 at.% and 6 at.%, they searched for the effect of dual doping on

CdS thin films in terms of structural and optical aspects. They found that $Cd_{0.94}Zn_{0.04}Fe_{0.02}S$ thin films had higher transmittance than those of the others besides the formation of wider band gap that made them more suitable for optoelectronic devices. Wang and co-workers (2014) fabricated n-type $Zn_xCd_{1-x}S$:Ga nanoribbons (NRs) by thermal co-evaporation technique. The growth directions of NRs were along [0002]. Crystallinity and phase of thin films were revealed by XRD measurement. They detected that Ga-doping improved the electrical conductivity of the produced NRs considerably. Chemical bath deposited Na and K co-doped CdS thin films were investigated by Mageswari et al. (2012b). XRD confirmed that all films had a cubic zinc blende structure. The surface of the undoped CdS films seemed a continuous, dense and homogeneous morphology after they were simultaneously doped with Na and K. AFM measurement showed that CdS: (Na, K) films had a crack free morphology. It was revealed from the optical measurements that the absorption edge of all thin films shifted towards the shorter wavelength and the increases in the optical transmission and the band gap values were observed for Na-doped CdS, K-doped CdS and Na-K co-doped CdS films in comparison to undoped CdS.

CHAPTER 3 MATERIALS AND METHODS

3.1 Spray Pyrolysis Deposition Technique

3.1.1 Introduction

Thin film deposition techniques are mainly comprised of two ways. These are physical and chemical. Some examples of the physical techniques are molecular beam epitaxy, sputtering and laser ablation. The chemical process, in other respects, comprised of two main branches as liquid and gas phase and some examples to them are CVD, atmospheric pressure CVD, spin coating and spray pyrolysis. Of all these techniques, there is a prominent one which gets the advantage over the others. It is spray pyrolysis and known as a chemical technique since thin films are formed on a substrate as a result of the chemical reaction. There is a growing interest in obtaining thin films by this method. Due to inexpensiveness of the method and making easier the manufacturing of thin film, it has been used for years to produce a thin film buffer layer in a variety of applications; solar cells, transistors, LEDs and so forth. Furthermore, it allows thin film to be deposited on large surface areas. Another advantage is that the components used in the method don't require a vacuum environment. This makes the operation quite simple.

The spray pyrolysis basically is used to make thin film coating through an aqueous solution. The aqueous solution is prepared from specific concentrations of salts containing elements of the material desired to be obtained. Then, this liquid solution is sprayed onto a preheated substrate as fine droplets at a certain flow rate for a certain period of time. Nitrogen gas or air is used as carrier gas in this process. The films obtained by this technique are overwhelmingly in the polycrystalline structure and highly homogeneous (Bedir et al., 2014). In addition to these, high-quality film coatings can be constructed. In this method, materials can be deposited on various kinds of substrates such as plastic, glass, quartz, ceramic, mica, indium tin oxide and fluorine doped tin oxide.

3.1.2 Influence of spray parameters

The properties of the produced materials can be controlled and changed with proper adjustment of the spraying conditions. Thin film quality and properties considerably depend on the spray parameters. These parameters are substrate temperature, solution flow rate, type of salts, solvent types, deposition time, precursor solution, nozzle to substrate distance, deposition rate, angle of the spray head, etc. By manipulating these parameters, the thickness of the semiconductor materials, forbidden energy gap, electrical and optical properties can be changed. Two of them were explained as follows.

3.1.2.1 Substrate temperature

Substrate temperature is accepted as the most important parameter affecting thin film properties by many researchers. It influences the thin film morphology significantly, such as film roughness, crystallinity, etc. As the substrate temperature increases, thin film morphology can change from a cracked to a porous microstructure (Perednis and Gauckler, 2004).

3.1.2.2 Nozzle to substrate distance

The distance between the spray head and substrate is very important for thin film production. If this distance is too high, droplets evaporate before reaching the substrate surface and thin film formation process is affected negatively. If this distance is too close, accumulation may occur on the substrate before appropriate conditions for chemical spraying develop. Furthermore, the adherence of thin films onto the substrate can take place weakly. This parameter also plays an important role in determining film thickness.

3.1.3 Setup components

The components of spray pyrolysis method are substrate heater, temperature controller, precursor solution and nozzle. A schematic diagram of spray pyrolysis is shown in Figure 3.1.

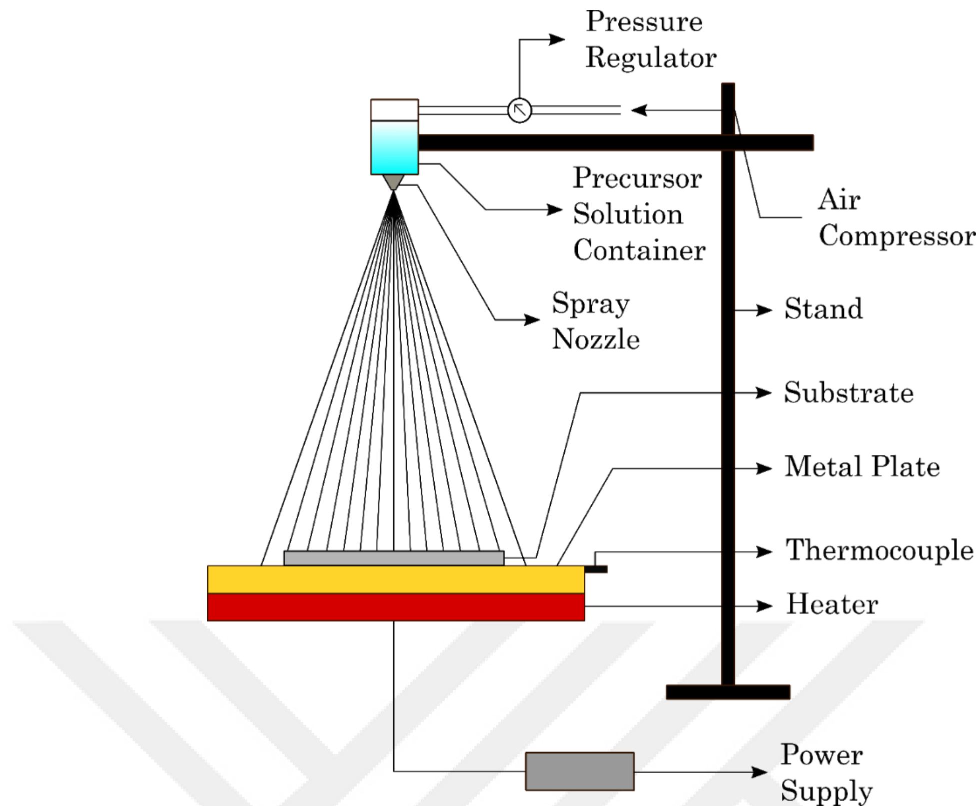

Figure 3.1. Schematic diagram of the homemade spray pyrolysis system.

3.1.3.1 Nozzle

The spraying of the salt solution onto the substrate surface with droplets of different sizes is accomplished with the help of nozzle. The nozzle is quite important in thin films because the geometry of the spray head greatly affects the spray droplet size and spray rate (Perednis, 2003).

3.1.3.2 Substrate heater

The substrate heater is utilized to heat the substrates till the desired temperature before the deposition process is initiated.

3.1.3.3 Temperature controller

The temperature of the substrate is controlled by a K type thermocouple and its main function is to keep the substrate temperature at a desired value.

3.2 Preparation of Thin Films

3.2.1 Substrate cleaning process

The substrate cleaning process is a quite important factor which determines the produced film quality. In this work, glass slides were chosen for Ga-doped CdS and (Ga-K)-co-doped CdS thin film growth because they have low-cost advantage in comparison to other types of substrates. The glass substrates (1 cm x 1.5 cm) were cleaned by ultrasonic washing in acetone and ethanol solutions and in distilled water, respectively. The ultrasonic cleaning process of the substrates in solvents lasted 10 minutes individually and they were dried with air flow.

3.2.2 Synthesis of CdS:Ga thin films

To attain undoped CdS thin films and 2 at.%, 4 at.%, 6 at.% and 8 at.% Ga-doped CdS thin films, 0.05 M cadmium chloride ($CdCl_2$), 0.1 M thiourea ($(NH_2)_2CS$) and 0.05 M gallium nitrate ($Ga(NO_3)_3$) salt were dissolved in distilled water all together (100 ml). The mixture was stirred vigorously by means of a magnetic stirrer until the used salts are dissolved completely. The substrate temperature was kept at 400 °C and temperature were controlled by a thermocouple type K, which was composed of a couple of chromel and alumel wires. The deposition time was applied for 20 minutes. The distance between nozzle and substrate was adjusted as 20 cm and the spraying rate was maintained at 2 ml per minute using compressed air. The substrate plate was rotated at the speed of 10 revolutions per minute. After the deposition, CdS and Ga-doped CdS thin films were obtained and it was seen that a uniform coverage and a good adherence to the glass substrate's surface were accomplished for these CdS and Ga-doped CdS thin films.

3.2.3 Synthesis of (Ga-K)-co-doped CdS thin films

After the determination of optimum Ga concentration (2 at.%) by means of investigation of optical and electrical properties of the fabricated Ga-doped CdS thin films, this concentration was kept constant for the synthesis of K-doped CdS:Ga thin films. The same cleaning procedures for glass substrates were conducted. To prepare CdS:(Ga, K) solutions (100 ml), 0.05 M cadmium chloride, 0.1 M thiourea, 0.05 M gallium nitrate and 0.05 M potassium chloride (KCl) salts were used. K level was selected as 1 at.%, 2 at.%, 3 at.%, 4 at.% and 5 at.%. After the deposition, (Ga-K)-co-doped CdS thin films were rinsed with distilled water in order to remove deposited particles on the surface to which attached loosely and then, were dried in air ambience. Spray nozzle to substrate distance, substrate

temperature, the spray rate and the rotation speed of the substrate plate were adjusted as the same as those of Ga-doped CdS thin films. Consequently, CdS:(Ga, K) thin films were achieved in the desired uniformity.

3.3 Characterization Techniques

Characterization refers to the usage of various techniques in order to probe the structure and properties of a material. The characterization methods which are used in this work are demonstrated in detail.

3.3.1 X-ray diffraction (XRD)

X-rays were discovered by Wilhelm Conrad Roentgen in 1895. X-rays are highly energetic electromagnetic radiation with a smaller wavelength than visible light and the wavelength varies between 0.01 Å and 10 Å. X-ray diffraction (XRD) is the most commonly used diffraction technique for studying crystal structure of solids such as metals, ceramics and minerals due to some reasons. The first one is that the wavelength of X-rays is comparable with interatomic distance. This feature allows it to be used in structural studies. Furthermore, X-ray scattering techniques are non-destructive. In other words, they don't modify the structure of sample being examined. Another advantage of XRD method is that the analysis of the samples can be made in a short time.

X-rays are produced by means of a vacuum-sealed device called X-ray tube. The tube has a cathode (negative electrode) at one end and a metal anode (positive electrode) at the other end. An element which has a high melting point is used for filament since it can endure the higher heat. When the current passes through the filament, it heats due to the high resistance of filament and it starts to give off electrons. These electrons are accelerated between the cathode and the anode by an extremely high potential difference and impinge on a metal slab made of heavy atoms like copper, but usually, the metal target may be chosen from tungsten material due to its considerably high melting point among all the metals, 3422 °C (Francis et al., 2016). Thus, this element can easily withstand the high temperatures caused by electron bombardment. The accelerated electrons lose almost all their kinetic energy during this collision. An electron from lower orbitals of tungsten atom is kicked out when the accelerated electron collides with the tungsten atom. From a higher energy level, an electron falls to lower energy level in order to make fill to the missing electron state. Hence, an extra energy is released in the form of a photon and called X-ray photon. During the process, heat can increase. Therefore a cooling process must be

conducted to defeat the heat increment. Also, the tube is covered by a lead material so as to prevent escaping X-rays in all directions. A narrow part that allows the escaping of X-ray photons is open in an X-ray tube. The schematic of an X-ray tube is given in Figure 3.2.

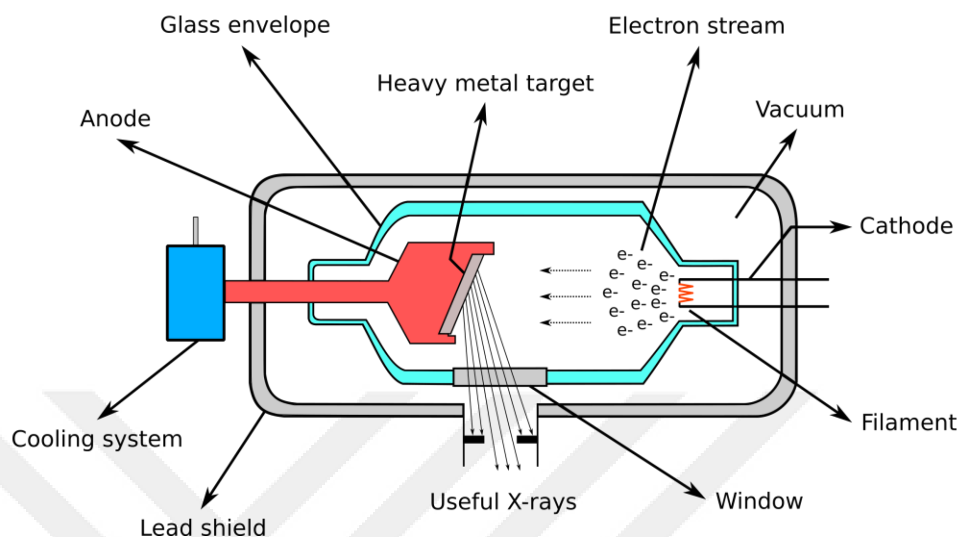

Figure 3.2. Schematic diagram of an X-ray tube.

When incoming X-ray photons are striked to atoms within planes of crystal, they are scattered by the sample. If there is a phase shift between the reflected beams, they may destroy each other and may not be able to measure a clear beam reflectance. But if the reflected beams are in the same phase, they strengthen each other and an intensive reflection occurs. This strong reflection is in the form of peaks observed at certain angles in the measuring device and called as constructive interference. In other words, the Bragg's rule satisfies that the reflected beams are in the same phase. Bragg's rule is formulated by

$$n\lambda = 2d\,sin\,\theta \tag{3.1}$$

Many information about the crystal can be determined from the XRD analysis. These are as follows: unit cell size, crystallite size, percentage of crystallinity, phase identification, determination of grain orientation and calculation of lattice parameter.

A Rigaku D/Max-IIIC diffractometer, which was given in Figure 3.3, was used in this work to get XRD patterns of the samples with a CuKα radiation ($\lambda = 1.5406$ Å) in the range

of 20-60° at room temperature with the step of 0.01° and the X-ray generator was set at 30.0 mA and 40.0 kV.

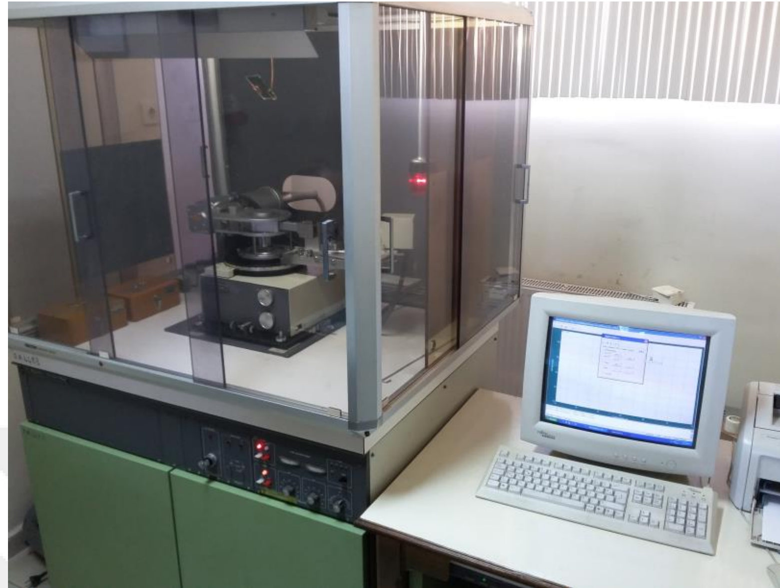

Figure 3.3. Rigaku D/Max-IIIC diffractometer.

The *a* and *c* lattice parameters of the samples were calculated from the following formulas for both zinc blende cubic (Equation 3.2) and hexagonal wurtzite (Equation 3.3) structures of CdS for different doping concentrations.

$$\frac{1}{d^2_{(hkl)}} = \frac{h^2 + k^2 + l^2}{a^2} \tag{3.2}$$

where d_{hkl} is the interplane distance

$$\frac{1}{d^2_{(hkl)}} = \frac{4}{3}\left(\frac{h^2 + hk + k^2}{a^2}\right) + \frac{l^2}{c^2} \tag{3.3}$$

Scherrer formula is used to determine the crystallite size (D) in nm

$$D = \frac{K\lambda}{\beta \cos\theta} \quad (3.4)$$

where K is a constant called Scherrer constant and relies on such as the crystal shape, etc., it equals to 0.94 in this case, λ is the wavelength of the X-ray, β is the full width at half maximum (FWHM) in radians and θ is the angle of diffraction (Bragg angle).

3.3.2 Scanning electron microscopy (SEM)

In scanning electron microscopy (SEM), electrons are used instead of photons in contrast to optic microscopes. A resolution better than 1 nm can be attained by SEM device (Stokes, 2008). The working principle of the device can be explained basically with some steps. First, electrons are produced from a suitable electron source that acts as a cathode. These produced electrons are accelerated between the cathode and an anode by applying a high voltage across them (0.5-30 kV), most typically 20 kV. Then, they are condensed by condenser lenses and the objective lens. These accelerated electrons eventually turn into a fine electron beam. A raster scanning is then performed over the sample surface using a high energy beam of electrons. The electrons striking on the sample scatter both elastically and inelastically from the sample's surface. As a consequence of the interaction of incoming electrons with the specimen, various signals including both as electrons and photons emerge. These signals are collected through relevant detectors. There is one detector at least for collecting the signals that is the secondary electron detector. However, SEM can be equipped with many other detectors such as backscattered electron detectors, energy dispersive spectrometer and, etc. After collection of signals, they are amplified with a photomultiplier tube. Then, the image of a sample is constructed on a device of screen.

The samples in SEM must be conductive so that the information can be obtained. Thus, the insulator samples should be coated with a conductive material if it desires to be analyzed. Otherwise, electrons will accumulate on the surface of the sample. This is called as "charging" and in this situation, insufficient information can be only given to the detectors.

There are various imaging modes in SEM. Secondary-electron (SEI) imaging and backscattered-electron (BSE) imaging are main SEM techniques. The others are electron backscattered diffraction, energy-dispersive X-ray spectroscopy (EDS), high-resolution SEM, etc.

A great advantage of SEM is its high depth of field (Stokes, 2008). High resolution, high magnification, easy sample preparation, etc. are other advantages of the SEM.

However, it needs high vacuum environment, a conductive sample and a large space and its maintenance cost is high. By using this device geologic and biologic samples and many types of materials can be examined.

SEM devices need a suitable environment for examining the samples properly. It must be a vibration free room which doesn't involve any external magnetic and electric fields. SEM provides information mainly about morphological and compositional properties.

A JEOL JSM-6610 SEM equipped with an EDS (Oxford Instruments), which was given in Figure 3.4, was used to perform morphological and elemental analyses in this study.

Figure 3.4. JEOL JSM-6610 SEM device equipped with the Oxford Instruments EDS. https://www.jeol.co.jp/en/products/detail/JSM-6610series.html.

3.3.2.1 Components of SEM

SEM devices consist of several parts. The most important ones are electron gun, apertures, electromagnetic lenses, scan coils, objective lens, various detectors, sample stage, vacuum pumps and cooling system. The components of a typical SEM device is illustrated in Figure 3.5 and their roles in the device are mentioned below.

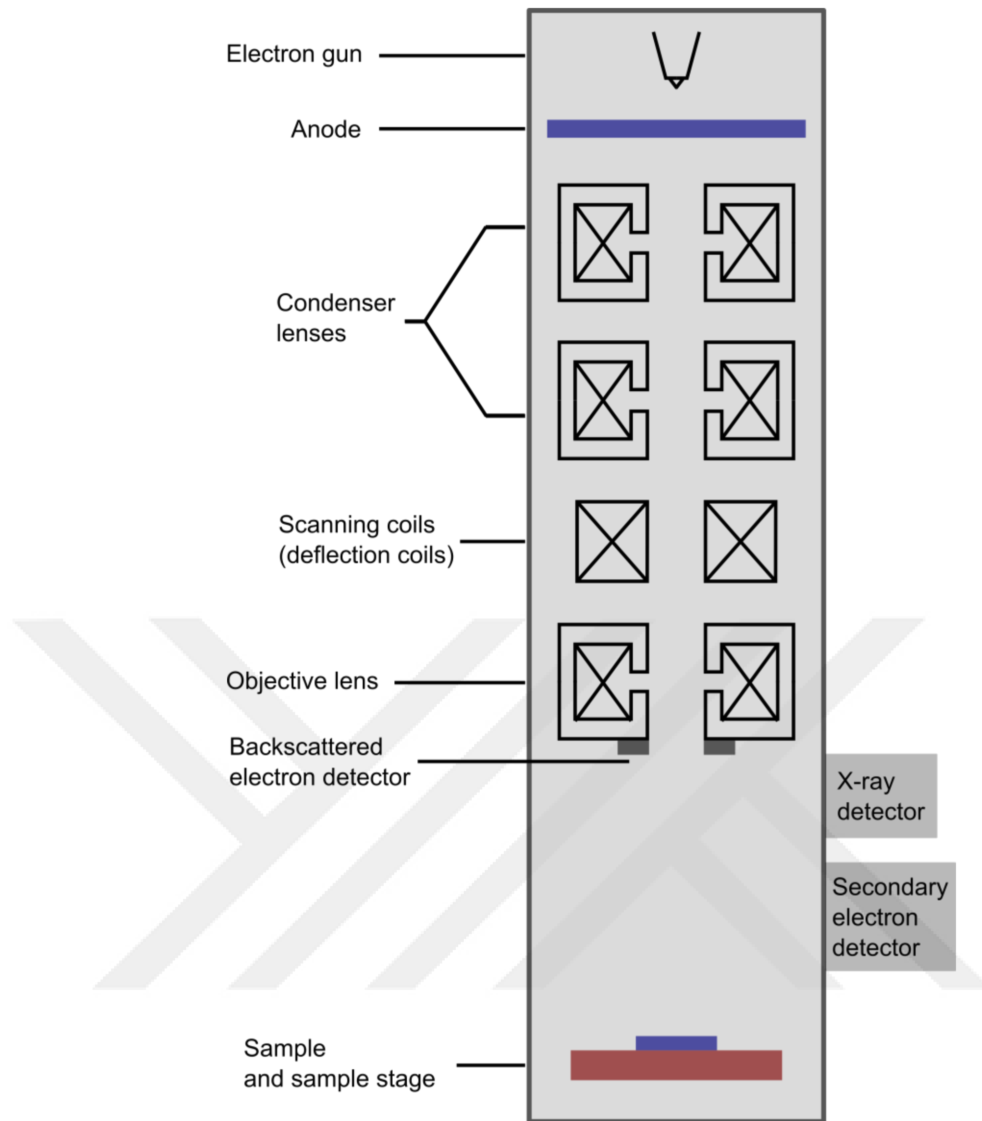

Figure 3.5. Schematic diagram of an SEM device.

Electron gun: Electron gun locates at top of the column and it is used to produce a stable electron beam. This electron beam is called also as the primary electron beam. There are mainly two types of electron guns that exist to extract the electrons from their associated atoms. The first one is thermionic guns and the other one is field emission guns (FEG). In thermionic guns, a Tungsten (W) wire or a single crystal of lanthanum hexaboride (LaB_6) are used as the most common source of electron emitters. These conductive materials are heated until electrons in the outermost orbital can overcome the energy barrier known as work function. For tungsten filament, this temperature is 2700 K. However, a single crystal of LaB_6 operates at a lower temperature than tungsten, it is heated till 1700 K by applying a voltage and it is durable enough to withstand high electric currents. Also, a LaB_6 crystal source provides nearly 10 times brightness than that of tungsten as well as a longer lifespan

(Goldstein et al., 2012). When sufficient kinetic energy is gained, electrons escape from the emitter. As the temperature increases, the number of electrons leaving the source increases. Thermionic emission guns are commonly preferred type of guns because of their features of simplicity and inexpensiveness. As for FEGs, they can be operated at room temperature (300 K), that is, no heating treatment is performed, instead, a strong electric field is applied to the metal surface and electrons are drawn from the emission source.

The vacuum requirements are different for different type of guns. Tungsten filament requires 10^{-5} torr vacuum while a single crystal of LaB_6 requires 10^{-7} torr vacuum (Stokes, 2008). However, a typical FEG requires ultra-high vacuum; 10^{-10} torr (Stokes, 2008). An important advantage of FEG is that it has the longest lifetime among the gun types.

Apertures: With the help of the apertures, the number of electrons that reach the specimen can be changed.

Electromagnetic lenses: Condenser lenses and objective lens are two types of electromagnetic lenses used in an SEM device. Demagnification process of the electron beam to a small spot is achieved by two condenser lenses and they locate between electron gun and scanning coils. These lenses are used to control the electron beam shape and size and hence, electron beam current (number of electrons). The condenser lens is used to focus the generated electron beam while passing through the column. Spot size controlling is fulfilled by a set of condenser lenses.

The objective lens is the last electromagnetic lens being controlled the electron beam and it lies under the scan coils. It is used to focus the incoming electron beam on the sample. The distance between objective lens and sample is called as working distance. When the working distance is reduced, a more finely beam is obtained from the focused beam. Therefore, the resolving power increases.

Scan coils: Scan coils are located above the objective lens. A raster scanning of the electron beam through the specimen are executed by scan coils. In order to be able to scan on the sample, the electron beam has to be moved to the left, right, up and down.

Specimen test chamber: The test chamber is a lower part of SEM. The specimen, sample stage and various detectors are located in this section. This space also has to keep

under high-vacuum condition to prevent scattering of the electron beam and to ease to collect electrons efficiently by means of detectors.

Sample stage: The sample stage situates in the specimen chamber. It is the place where the sample is inserted and examined. The movement of the stage in directions of x, y and z can be conducted by using the software interface.

Detectors to detect various signals: Several detectors can be positioned to test chamber to detect signals. Secondary electron detector and back-scattered electron detector are frequently used detectors in SEMs.

Display devices: All images of samples appear on a display unit.

Vacuum system: The vacuum system is very crucial on an SEM to conserve gun pressure and chamber pressure. If there is not a good vacuum, dirt will accumulate on the electron emitting surface (electron gun) and this leads to reduction the lifetime of the electron source. The pressure should be low enough for operation of the electron gun properly. Otherwise, the generated electron beams are hindered by the air particles and cannot travel long distances. So, literally, they don't reach the sample's surface. Chamber pressure is also important and has to be at high vacuum condition. So, it allows the access of the electron signals from specimen to the relevant detector. The electron gun section and the column are vacuumed together.

The four types of pumps are the most used as vacuum pumps in SEMs. These are rotary, turbomolecular, sputter ion and oil diffusion pumps. Due to an ultra-high vacuum requirement, oil diffusion pump is used primarily and is also supported by a rotary pump generally (Lyman et al., 1990).

3.3.2.2 Electron-material interaction

As a result of electron-material interaction, some signals arise; secondary electrons, backscattered electrons, Auger electrons, cathodoluminescence and X-rays. These signals are shown in Figure 3.6. Some electrons from incoming electron beam can pass through the specimen. These are transmitted electrons.

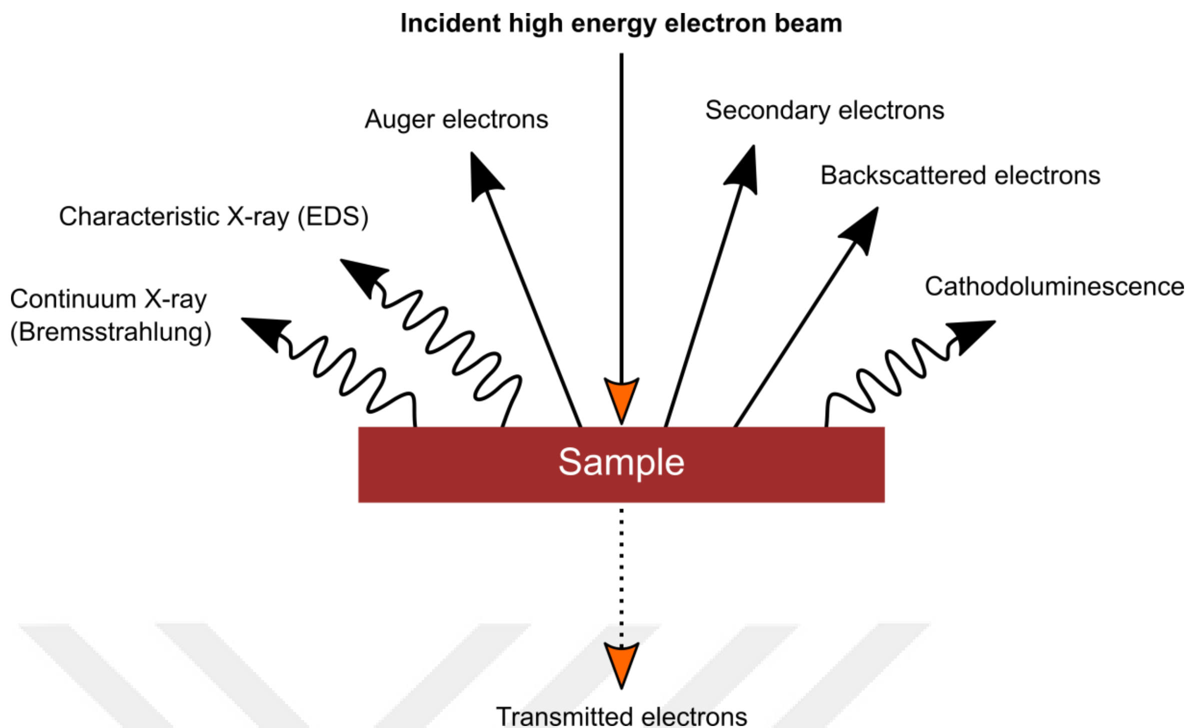

Figure 3.6. The signals arising after the interaction between the electron beam and sample.

Secondary electrons: Secondary electrons are low energy electrons (less than 50 eV) (Stokes, 2008). If the highly energetic primary electrons collide with weakly bonded valence electrons inelastically, the electrons in the valence band can be knocked out. These electrons from the orbit of their atoms are so-called secondary electrons. Since these electrons have relatively small energy, they cannot penetrate deeper in the sample and can be found near the sample's surface. Hence, they can be easily attracted by applying them a positive voltage due to their negative charges. Secondary electrons mainly give information about surface topography.

Backscattered electrons: The backscattered electrons are highly energetic electrons (more than the 50 eV, up to the energy level of the primary electron beam) (Stokes, 2008). Therefore, backscattered electrons give more information about deeper region of the sample due to deeper penetration of these electrons in the specimen. They result from elastic collision of primary electrons with atoms of the sample and change their path up to 180 degrees. These electrons which return to backward and leave the sample are so-called backscattered electrons. Backscattered electrons mainly give chemical information about sample such as the atomic number.

3.3.3 Energy dispersive X-ray spectroscopy (EDS)

EDS is a chemical microanalysis technique which is utilized frequently by integrating into an SEM or a TEM device. EDS is a non-destructive method and chemical composition information of all elements whose atomic number is greater than three can be provided by this technique. The detection of elemental abundances can be made by this technique. After the primary electrons interact with atoms of sample in an electron microscope, a variety of emissions emerges as discussed before. Of all, X-rays concern us in EDS analysis. The electron-material interaction results in two types of X-rays; continuous (Bremsstrahlung) X-rays and characteristic X-rays. First, when high-speed electron beam approaches to nucleus of the target atom, it is affected by the attraction force resulting from the positive charge of the nucleus (coulomb attraction) and highly energetic electrons decelerate. Therefore, electron beam loses energy and lost energy is emitted as photons. Second, after electrons sent on the target atom interact with the electrons in the orbital of the target atom, an electron is ejected. From a higher energy shell, an electron falls into the energy level of missing electron and an excess energy which equals the energy difference in these shells is emitted as X-ray. It is called characteristic X-rays. Each element has its own characteristic X-ray wavelength.

To detect X-rays, an EDS detector is used. A charge pulse is created, following hitting of the resulting X-rays into EDS detector. First, the charge pulse to a voltage pulse and then the voltage pulse to a digital signal conversion processes are completed. Thereby, a count corresponding to the energy level is formed. As the counts increased, an X-ray spectrum is attained. The y-axis indicates the number of X-rays (counts) transformed to the digital signal by EDS detector. On the other hand, corresponding energy levels to these counts are demonstrated in the x-axis. There are three types of elemental mapping modes in EDS; spot, line and area. EDS measurements were taken via the SEM device which was shown in the SEM section. Elemental analyze and mapping operations in this work were performed with an Oxford Instruments brand EDS product which was integrated into JEOL JSM-6610 SEM device.

3.3.4 Optical characterization

Optical characterization refers to a study of the interaction of materials with electromagnetic radiation. These optical methods have some advantages as follows: sample preparation doesn't required and they are non-destructive in general. For instance, visible light doesn't modify the matter when interaction happens between light and matter due to its small energy.

When a light is dropped onto a semiconductor material, either photons are absorbed or transmitted by the semiconductor depending on the energy of photons and the band gap of the semiconductor. If the energy of incoming photons is equal or greater than the band gap of the semiconductor, the photons are absorbed, if not, the incident photons pass the semiconductor material without being absorbed.

To find the band gap value of a material, it has to be known the absorption coefficients of the samples at the corresponding wavelengths of photons and is found from the formula of

$$I = I_0 e^{-\alpha t} \tag{3.5}$$

where t is the thickness of the material and the transmittance (T) is equal to the transmitted light intensity (I) divided by incident light intensity (I_0) or equation can be re-written as

$$\alpha = \frac{-In(T)}{t} \tag{3.6}$$

for simplicity. The band gap energy of the samples can be determined by an equation so-called Tauc’s equation, but the first thing is to determine the absorption coefficient (α) by the formula in Equation 3.6. Following the determining of absorption coefficients, optical band gap of the films can be calculated with Tauc’s equation

$$\alpha hv = A(hv - E_G)^n \tag{3.7}$$

where A is a constant, hv is the incident photon energy, E_G is the optical band gap energy of sample and $n = 1/2$ for direct band gap semiconductor.

In our study, optical properties of all thin films were revealed by examining the optical transmission and PL measurements as well as determination of band gap values. Optical transmission and PL investigations of the samples at room temperature were performed in the wavelength range of 450 nm to 800 nm. Transmittance spectra of the samples were

recorded using the SpectraMax M5 device with a light source at 400 nm. The device is given in Figure 3.7.

Figure 3.7. SpectraMax M5 device.

Room temperature photoluminescence (RTPL) data was obtained by the Dongwoo Optron device operating at a Xe lamp with a power of 450 W in our work. The device is given in Figure 3.8.

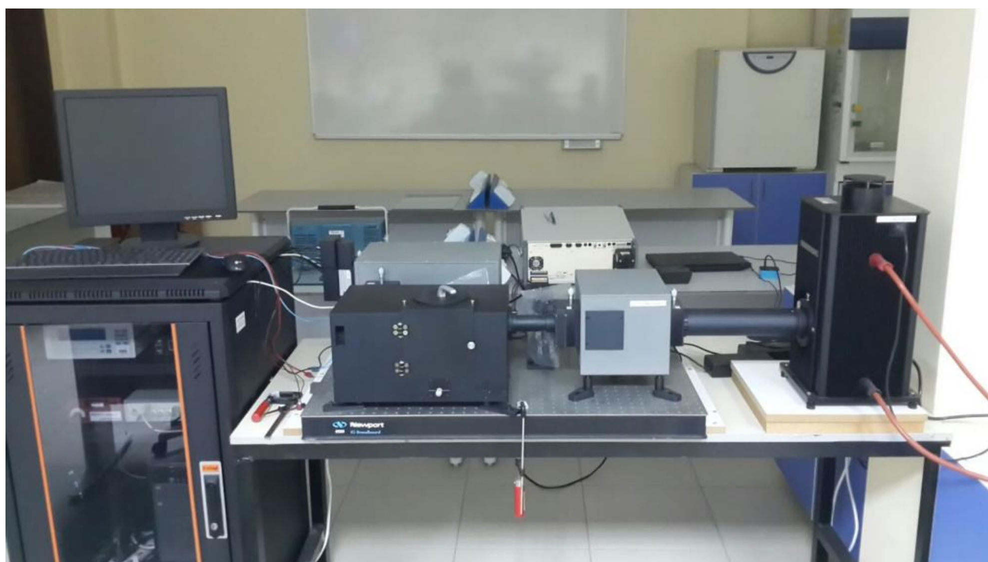

Figure 3.8. Dongwoo Optron device.

3.3.5 Electrical characterization

Hall effect method is utilized to characterize semiconductors in particular. Using the Hall effect experiment, the carrier density of samples can be determined. For this, Hall voltage (V_H), magnetic field (B), current passing in the material (I), electric charge (e) and thickness of the material (t) have to be known and then, placed in the following equations

$$n = \left(\frac{1}{e}\right)\left(\frac{IB}{V_H t}\right) \quad (3.8)$$

carrier density n for an n-type material and

$$p = \left(\frac{1}{e}\right)\left(\frac{IB}{V_H t}\right) \quad (3.9)$$

carrier density p for a p-type material can be found.

The method becoming a standard in order to calculate the resistivity of a semiconductor material is four-probe technique and a schematic representation of it can be seen in Figure 3.9.

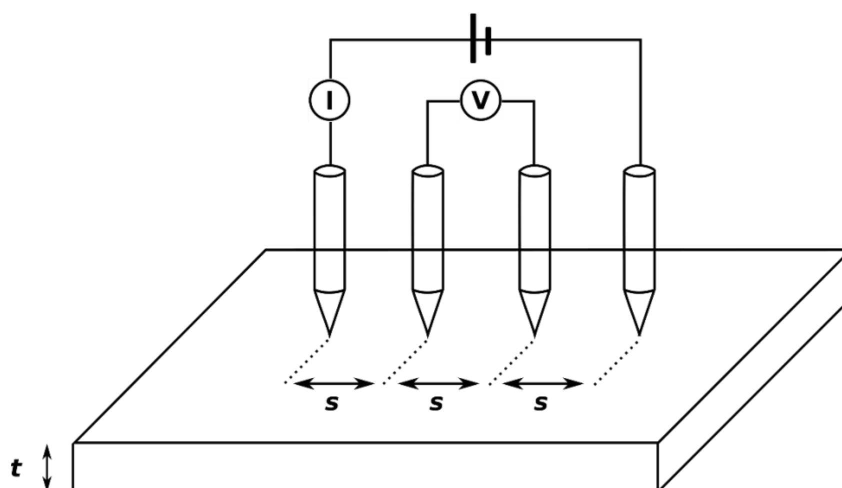

Figure 3.9. Schematic of four point probe method.

The resistivity of thin film can be measured in this way and the resistivity ρ is found by the following equation

$$\rho = 2\pi s \frac{V}{I} \tag{3.10}$$

where s is spacing between the probes, V is the potential difference between inner probes and I is the current passing through the sample.

In this study, the electrical characterization was carried out at room temperature using both Hall Effect experiments and four-probe method, to determine the carrier concentration and resistivity of the samples, respectively.

CHAPTER 4 RESULTS AND DISCUSSION

4.1 Investigation of Physical Properties of Ga-doped CdS Thin Films

4.1.1 XRD investigation of CdS:Ga thin films

In Figure 4.1.(a-e), XRD results of undoped CdS and doped Ga-doped CdS samples with 2 at.%, 4 at.%, 6 at.% and 8 at.% concentrations are shown. The identification of crystalline phases, calculation of crystallite sizes and determination of a and c lattice parameters of samples were performed by using XRD data. XRD pattern of undoped CdS sample is seen in Figure 4.1.a. The sample has a hexagonal wurtzite structure (JCPDS card no: 41-1049) and exhibits polycrystalline behaviour since it displays many peaks in the range of 2θ. These peaks locate at 25.0°, 26.7°, 28.4°, 36.7°, 43.9°, 47.9°, 52.0°, 53.0° and 58.5°, corresponding to (100), (002), (101), (102), (110), (103), (112), (201) and (202) planes, respectively. Two major distinct peaks corresponding to (101) and (112) planes are detected for all samples. The preferential orientation is along (101) plane. It was observed that the preferred orientation didn't change after incorporation of Ga-atoms. However, there is a slight increase in the peak intensity (101) till 6 at.% Ga concentration and this could be as a result of improvement in the crystal quality. On the other hand, the peak intensity of $Cd_{0.92}Ga_{0.08}S$ sample is lower than those of others. The reason for the decline of intensity is the deterioration of the crystal quality because Ga atoms occupy interstitially in the CdS host matrix, this results in rises in the lattice imperfections and changes in the unit cell volume. The interstitial occupation of Ga atoms in CdS causes more degradation of the crystal structure. A similar results found by Ravichandran and Senthamilselvi (2013). They found that crystal quality of the samples reduces after In concentration increases in CdS thin films. It is noted that there are no other peaks associated with secondary or impurity phases such as oxides of Cd or Ga. That indicates the successful dissolution of Ga atoms in the CdS matrix. The (100) and (002) planes were respectively used to calculate the lattice parameters a and c of undoped CdS and CdS:Ga samples. The obtained results are listed in Table 4.1. For undoped CdS, a value is found as 0.411 nm and c value is found as 0.668 nm. However, a reduction to 0.409 nm and 0.665 nm is happened for 2 at.% Ga incorporation into CdS. The reason is for that Ga ions occupy substitutionally within CdS structure due to the smaller ionic radius (0.062 nm) of Ga^{3+} ions in comparison to Cd^{2+} ions (0.097 nm). So, it is observed that volume of the unit cell decreases. However, further increasing in Ga concentration causes an increase in a and c values. It shows that Ga ions start to take interstitial position in CdS structure. As a result, it is seen that volume of the unit cell increases. Using (101) reflection plane, crystallite size of the samples are calculated with the help of Scherrer equation.

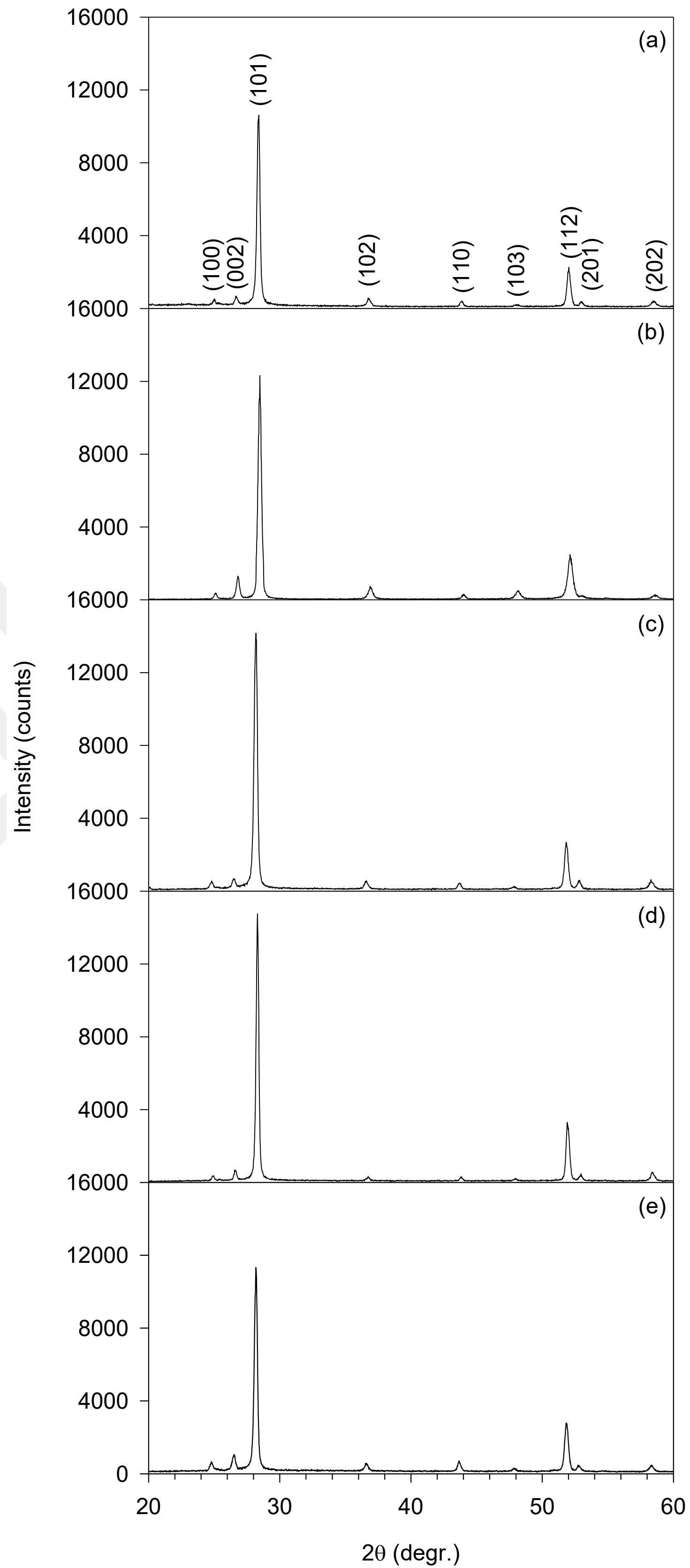

Figure 4.1. XRD data of **a)** CdS, **b)** $Cd_{0.98}Ga_{0.02}S$, **c)** $Cd_{0.96}Ga_{0.04}S$, **d)** $Cd_{0.94}Ga_{0.06}S$ and **e)** $Cd_{0.92}Ga_{0.08}S$ thin films.

The results are listed in Table 4.1. CdS sample has 31 nm crystallite size and crystallite sizes are almost same for CdS and Ga-doped CdS samples except for $Cd_{0.94}Ga_{0.06}S$ as is seen in Table 4.1. Moreover, crystallite size variations and grain size variations (see SEM images in Figure 4.2) of all CdS samples are quite similar.

Table 4.1. Lattice parameters (*a* and *c*) and the crystallite sizes of CdS, $Cd_{0.98}Ga_{0.02}S$, $Cd_{0.96}Ga_{0.04}S$, $Cd_{0.94}Ga_{0.06}S$, $Cd_{0.92}Ga_{0.08}S$ thin films.

Sample	Lattice parameters		Crystallite size *D* (nm)
	a **(nm)**	***c*** **(nm)**	
CdS	0.411	0.668	31
$Cd_{0.98}Ga_{0.02}S$	0.409	0.665	28
$Cd_{0.96}Ga_{0.04}S$	0.414	0.673	29
$Cd_{0.94}Ga_{0.06}S$	0.412	0.671	35
$Cd_{0.92}Ga_{0.08}S$	0.415	0.671	30

4.1.2 SEM investigation of CdS:Ga thin films

The surface morphology of the samples are investigated through SEM and their images are displayed in Figure 4.2.(a-f). In Figure 4.2.a, the SEM micrograph of CdS sample is shown. It is seen that many irregular shaped and different sized grains are observed. Additionally, the surface morphology is smooth and compact. The surface morphology regarding the sample of $Cd_{0.98}Ga_{0.02}S$ thin films is displayed in Figure 4.2.b. For the surface morphology in comparison to CdS sample, it is observed that grains become worm-like shape and smaller grain sizes having a smooth surface morphology are attained. Besides that, it is seen the surface is relatively uniform and continuous. The CdS sample with 4 at.% Ga-doping is displayed in Figure 4.2.c and some undefined shaped grains can be seen in addition to the worm-like shapes. As for $Cd_{0.94}Ga_{0.06}S$ sample, the surface morphology dramatically varies, seen in Figure 4.2.d. The grain shapes are partially rounded and the grain boundaries are very explicit. Moreover, the grain sizes grow. This result can be supported by the XRD pattern and the increment in grain size may be explained with enhancement in crystal quality. The undefined shapes appear also in here. The Figure 4.2.e shows the surface morphology of $Cd_{0.92}Ga_{0.08}S$ specimen. This morphology resembles

$Cd_{0.98}Ga_{0.02}S$ and $Cd_{0.96}Ga_{0.04}S$ morphology. The uniformly distributed grains over the surface can be easily noticed, indicating that a denser structure is formed. The SEM image with 60° tilt of $Cd_{0.96}Ga_{0.04}S$ is shown in Figure 4.2.f. The average sample thickness is determined as 1.5 µm. As a consequence, different Ga-dopings affected the surface morphology of CdS samples significantly.

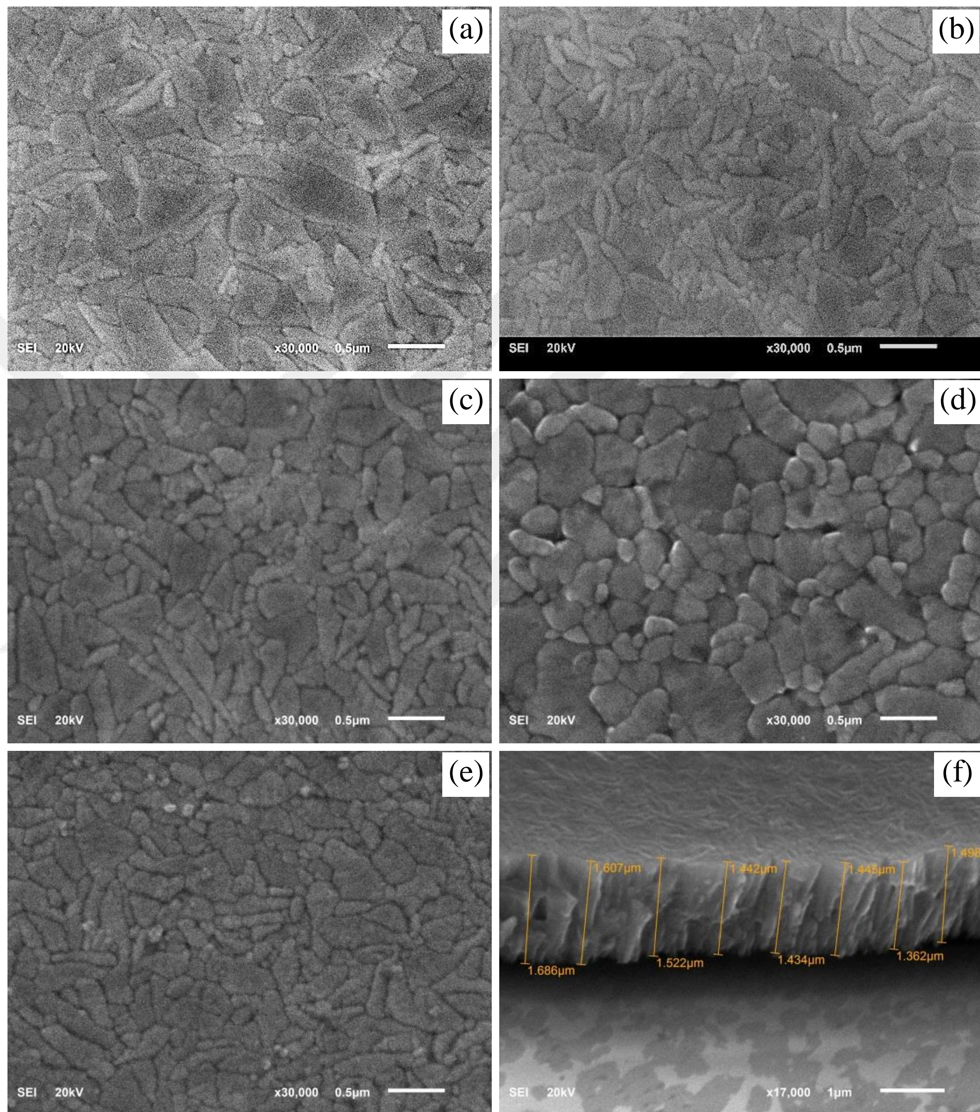

Figure 4.2. SEM images of **a)** CdS, **b)** $Cd_{0.98}Ga_{0.02}S$, **c)** $Cd_{0.96}Ga_{0.04}S$, **d)** $Cd_{0.94}Ga_{0.06}S$ and **e)** $Cd_{0.92}Ga_{0.08}S$ thin films. **f)** indicates 60° tilted view of $Cd_{0.96}Ga_{0.04}S$ sample.

4.1.3 EDS investigation of CdS:Ga thin films

EDS analysis of samples is performed. The typical spectrum for $Cd_{0.94}Ga_{0.06}S$ sample and actual atomic concentrations for CdS samples are presented in Figure 4.3 and Table 4.2, respectively. Figure 4.3 clearly indicates that there are almost no impurity atoms

in CdS host structure except for Ga atoms. While the Cd to S ratio is 0.96 for CdS, this ratio is low for all other CdS:Ga samples. It indicates that the formation of less stoichiometric films following Ga-dopings. It is realized from the Table 4.2 that the gradual increase of Ga concentration causes S deficiency.

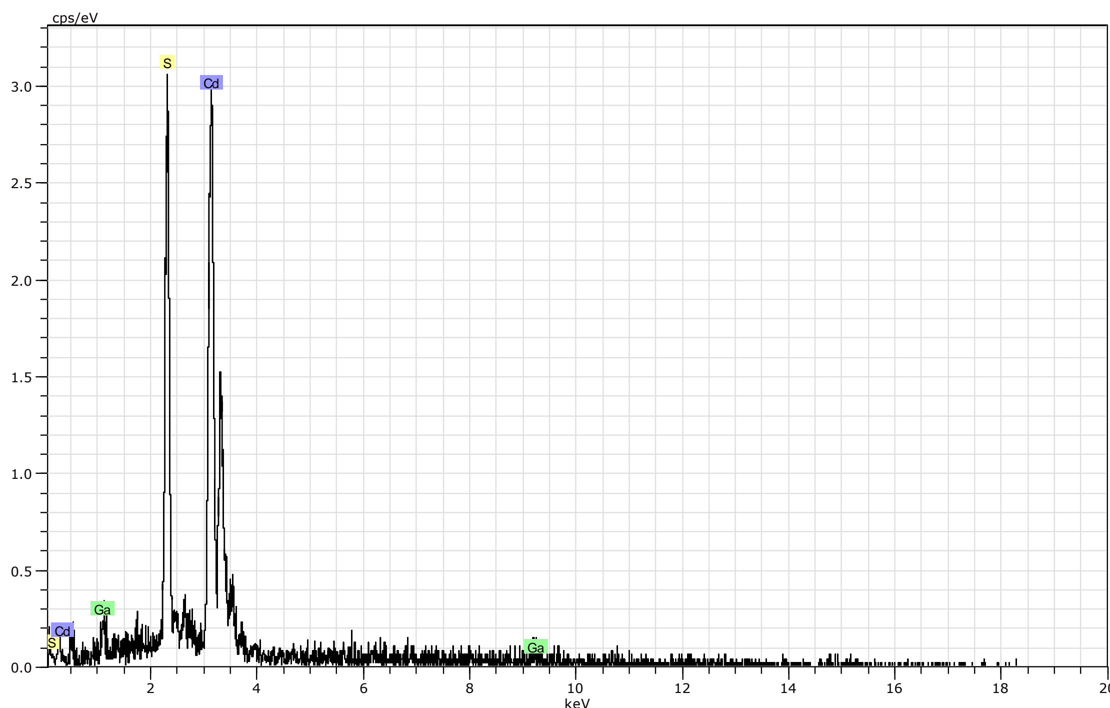

Figure 4.3. EDS spectrum of $Cd_{0.94}Ga_{0.06}S$ sample.

Table 4.2. Actual atomic concentrations of Cd, S, and Ga elements in CdS and $Cd_{0.98}Ga_{0.02}S$, $Cd_{0.96}Ga_{0.04}S$, $Cd_{0.94}Ga_{0.06}S$, $Cd_{0.92}Ga_{0.08}S$ thin films.

Samples	Cd	S	Ga
CdS	48.9	51.1	-
$Cd_{0.98}Ga_{0.02}S$	46.7	50.6	2.7
$Cd_{0.96}Ga_{0.04}S$	46.0	49.1	4.9
$Cd_{0.94}Ga_{0.06}S$	45.8	48.7	5.5
$Cd_{0.92}Ga_{0.08}S$	43.0	49.0	8.0

4.1.4 Optical investigation of CdS:Ga thin films

First optical investigation on CdS, $Cd_{0.98}Ga_{0.02}S$, $Cd_{0.96}Ga_{0.04}S$, $Cd_{0.94}Ga_{0.06}S$ and $Cd_{0.92}Ga_{0.08}S$ samples is taken by transmittance spectra and it is displayed in Figure 4.4. The transmittance values of all CdS thin films begin to increase rapidly at around 500 nm and their maximum values reach almost 70% as they approach 800 nm. It is clear that between 450 nm and 700 nm, a better transmittance is exhibited by $Cd_{0.98}Ga_{0.02}S$ and $Cd_{0.96}Ga_{0.04}S$ thin films in comparison to CdS thin films. On the other hand, the transmittance decreases when Ga content is increased to 6 at.% and 8 at.%. The improvement in the transmittance could indicate an enhanced crystal quality because of the lower defect density. The worsening in the transmittance may be attributed to crystal defects caused by Ga atoms. It can be deduced from the curve that 2 at.% Ga concentration causes a shifting of the absorption edge to the shorter wavelength (blue shift), in comparison to CdS sample. However, the other Ga-doping values cause a shift of the absorption edge to the longer wavelengths (red shift).

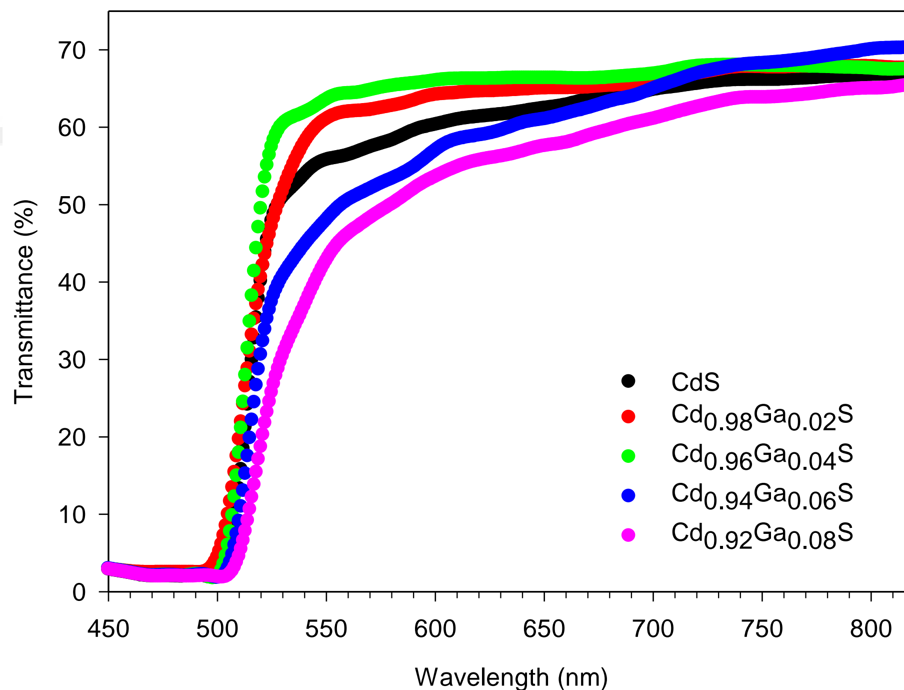

Figure 4.4. Transmittance data of CdS and $Cd_{0.98}Ga_{0.02}S$, $Cd_{0.96}Ga_{0.04}S$, $Cd_{0.94}Ga_{0.06}S$, $Cd_{0.92}Ga_{0.08}S$ thin films.

The band gap energies for all the samples are estimated by Tauc's plot method and the conclusions are shown in Figure 4.5. CdS specimen has a 2.42 eV band gap as seen and it is exactly the same as with the band gap value of single crystal CdS. But, the band

gap is calculated as 2.43 eV for $Cd_{0.98}Ga_{0.02}S$ sample. This widening in the energy gap of the CdS can be explained by Burstein-Moss effect which results from the increase in carrier concentration (Yılmaz, 2015a) and this result is consistent with both XRD data and electrical outcome. It demonstrates that Ga^{3+} ions take the substitutional position at the sites of Cd^{2+} within CdS matrix. After each Ga^{3+} atom occupation in CdS, an extra electron joins to the host matrix and contributes to enhance the carrier concentration.

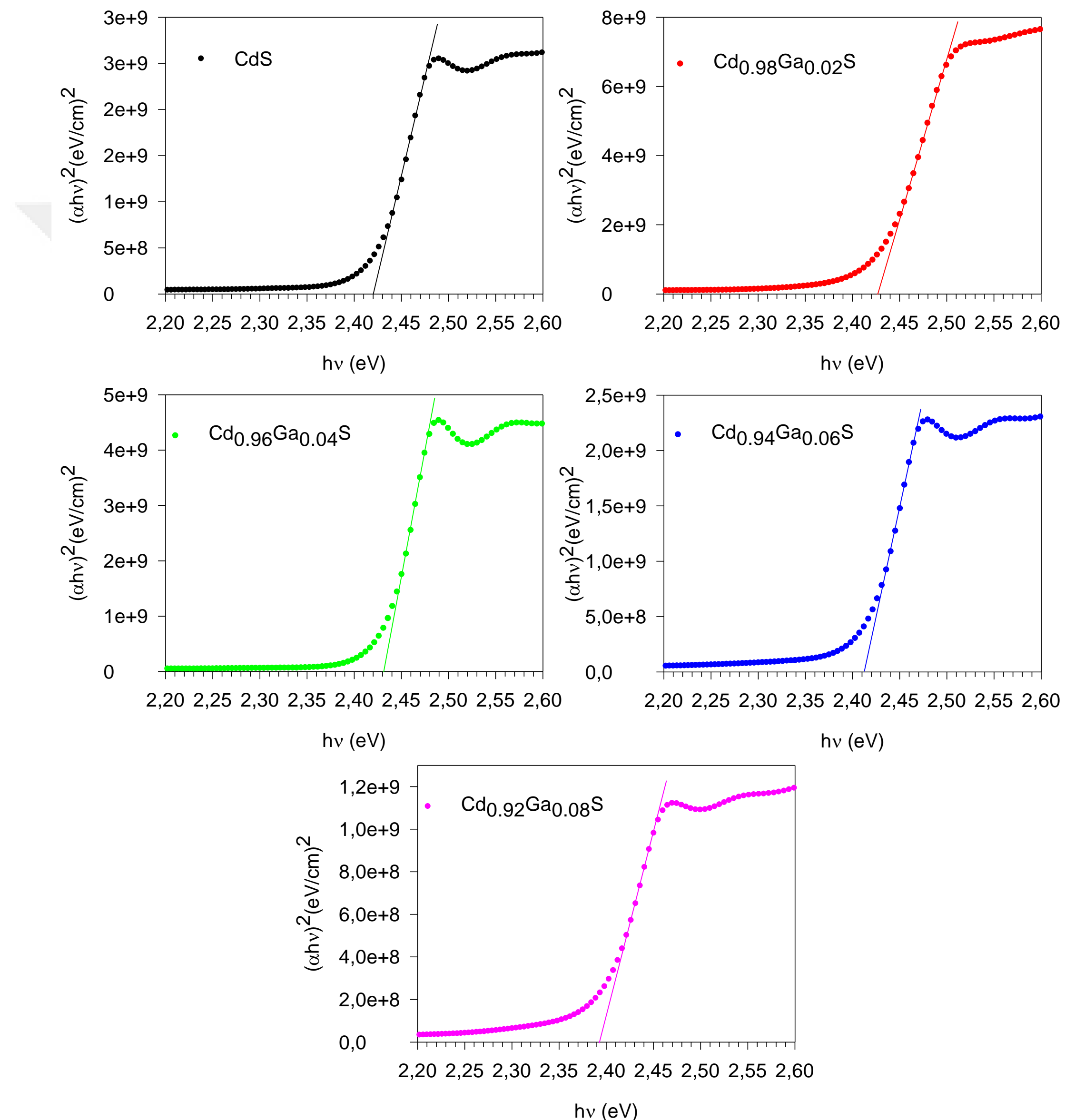

Figure 4.5. Tauc's plot of CdS and $Cd_{0.98}Ga_{0.02}S$, $Cd_{0.96}Ga_{0.04}S$, $Cd_{0.94}Ga_{0.06}S$ and $Cd_{0.92}Ga_{0.08}S$ thin films.

The sample of 4 at.% Ga-doped CdS has also a band gap energy of 2.43 eV and it is still higher in contrast to band gap energy of CdS. However, the Burstein-Moss effect is

not responsible for that because Ga^{3+} ions now can take place interstitially rather than substitutionally in CdS matrix. Therefore, the band gap broadening in comparison with CdS could be as a result of the increase of lattice strain due to the decrease in grain size till 4 at.% Ga concentration (Khallaf et al., 2009b). For the 6 at.% Ga concentration, band gap value is 2.41 eV. For 8 at.% Ga-doping, it is 2.39 eV. It was reported an analog drop for some studies (Khallaf, 2009b; Yan, 2015; Akintunde, 2000). The reason for a boost in band gap is that the incorporation of Ga^{3+} ions into the CdS matrix causes to form donor states. As the number of Ga atoms increase in the CdS, donor levels begin to degenerate. The donor levels combine with the conduction band of CdS and lead to the widening of the conduction band. Thereby, the band gap of the material narrows (Lokhande and Pawar, 1982).

Figure 4.6 shows RTPL data of CdS and CdS samples with 2 at.%, 4 at.%, 6 at.% and 8 at.% Ga concentrations. Three main peaks locating between 480-485 nm, 490-500 nm and 505-675 nm can be seen in the spectrum. The initial peak is associated with the host CdS and excitonic transitions or interstitial sulfur (I_S) vacancies could be the cause of the second peak (Kaur et al., 2014). However, a broad deep level emission (DLE) related to intrinsic defects like cadmium interstitials (I_{Cd}), sulfur vacancies (V_S), cadmium vacancies (V_{Cd}) is observed at the third peak. When compared to CdS sample, a similar intensity behaviour is observed from PL spectrum for $Cd_{0.98}Ga_{0.02}S$ sample excluding part of DLE band which corresponds between 510 and 555 nm. In this interval, the band intensity of CdS is higher than that of $Cd_{0.98}Ga_{0.02}S$. The decrease in band intensity may be a sign of the presence of lesser defects, resulting in a better crystal quality and XRD data supports this conclusion. The highest DLE band intensity among the samples is displayed by $Cd_{0.96}Ga_{0.04}S$ sample. Since Ga^{3+} ions hereafter make interstitial occupation rather than substitutional in the CdS matrix, it causes a rise in the density of I_{Cd} defects and thus leads to an increase in the DLE band intensity. In addition to that, radiative recombination after the entrance of Ga atoms into the matrix can lead to an enhancement in the DLE band intensity (Giribabu et al., 2013). However, last two Ga-dopings, 6 at.% and 8 at.%, cause a substantial drop in DLE intensity. A possible explanation for this could be the recombination of I_{Cd} defects with V_{Cd} defects (Yılmaz et al., 2015b). As a result, the population of these type of defects reduces, resulting diminishment in DLE band intensity. It is seen from XRD, Ga^{3+} ions still continue to enter into CdS matrix as interstitial, leading an increase in I_{Cd} defects. Furthermore, it is seen from EDS analysis that 6 at.% and 8 at.% Ga levels trigger more V_{Cd} defects in CdS structure. Muthusamy et al. (2014) found a similar descension behavior in PL intensity after 6 at.% Al doping is introduced in CdS.

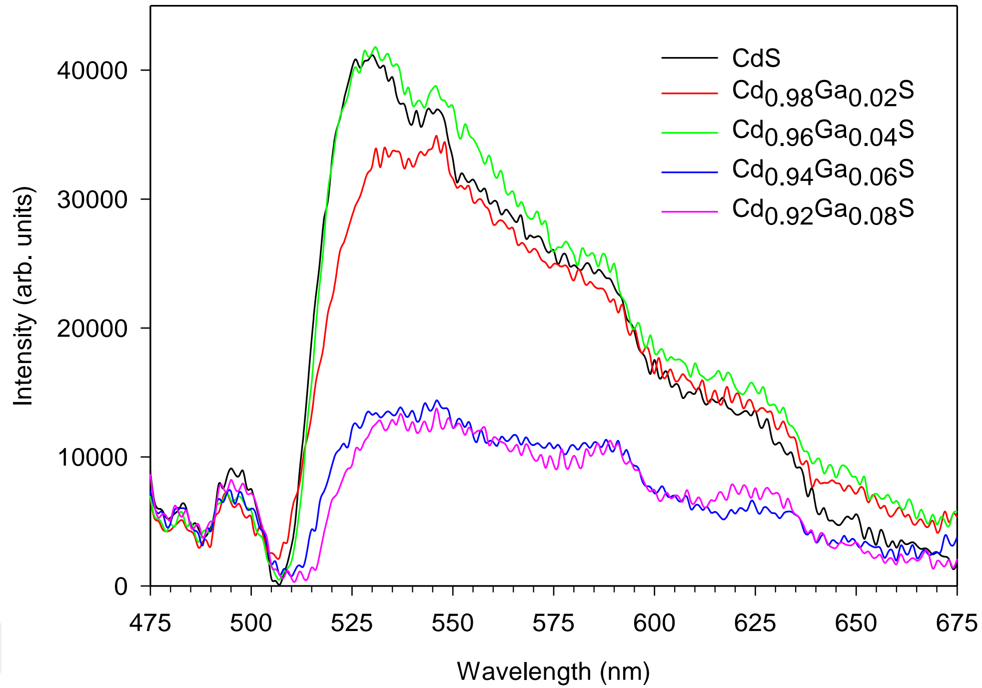

Figure 4.6. RTPL data of CdS and $Cd_{0.98}Ga_{0.02}S$, $Cd_{0.96}Ga_{0.04}S$, $Cd_{0.94}Ga_{0.06}S$ and $Cd_{0.92}Ga_{0.08}S$ thin films.

4.1.5 Electrical investigation of CdS:Ga thin films

The electrical properties of CdS:Ga thin films are investigated in terms of carrier concentration and resistivity. The results are listed in Table 4.3. For CdS sample, carrier concentration and resistivity values are 6.18 x 10^{10} cm^{-3} and 4.14 x 10^{4} Ω.cm, respectively. With 2 at.% Ga-doping, sample shows a carrier concentration of 9.91 x 10^{12} cm^{-3} and this is better than that of CdS one since Ga^{3+} ions occupy substitutional positions at the sites of Cd^{2+} ions, so the number of free carriers increases, leading an enhancement in carrier density. Moreover, the resistivity drops to the value of 1.53 x 10^{3} Ω.cm by virtue of the enhancement both in carrier concentration and crystal quality. After both 4 at.% and 6 at.% Ga-dopings, carrier concentrations of CdS thin films decreases to 1.75 x 10^{11} cm^{-3} and 7.89 x 10^{10} cm^{-3}, respectively. These declines can be attributed to interstitial replacements of Ga^{3+} ions in the CdS matrix. It is known, interstitially incorporated Ga^{3+} ions do not act as donors in CdS because they are not active as electrical. Instead of this, they behave as recombination centers and it results in fall in carrier concentration. As for resistivity values of $Cd_{0.96}Ga_{0.04}S$ and $Cd_{0.94}Ga_{0.06}S$ thin films, it is seen that they are 2.61 x 10^{4} Ω.cm and 3.62 x 10^{4} Ω.cm, respectively. The continuing rising in resistivity with increasing Ga-doping could be commented as a consequence of more scatterings at the grain boundaries. Among all the doped and undoped CdS samples, the minimum carrier concentration value takes place for 8 at.% Ga-dopings as 2.36 x 10^{10} cm^{-3}. On the other hand, the resistivity still

proceeds to increase gradually. The reason for both the decrement in carrier concentration and increment in resistivity could be in consequence of more deterioration happening in the crystal quality since more Ga atoms distort CdS structure after they occupy interstitially in CdS matrix.

Table 4.3. Carrier concentration and resistivity values of CdS and $Cd_{0.98}Ga_{0.02}S$, $Cd_{0.96}Ga_{0.04}S$, $Cd_{0.94}Ga_{0.06}S$, $Cd_{0.92}Ga_{0.08}S$ thin films.

Sample	Carrier concentration (cm^{-3})	Resistivity (Ω.cm)
CdS	6.18×10^{10}	4.14×10^{4}
$Cd_{0.98}Ga_{0.02}S$	9.91×10^{12}	1.53×10^{3}
$Cd_{0.96}Ga_{0.04}S$	1.75×10^{11}	2.61×10^{4}
$Cd_{0.94}Ga_{0.06}S$	7.89×10^{10}	3.62×10^{4}
$Cd_{0.92}Ga_{0.08}S$	2.36×10^{10}	4.51×10^{4}

4.2 Investigation of Physical Properties of (Ga-K)-co-doped CdS Thin Films

4.2.1 XRD investigation of (Ga-K)-co-doped CdS thin films

XRD analysis results of 1 at.%, 2 at.%, 3 at.%, 4 at.% and 5 at.% K-doped CdS:Ga samples are illustrated by Figure 4.7.(a-e). The CdS:Ga sample with 1 at.% K-doped is seen in Figure 4.7.a. It demonstrates that the sample is polycrystalline and has a hexagonal structure (matched with JCPDS card no: 41-1049). The peaks of (100), (102), (110), (103), (112) and (202) can be detected easily besides the most intense peak of (101). Also, when compared 2 at.% Ga-doped CdS sample (see Figure 4.1.b) with 1 at.% K-doped CdS:Ga sample, it isn't observed a variation in the peak intensity of (101). However, (002), (200) and (201) small peaks appear after 2 at.% K-doping and (101) peak intensity drops a little. A considerable reduction in (101) peak intensity occurs following 3 at.%, 4 at.% and 5 at.% doped of K in CdS:Ga samples and this could be attributed to degradation in crystal quality since K atoms enter interstitially into the host matrix. But it is one which is still predominant all over the others. On the other hand, (100) and (110) peak intensities show a rising trend. This indicates the existing of more random preferred orientation in the crystal. XRD data

indicates that there is no metallic peak for the elements of Ga and K and their probable compounds such as GaS for all the doping levels. It points out that Ga and K atoms dissolve in CdS host matrix successfully.

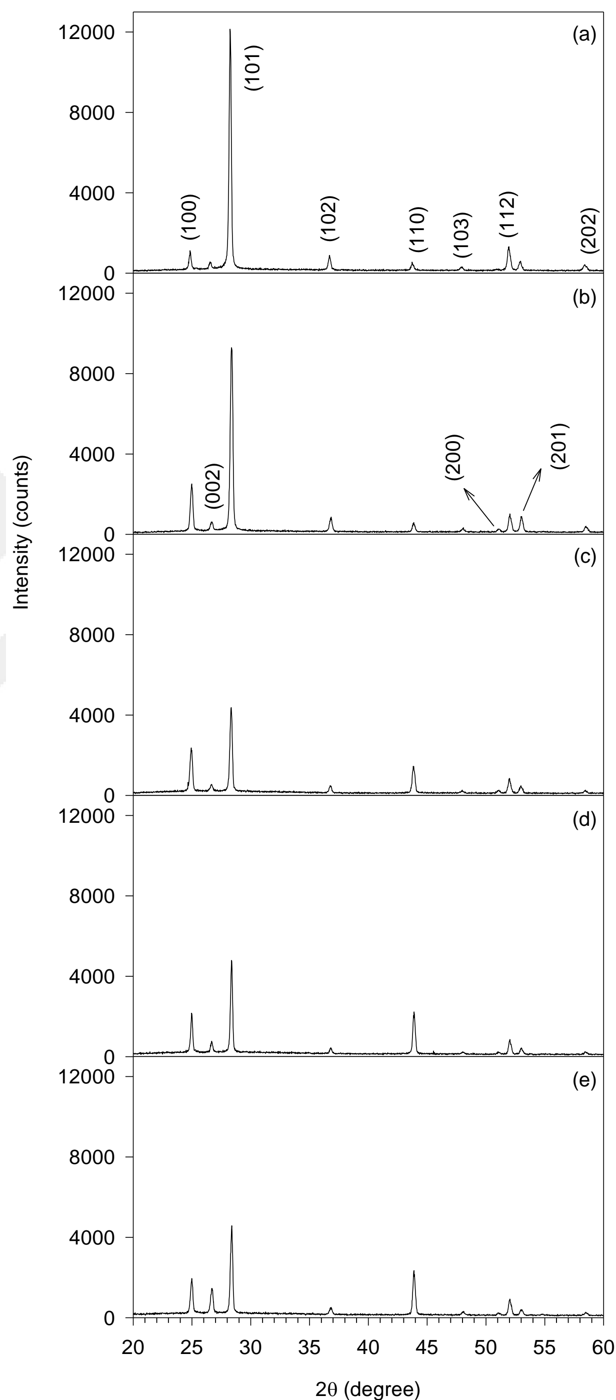

Figure 4.7. XRD data of **a)** 1 at.% K-doped $Cd_{0.97}Ga_{0.02}S$, **b)** 2 at.% K-doped $Cd_{0.96}Ga_{0.02}S$, **c)** 3 at.% K-doped $Cd_{0.95}Ga_{0.02}S$, **d)** 4 at.% K-doped $Cd_{0.94}Ga_{0.02}S$, **e)** 5 at.% K-doped $Cd_{0.93}Ga_{0.02}S$ thin films.

Table 4.4. Lattice parameters, crystallite sizes and thicknesses of 1 at.% K-doped $Cd_{0.97}Ga_{0.02}S$, 2 at.% K-doped $Cd_{0.96}Ga_{0.02}S$, 3 at.% K-doped $Cd_{0.95}Ga_{0.02}S$, 4 at.% K-doped $Cd_{0.94}Ga_{0.02}S$ and 5 at.% K-doped $Cd_{0.93}Ga_{0.02}S$ thin films.

Sample	**Lattice parameters**		**Crystallite size *D* (nm)**
	***a* (nm) (100)**	***c* (nm)**	
$Cd_{0.97}Ga_{0.02}K_{0.01}S$	0.412	0.671	39
$Cd_{0.96}Ga_{0.02}K_{0.02}S$	0.410	0.667	33
$Cd_{0.95}Ga_{0.02}K_{0.03}S$	0.410	0.668	36
$Cd_{0.94}Ga_{0.02}K_{0.04}S$	0.410	0.668	42
$Cd_{0.93}Ga_{0.02}K_{0.05}S$	0.410	0.668	39

The planes of (100) and (002) are used respectively to calculate a and c lattice parameters and the data is displayed in Table 4.4. In the previous section, it was said that the lattice parameters a and c were found in turn as 0.409 nm and 0.665 nm for 2 at.% Ga-doped CdS sample (see Table 4.1). They increase to the value of $a = 0.412$ nm and $c = 0.671$ nm after 1 at.% K-dopings, giving rise to a increase in lattice volume. The enlargement in the lattice volume could be explained by the substitutional entrance of the K^+ ions at the positions of Cd^{2+} because K^+ ions have a bigger ionic radius (0.133 nm) than that of Cd^{2+} ions (0.097 nm). The interstitial entrance can be also the reason for it as well since it causes an expansion in the lattice volume. The interstitial occupation of K^+ ions in the CdS sites was also reported by Klyuev et al. (2005). However, a and c values decrease to 0.410 nm and 0.668 nm respectively for 2 at.%, 3 at.%, 4 at.% and 5 at.% K-dopings. Nonetheless, they are bigger than that of 2 at.% Ga-doped CdS one which means that K^+ ions continue to incorporate into the CdS structure interstitially. A potential answer to the drop may be the increase of strain that originates from defects and lattice distortions. In addition to that, some defects like V_S can be the reason for the contraction in lattice parameters (Hemathangam et al., 2016).

Via the Scherrer's formula and using (101) plane, crystallite sizes are calculated for all samples and tabulated in Table 4.4. In the previous section again, it was represented that the crystallite size was 28 nm for $Cd_{0.98}Ga_{0.02}S$ sample. It is clear that all K-doping values affect the crystallite size of the samples. Additionally, 4 at.% K-doped $Cd_{0.94}Ga_{0.02}S$ has the largest D value among the other samples due to the increasing crystal volume.

4.2.2 SEM investigation of (Ga-K)-co-doped CdS thin films

SEM investigation results are showed in Figure 4.8.(a-e). It was mentioned before that 2 at.% Ga-doped CdS sample (see Figure 4.2.b) is composed of many small and irregular shaped grains. This sample has smooth surface morphology and contains no pinholes. However, the micrograph of 1 at.% K-doped $Cd_{0.97}Ga_{0.02}S$ sample is illustrated in Figure 4.8.a and the worm-like shaped grains are apparent. In addition, there are some grains with undefined shapes and polygon shapes. Also, the sample surface morphology is smooth and continuous. Figure 4.8.b indicates 2 at.% K-doped $Cd_{0.96}Ga_{0.02}S$ sample. As seen from the view, there are mostly grains with triangular-like shapes. But also the existence of the polygon shaped grains throughout the surface can be noticed even though they are few numbers. It was observed that the grain size increases by comparison to 1 at.% K-doped $Cd_{0.97}Ga_{0.02}S$ sample as a consequence of a rise in the crystal size after incorporation of increasing K level. Furthermore, the grain boundaries become more distinctive. Figure 4.8.c shows the SEM image of 3 at.% K-doped $Cd_{0.95}Ga_{0.02}S$ sample. Undefined and polygon shaped grains are still dominant as seen. In addition, surface roughness is high and grain size decreases. Figure 4.8.d displays SEM image of 4 at.% K-doped $Cd_{0.94}Ga_{0.02}S$ sample. The density of triangular-like shaped grains diminishes and most of grains are composed of now both undefined and polygon like shaped grains. A relatively smooth and compact surface morphology are achieved when compared to all K-doping levels and moreover, the surface roughness is notably low. As for 5 at.% K-doped $Cd_{0.93}Ga_{0.02}S$ sample from Figure 4.8.d, the biggest grain size is attained. Also, it is seen that grains are dispersed uniformly and continuously on the sample's surface. The grain boundary is very distinct for this sample.

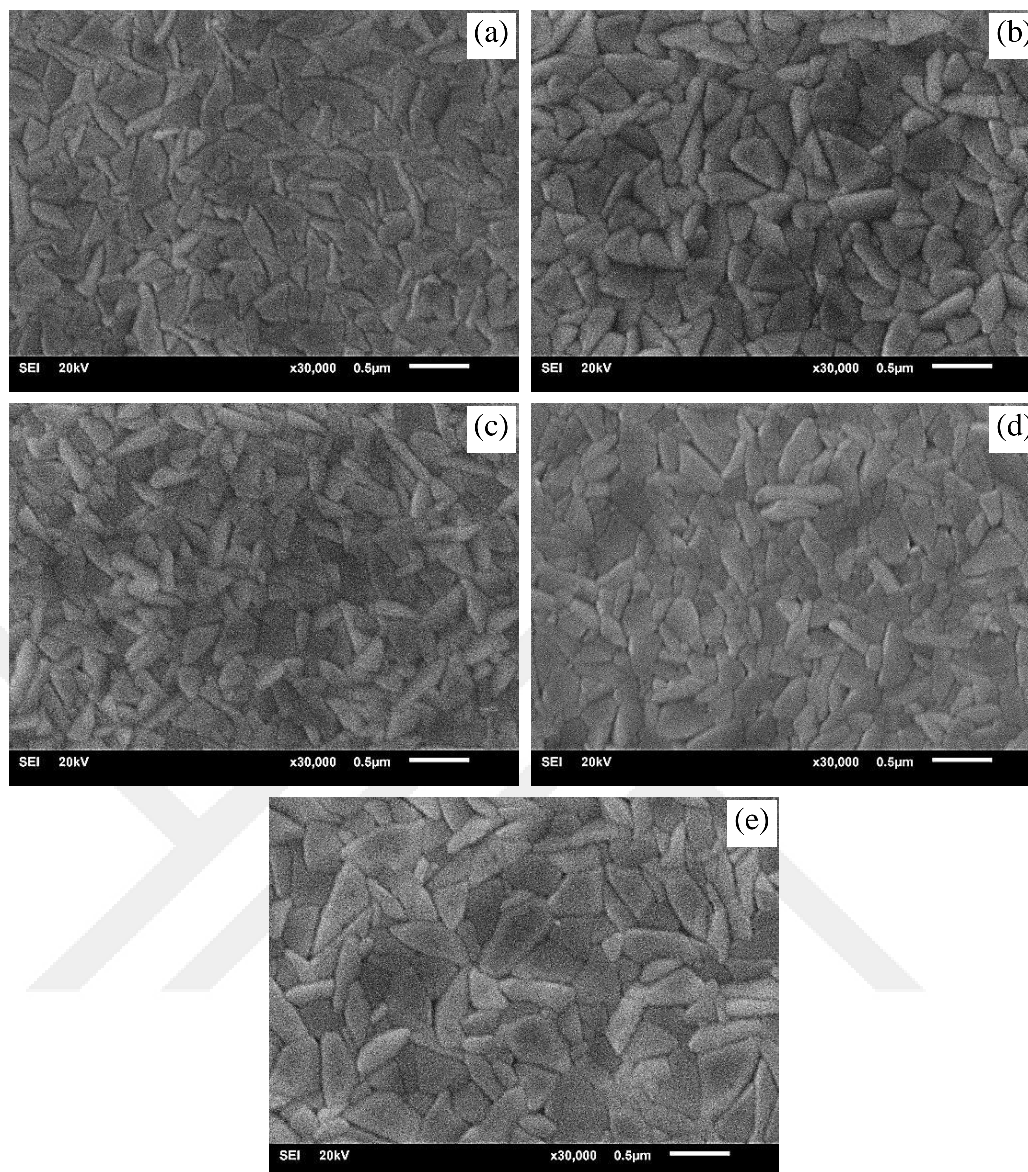

Figure 4.8. SEM plain views of **a)** 1 at.% K-doped $Cd_{0.97}Ga_{0.02}S$, **b)** 2 at.% K-doped $Cd_{0.96}Ga_{0.02}S$, **c)** 3 at.% K-doped $Cd_{0.95}Ga_{0.02}S$, **d)** 4 at.% K-doped $Cd_{0.94}Ga_{0.02}S$, and **e)** 5 at.% K-doped $Cd_{0.93}Ga_{0.02}S$ thin films.

4.2.3 EDS investigation of (Ga-K)-co-doped CdS thin films

Investigation of chemical compositions for 1 at.%, 2 at.%, 3 at.%, 4 at.% and 5 at.% K-doped CdS:Ga samples are performed. Furthermore, a typical EDS spectrum of 4 at.% K-doped CdS:Ga sample is displayed in Figure 4.9 and Ga, K, Cd and S elements are clearly seen in the spectrum which means it is the proof of presence both Ga and K atoms in the host structure of CdS. It is no surprise that S content is rich in contrast to Cd content in thin films by virtue of the chosen molar ratio for Cd/S (1:2). In order to get a better optical properties for the sample, this ratio is selected. The highest Cd/S ratio is found as 0.97 for 2 at.% K-doped sample. It indicates the formation of the best stoichiometric thin films. Less

stoichiometric thin films are formed after 4 at.% and 5 at.% K-dopings, Cd/S ratio is 0.87 for these two. It can be seen that the actual concentrations of Ga and K in the CdS are near to the nominal values.

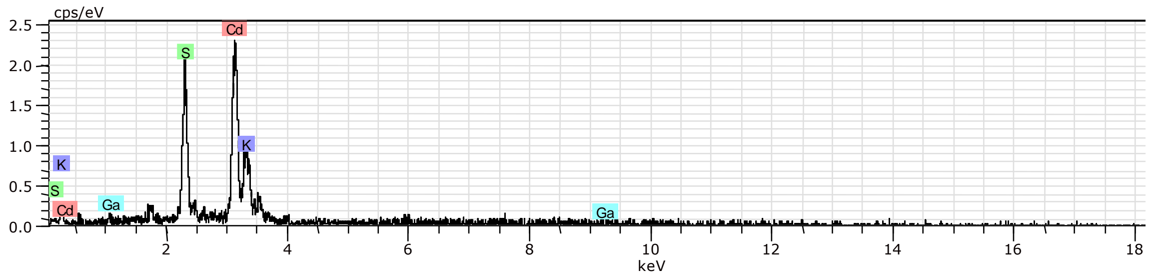

Figure 4.9. EDS spectrum of 4 at.% K-doped $Cd_{0.94}Ga_{0.02}S$ thin films.

Table 4.5. Actual and nominal atomic contents of Cd, S, Ga, and K in 1 at.% K-doped $Cd_{0.97}Ga_{0.02}S$, 2 at.% K-doped $Cd_{0.96}Ga_{0.02}S$, 3 at.% K-doped $Cd_{0.95}Ga_{0.02}S$, 4 at.% K-doped $Cd_{0.94}Ga_{0.02}S$ and 5 at.% K-doped $Cd_{0.93}Ga_{0.02}S$ thin films.

Sample	**measured at.%**			
	Ga	K	Cd	S
$Cd_{0.97}Ga_{0.02}K_{0.01}S$	2.3	1.5	46.6	49.6
$Cd_{0.96}Ga_{0.02}K_{0.02}S$	2.4	2.7	46.7	48.2
$Cd_{0.95}Ga_{0.02}K_{0.03}S$	2.7	3.7	44.8	48.8
$Cd_{0.94}Ga_{0.02}K_{0.04}S$	2.5	4.1	43.5	49.9
$Cd_{0.93}Ga_{0.02}K_{0.05}S$	2.8	5.1	42.9	49.2

EDS element mapping conclusions in Figure 4.10 shows us the distribution of elements of Cd, S, Ga and K on the CdS surface. In Figure 4.10.a, SEM plan view of 4 at.% K-doped sample is demonstrated together with the simultaneous EDS mapping of all the elements. Additionally, individual elemental mapping of these is displayed in the same figure. It can be said that they are distributed throughout the surface of CdS homogeneously.

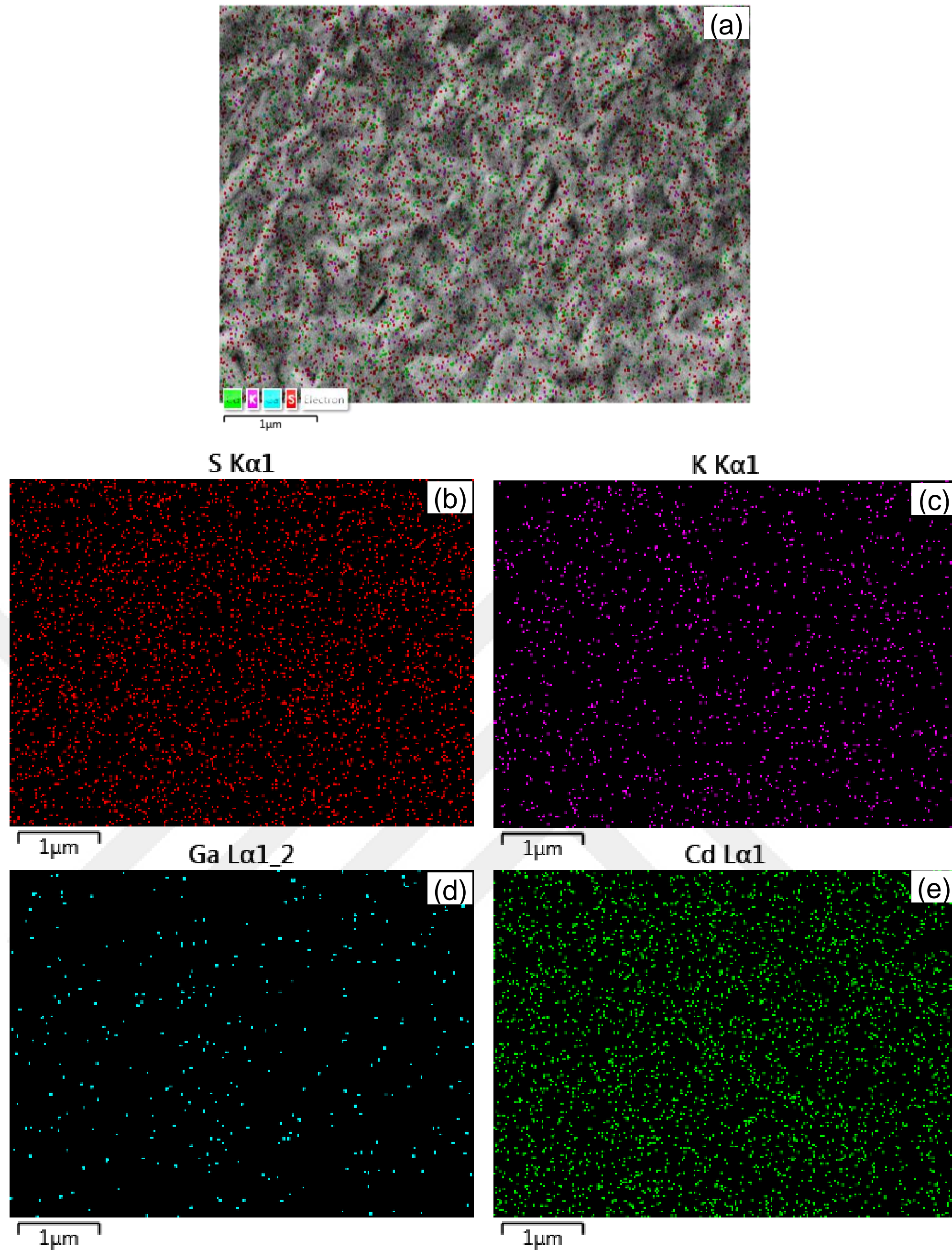

Figure 4.10. a) SEM plan view of 4 at.% K-doped $Cd_{0.94}Ga_{0.02}S$ thin films including mapping of S, K, Ga and K elements on the surface, individual mapping results of **b)** S, **c)** K, **d)** Ga and **e)** Cd elements.

4.2.4 Optical investigation of (Ga-K)-co-doped CdS fhin films

Transmittance curves of all K-doped samples which have 1 at.%, 2 at.%, 3 at.%, 4 at.% and 5 at.% doping levels are illustrated in Figure 4.11. The 1 at.% and 2 at.% K-doped samples have the lowest transmittance values among the other samples, that is nearly 75%. However, these are higher than that of 2 at.% Ga-doped CdS (see Figure 4.4) sample, which has almost 65% transmittance value. That is explainable by happening of the less

scattering from the grain boundaries by virtue of the grain growth (confirmed by SEM images) (Yılmaz et al., 2015b). An increase in transmittance takes place following 3 at.% and 4 at.% K-dopings and transmittance values of both approach to 85% in the visible region. 5 at.% K-doped films exceed 80% before the absorption edge. However, 5 at.% K-doping level causes a significant drop in transmission. It is probably owing to the poor degree of crystallinity. As a consequence, an increase in K concentration improves the transmittance of samples compared to 2 at.% Ga-doped CdS. Absorption edge shifts towards to the shorter wavelengths by 1 at.%, 2 at.%, 3 at.%, 4 at.% and 5 at.% K-dopings in comparison to 2 at.% Ga-doped CdS.

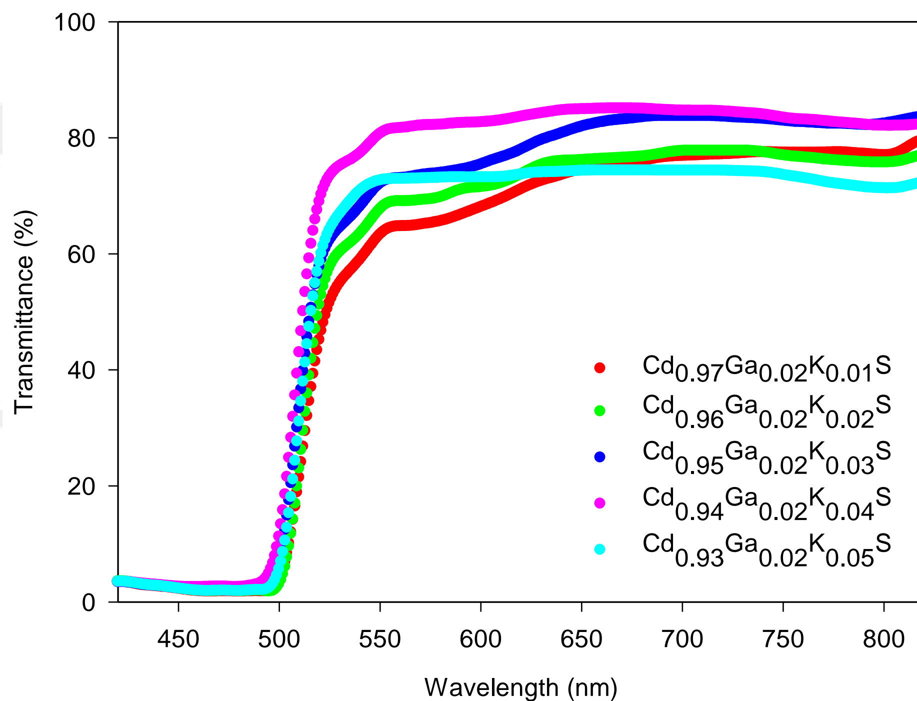

Figure 4.11. Transmission plots of 1 at.% K-doped $Cd_{0.97}Ga_{0.02}S$, 2 at.% K-doped $Cd_{0.96}Ga_{0.02}S$, 3 at.% K-doped $Cd_{0.95}Ga_{0.02}S$, 4 at.% K-doped $Cd_{0.94}Ga_{0.02}S$ and 5 at.% K-doped $Cd_{0.93}Ga_{0.02}S$ thin films.

Band gaps of all the samples are determined and presented in Figure 4.12. The band gap of 1 at.% and 2 at.% K-doped CdS:Ga samples are the same (2.44 eV) and it is slightly wider than that of 2 at.% Ga-doped CdS (2.43 eV) (see Figure 4.5). However, band gap value ascends to 2.45 eV for the case of 3 at.%, 4 at.% and 5 at.% K-dopings. This increase cannot be attributed to Burstein-Moss effect since carrier concentrations of all the K-doped CdS:Ga samples have lower than that of the 2 at.% Ga-doped CdS sample. The reason for this could be related to the increase of internal strain which originates from the

interstitial occupation of K atoms in the host structure (Yellaiah et al., 2013). It is known that the interstitial entrance into the structure leads to an enlargement in the band gap of the sample (Vettumperumal et al., 2015).

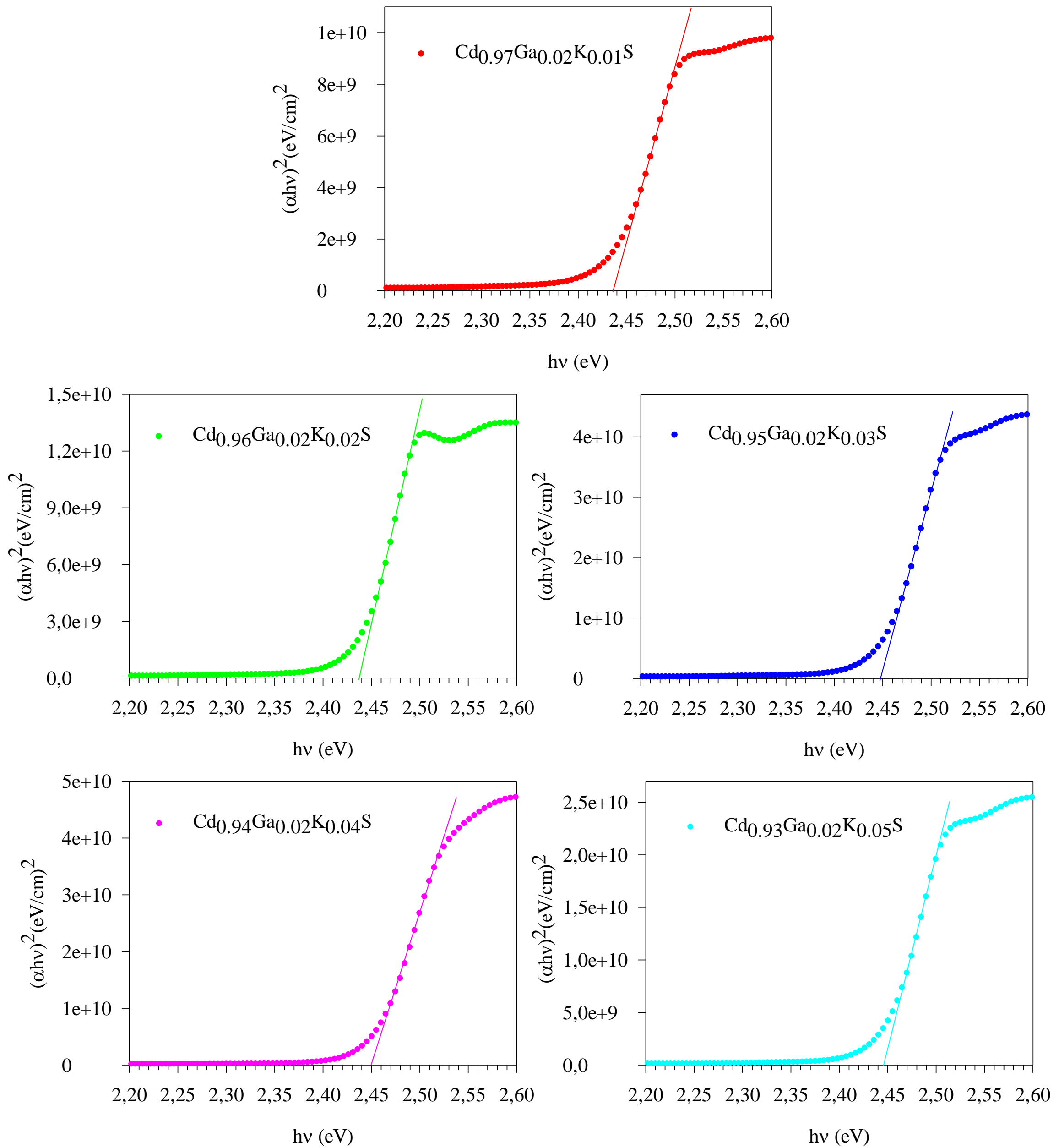

Figure 4.12. Tauc's plot conclusions of 1 at.% K-doped $Cd_{0.97}Ga_{0.02}S$, 2 at.% K-doped $Cd_{0.96}Ga_{0.02}S$, 3 at.% K-doped $Cd_{0.95}Ga_{0.02}S$, 4 at.% K-doped $Cd_{0.94}Ga_{0.02}S$ and 5 at.% K-doped $Cd_{0.93}Ga_{0.02}S$ thin films.

PL investigation of 1 at.%, 2 at.%, 3 at.%, 4 at.% and 5 at.% K-doped CdS:Ga thin films is seen in Figure 4.13. The RTPL graph of 2 at.% Ga-doped CdS is given in Figure

4.6 and there are mainly three peaks for this sample. The first is between 480-485 nm and it is because of the host CdS. The second is between 490-500 nm and related to I_S defects or green band which is the result of the excitonic transition (Kaur et al., 2014). The third is associated with DLE band. It results from the intrinsic defects such as I_{Cd} in addition to V_{Cd} and V_S. The intensity of the first and the second peaks variates a little for all the samples. As for DLE band, 1 at.% K-doped $Cd_{0.97}Ga_{0.02}S$ and 2 at.% K-doped $Cd_{0.96}Ga_{0.02}S$ samples have slightly less band intensity in comparison to $Cd_{0.98}Ga_{0.02}S$ sample. It indicates a decrement in defect levels and that means the formation of more stoichiometric films (supported by the EDS result). K concentration causes an increment in the DLE band intensity for the further K levels (3 at.%, 4 at.% and 5 at.%), particularly for 4 at.% K level, when compared with the $Cd_{0.98}Ga_{0.02}S$ one (see Figure 4.6). A possible reason for that could be the increasing number of defects such as I_{Cd}, V_{Cd} and interstitial potassium (I_K) after the substitutional incorporation of Ga atoms in CdS matrix. The radiative recombination due to a boost in the K level can be concluded a rise in the DLE intensity (Poornaprakash et al., 2016). Moreover, increasing carrier concentration in the conduction band may be another reason for it (Klyuev et al., 2005). However 5 at.% K content leads to a reduction in the DLE intensity. It could be explained by the decreasing number of defects such as I_{Cd} and V_{Cd} due to the recombination of these types of defect.

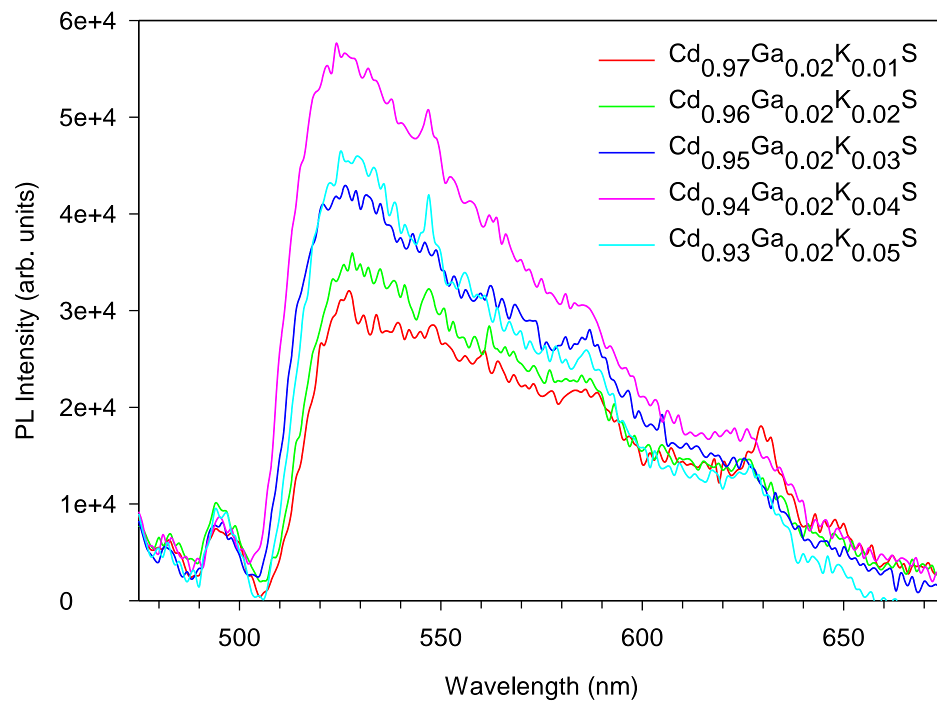

Figure 4.13. RTPL graphs of 1 at.% K-doped $Cd_{0.97}Ga_{0.02}S$, 2 at.% K-doped $Cd_{0.96}Ga_{0.02}S$, 3 at.% K-doped $Cd_{0.95}Ga_{0.02}S$, 4 at.% K-doped $Cd_{0.94}Ga_{0.02}S$ and 5 at.% K-doped $Cd_{0.93}Ga_{0.02}S$ thin films.

4.2.5 Electrical investigation of (Ga-K)-co-doped CdS thin films

Carrier concentration and electrical resistivity of 1 at.%, 2 at.%, 3 at.%, 4 at.% and 5 at.% K-doped CdS:Ga samples are tabulated in Table 4.6. The sample of $Cd_{0.98}Ga_{0.02}S$ had 9.91 x 10^{12} cm^{-3} carrier concentration and 1.53 x 10^{3} Ω.cm (see Table 4.3). A carrier density of 4.02 x 10^{11} cm^{-3} and a resistivity of 2.54 x 10^{4} Ω.cm are attained for 1 at.% K-doped Cd:Ga sample. The reason for the reduction in carrier concentration could be that K atoms take a position in CdS:Ga samples interstitially. It results in deterioration in the lattice, leading strain formation in the host matrix. Consequently, carrier density reduces (Park and Han, 2015) and hence, resistivity increases. Furthermore, the population of free carriers scattering from the grain boundaries ascends and this causes a drop in conductivity. Almost no change in the resistivity after 2 at.% K concentration, but a slight increase in the carrier concentration to 5.06 x 10^{11} cm^{-3} is reached. However, in the case of 3 at.%, 4 at.% and 5 at.% K concentrations, it ended up with a significant improvement in the carrier concentrations and a drop in the resistivity values. Especially, 4 at.% K concentration sample has the best carrier concentration (5.90 x 10^{12} cm^{-3}) as well as the lowest resistivity (8.29 x 10^{3} Ω.cm). Such enhancement can be interpreted by the increase in I_K centers. Because these interstitial K atoms play a role as donor centers at room temperature and contribute to the structure by giving an electron (Klyuev et al., 2005). That is, when K atoms increase in the $Cd_{0.98}Ga_{0.02}S$ matrix, the number of free electrons becomes much more. Therefore, the resistivity of the sample also decreases. Carrier density lessens slightly and resistivity increases a little for 5 at.% K-doped CdS:Ga thin films.

Table 4.6. Carrier concentration and resistivity values of 1 at.% K-doped $Cd_{0.97}Ga_{0.02}S$, 2 at.% K-doped $Cd_{0.96}Ga_{0.02}S$, 3 at.% K-doped $Cd_{0.95}Ga_{0.02}S$, 4 at.% K-doped $Cd_{0.94}Ga_{0.02}S$ and 5 at.% K-doped $Cd_{0.93}Ga_{0.02}S$ thin films.

Sample	Carrier concentration (n) (cm^{-3})	Resistivity (ρ) (Ω.cm)
$Cd_{0.97}Ga_{0.02}K_{0.01}S$	4.02×10^{11}	2.54×10^{4}
$Cd_{0.96}Ga_{0.02}K_{0.02}S$	5.06×10^{11}	2.59×10^{4}
$Cd_{0.95}Ga_{0.02}K_{0.03}S$	3.90×10^{12}	9.12×10^{3}
$Cd_{0.94}Ga_{0.02}K_{0.04}S$	5.90×10^{12}	8.29×10^{3}
$Cd_{0.93}Ga_{0.02}K_{0.05}S$	4.86×10^{12}	9.31×10^{3}

CHAPTER 5 CONCLUSIONS

In this thesis, CdS:Ga and CdS:(Ga, K) thin films were constructed on glass substrates at 400 °C via spray pyrolysis and influences of different concentrations of Ga and Ga-K elements on the physical properties of CdS thin films were characterized by XRD, SEM, EDS, PL, Hall effect and resistivity measurements.

The level of Ga was changed from 0 at.% to 8 at.% in steps of 2 at.% in order to prepare CdS:Ga thin films. XRD showed that the prepared CdS:Ga thin films were at hexagonal crystal structure with the preferred orientation along the (101). SEM micrographs indicated a considerable variation at the surface morphology after Ga incorporation, particularly for 6 at.% sample. EDS analysis showed the formation of non-stoichiometric films with increasing of Ga content. As for the transmittance of the samples, in comparison with the transmittance value of pure CdS, the transmittance increased after 2 at.% and 4 at.% Ga-doping but it decreased after 6 at.% and 8 at.% Ga-doping. The band gap of CdS specimen was calculated as 2.42 eV. The band gap increased to 2.43 eV for 2 at.% and 4 at.% Ga-dopings whereas it was found as 2.41 eV and 2.39 eV for 6 at.% and 8 at.% Ga-dopings, respectively. As a result of the electrical analysis of the samples, the best values both for the carrier concentration and resistivity were found respectively as 9.91×10^{12} cm^{-3} and 1.53×10^{3} Ω.cm. Among different Ga concentrations, the chosen one was 2 at.% due to displaying better optical and electrical conclusions than those of the others and therefore, this value was kept fixed for the further study which was co-doped with K.

For the dual doping, the level of K was varied from 1 at.% to 5 at.% in steps of 1 at.% to prepare CdS:(Ga, K) thin films. XRD displayed that the presence of hexagonal crystal structure for the prepared CdS:(Ga, K) thin films with a strong (101) preferred orientation. EDS indicated that the best stoichiometric film was obtained with the CdS:Ga sample which was doped with 2 at.% K. As for the transmittance of the samples, it increased with increasing K content and reached the maximum for 4 at.% K content. The band gap of CdS:Ga (2 at.%) was calculated as 2.43 eV. The band gap increased to 2.44 eV for 1 at.% and 2 at.% K-dopings and 2.45 eV for 3 at.%, 4 at.% and 5 at.%. The electrical measurements showed that the best carrier concentration and the lowest resistivity were achieved as 5.90×10^{12} cm^{-3} and 8.29×10^{3} Ω.cm, respectively for 4 at.% K-doping. In conclusion, 4 at.% (Ga-K)-co-doped CdS thin films exhibited the best optical and electrical behaviors that made it a suitable candidate for optoelectronic applications and solar cells.

REFERENCES

Adachi S. 2005. Properties of group-IV, III-V and II-VI semiconductors. John Wiley & Sons.

Akintunde JA. 2000. Dual impurity doping of buffer solution grown cadmium sulphide thin films: electrical and optical properties. Journal of Materials Science: Materials in Electronics, 11(6): 503-508.

Altosaar M, Ernits K, Krustok J, Varema T, Raudoja J, Mellikov E. 2005. Comparison of CdS films deposited from chemical baths containing different doping impurities. Thin Solid Films, 480-481: 147-150.

Anbarasi M, Nagarethinam VS, Balu AR. 2014. Investigations on the structural, morphological, optical and electrical properties of undoped and nanosized Zn-doped CdS thin films prepared by a simplified spray technique. Materials Science-Poland, 32(4): 652-660.

Anbarasi M, Nagarethinam VS, Baskaran R, Narasimman V. 2016. Studies on the structural, morphological and optoelectrical properties of spray deposited CdS:Pb thin films. Pasific Science Review A: Natural Science and Engineering, 18(1): 72-77.

Atay F, Bilgin V, Akyuz I, Kose S. 2003. The effect of In doping on some physical properties of CdS films. Materials Science in Semiconductor Processing, 6(4): 197-203.

Bala V, Tripathi SK, Kumar R. 2014. Correlation of photoluminescence quenching with Charge Transport in group III (Al, Ga & In) elements doped CdS/PVA NCs: Experimental and First Principles Studies. Mater Lett, 132: 38-40.

Bala V, Tripathi SK, Kumar R. 2015. Optical properties of Ga and In doped CdS nanocomposites: An experimental and first principles study. Mater Lett, 149: 18-21.

Bedir M, Öztaş M, Çelik SS, Özdemir T. 2014. Effect of boric acid content on the structural and optical properties of MnS films prepared by spray pyrolysis technique. Acta Physica Polonica A, 126: 840-844.

Benick J, Richter A, Müller R, Hauser H, Feldmann F, Krenckel P, Riepe S, Schindler F, Schubert MC, Hermle M, Bett AW, Glunz SW. 2017. High-efficiency n-type HP mc silicon solar cells. IEEE Journal of Photovoltaics, 7(5): 1171-1175.

Bidadi H, Kalafi M, Tajalli H, Bairamov AI, Dzhafarov TD. 1996. Diffusion and interaction of Group I impurities with vacancies in CdS thin films. Optical Materials, 6(1-2): 27-33.

Cai J, Jie J, Jiang P, Wu D, Xie C, Wu C, Wang Z, Yu Y, Wang L, Zhang X, Peng Q, Jiang Y. 2011. Tuning the electrical transport properties of n-type CdS nanowires via Ga doping and their nano-optoelectronic applications. Physical Chemistry Chemical Physics, 13(32): 14663-14667.

Challa KK, Magnone E, Kim ET. 2012. Highly photosensitive properties of CdS thin films doped with boron in high doping levels. Mater Lett, 85: 135-137.

Chapin DM, Fuller CS, Pearson GL. 1954. A new silicon p-n junction photocell for converting solar radiation into electrical power. J Appl Phys, 25(5): 676-677.

Dushkina NM, Ullrich B, Sakai H, Segawa Y, Hibino K, Eiju T. 2000. Reflection properties of oriented thin CdS films formed by laser ablation. Thin Solid Films, 360: 222-228.

Etgar L. 2013. Semiconductor nanocrystals as light harvesters in solar cells. Mater, 6(2): 445-459.

Flores FM, Zepeda KEN, Cervantes AG, Gallardo S, Galvan JGQ, Hernandez AH, Olvera ML, Torres MZ, Kundriavtsev Y, Lira MM. 2013. Effect of the immersion in $CdCl_2$ and annealing on physical properties of CdS:F films grown by CBD. Journal of Physics and Chemistry of Solids, 74: 611-615.

Fraas L, Partain L. 2010. Solar cells and their applications, second ed. John Wiley & Sons.

Francis LF, Stadler BJH, Roberts CC. 2016. Materials processing: A unified approach to processing of metals, ceramics and polymers. Elsevier.

Giribabu G, Murali G, Amaranatha Reddy D, Liu C, Vijayalakshmi R. 2013. Structural, optical and magnetic properties of Co doped CdS nanoparticles. J Alloys Compd, 581: 363-368.

Gluszak EA. 1996. Growth and properties of chemically deposited CdS thin films.

Goldstein JI, Newbury DE, Echlin P, Joy DC, Romig AD, Lyman CE, Fiori C, Lifshin E. 2012. Scanning electron microscopy and X-ray microanalysis: A text for biologists, materials scientists, and geologists. second ed. Springer.

Green MA, Hishikawa Y, Dunlop ED, Levi DH, Hohl-Ebinger J, Ho-Baillie AWY. 2018. Solar cell efficiency tables (version 51). Progress in Photovoltaics: Research and Applications, 26(1): 3-12.

Hemathangam S, Thanapathy G, Muthukumaran S. 2016. Optical, structural, FTIR and photoluminescence characterization of Cu and Al doped CdS thin films by chemical bath deposition method, 27(7): 6800-6808.

Hodes G. 2002. Chemical solution deposition of semiconductor films. Marcel Dekker.

Kaur K, Lotey GS, Verma NK. 2014. Optical and magnetic properties of Fe-doped CdS dilute magnetic semiconducting nanorods. J Mater Sci Mater Electron, 25(6): 2605-2610.

Kelsall RW, Hamley IW, Geoghegan M. 2005. Nanoscale science and technology. John Wiley & Sons.

Khajuria S, Sanotra S, Ladol J, Sheikh HN. 2015. Synthesis, characterization and optical properties of cobalt and lanthanide doped CdS nanoparticles. J Mater Sci Mater Electron, 26(9): 7073-7080.

Khallaf H, Chai G, Lupan O, Chow L, Heinrich H, Park S, Schulte A. 2009a. In-situ boron doping of chemical-bath deposited CdS thin films. Physica Status Solidi (A) Applications and Materials Science , 206(2): 256-262.

Khallaf H, Chai G, Lupan O, Chow L, Park S, Schulte A. 2009b. Characterization of gallium-doped CdS thin films grown by chemical bath deposition. Appl Surf Sci, 255: 4129-4134.

Kittel C. 2005. Introduction to solid state physics, eighth ed. John Wiley & Sons.

Klyuev VG, Maiorova TL, Naumov AV, Semenov VN. 2005. Luminescence and electrical properties of CdS films doped with potassium and sodium. J Appl Spectrosc, 72(4): 552-557.

Klyuev VG, Maiorova TL. 2007. Effect of alkali-metal doping on photoluminescence of CdS films. Journal of Applied Spectroscopy, 74(3): 402-407.

Kumar V, Suriakarthick R, Gopalakrishnan R, Hayakawa Y. 2017. Enhanced electrical and optical properties of CdS:Na thin films by photochemical deposition. Journal of Crystal Growth 468: 208-211.

Lee JH, Yi JS, Yang KJ, Park JH, Oh RD. 2003. Electrical and optical properties of boron doped CdS thin films prepared by chemical bath deposition. Thin Solid Films, 431-432(03): 344-348.

Lee J. 2004. Raman scattering and photoluminescence analysis of B-doped CdS thin films. Thin Solid Films, 451-452: 170-174.

Liu K, Zhang JY, Wu X, Li B, Li B, Lu Y, Fan X, Shen D. 2007. Fe-doped and (Zn, Fe) co-doped CdS films: Could the Zn doping affect the concentration of Fe^{2+} and the optical properties? Physica B, 389(2): 248-251.

Lokhande CD, Pawar SH. 1982. Optical and transport properties of chemical bath deposited CdS: Al films. Solid State Communications, 44(8): 1137-1139.

Lyman CE, Newbury DE, Goldstein J, Williams DB, Romig AD, Armstrong J, Echlin P, Fiori C, Joy DC, Lifshin E, Peters KR. 1990. Scanning electron microscopy, X-ray microanalysis, and analytical electron microscopy: A laboratory workbook.

Mageswari S, Dhivya L, Palanivel B, Murugan R. 2012a. Structural, morphological, optical and electrical properties of spray deposited ternary CdZnS thin films. International Journal of Thin Films Science and Technology, 24(1): 17-24.

Mageswari S, Dhivya L, Palanivel B, Murugan R. 2012b. Structural, morphological and optical properties of Na and K dual doped CdS thin film. Journal of Alloys and Compounds, 545: 41-45.

Mayorova TL, Klyuev VG, Bezdetko JS. 2014. Photoconductivity of CdS films, undoped and doped with alkali-metal impurity ions. Semiconductors, 48(7): 864-867.

Muthusamy M, Muthukumaran S, Ashokkumar M. 2014. Composition dependent optical, structural and photoluminescence behaviour of CdS:Al thin films by chemical bath deposition method. Ceramics International, 40(7): 10657-10666.

Narasimman V, Nagarethinam VS, Usharani K, Balu AR. 2016a. Structural, morphological, optical properties of Na and K dual doped CdS thin films. J Alloys and Compd, 545:41-45.

Narasimman V, Nagarethinam VS, Usharani K, Balu AR. 2017. Bromine doping effect on some properties of CdS films. Surface Engineering, 33(3): 175-180.

Nazir A, Toma A, Shah NA, Panaro S, Butt S, Sagar RR, Raja W, Rasool K, Maqsood A. 2014. Effect of Ag doping on opto-electrical properties of CdS thin films for solar cell applications. Journal of Alloys and Compounds, 609: 40-45.

Pandey J, Khare R, Khare S, Singh D. 2015. Solar cell harvesting: Green renewable technology of future. International Journal of Advanced Research in Engineering and Applied Sciences, 4(11): 93-103.

Park M, Han SM. 2015. Enhancement in conductivity through Ga, Al dual doping of ZnO nanofibers. Thin Solid Films, 590: 307-310.

Paudel NR, Wieland KA, Compaan AD. 2012. Ultrathin CdS/CdTe solar cells by sputtering. Sol Energy Mater Sol Cells, 105: 109-112.

Perednis D. 2003. Thin film deposition by spray pyrolysis and the application in solid oxide fuel cells.

Perednis D, Gauckler LJ. 2005. Thin film deposition using spray pyrolysis. Journal of Electroceramics, 14(2): 103-111.

Pitchaimani K, Amalraj L, Muthukumaran S. 2016. Microstructure, optical and structural characterization of $Cd_{0.98}Fe_{0.02}S$ thin films co-doped with Zn by chemical bath deposition method. Physica E: Low-dimensional Systems and Nanostructures, 78: 56-64.

Poornaprakash B, Poojitha PT, Chalapathi U, Subramanyam K, Park SH. 2016. Synthesis, structural, optical, and magnetic properties of Co doped, Sm doped and Co^{+} Sm co-doped ZnS nanoparticles. Physica E, 83(): 180-185.

Ravichandran K, Senthamilselvi V. 2013. Effect of indium doping level on certain physical properties of CdS films deposited using an improved SILAR technique. Appl Surf Sci, 270: 439-444.

Richter A, Benick J, Feldmann F, Fell A, Hermle M, Glunz SW. 2017. N-type Si solar cells with passivating electron contact: Identifying sources for efficiency limitations by wafer thickness and resistivity variation. Sol Energy Mater Sol Cells, 173(May): 96-105.

Rmili A, Ouachtari F, Bouaoud A, Louardi A, Chtouki T, Elidrissi B, Erguig H. 2013. Structural, optical and electrical properties of Ni-doped CdS thin films prepared by spray pyrolysis. J Alloys Compd, 557: 53-59.

Sai H, Matsui T, Koida T, Matsubara K, Kondo M, Sugiyama S, Katayama H, Takeuchi Y, Yoshida I. 2015. Triple-junction thin-film silicon solar cell fabricated on periodically textured substrate with a stabilized efficiency of 13.6%. Appl Phys Lett, 106(21): 30-34.

Sandoval U, Torres M, Jimenez J, Gonzalez N. 2013. Optical and structural characterization of Li-doped CdS nanoparticles. MRS Proceedings, 1509: mrsf12-1509-cc03-37.

Sayigh AAM. 1977. Solar energy engineering. Academic Press INC.

Sekhar H, Kumar YR, Rao DN. 2015. Preparation, structural and linear optical properties of Zn doped CdS nanopowders. IOP Conference Series: Materials Science and Engineering, 73: 012079.

Selvan G, Abubacker MP, Balu AR. 2016. Structural, optical and electrical properties of Cl-doped ternary CdZnS thin films towards optoelectronic applications. Optik: International Journal for Light and Electron Optics, 127(12): 4943-4947.

Shah NA, Sagar RR, Mahmood W, Syed WAA. 2012. Cu-doping effects on the physical properties of cadmium sulfide thin films. Journal of Alloys and Compounds, 512(1): 185-189.

Shockley W, Queisser H.J. 1961. Detailed balance limit of efficiency of P-N junction solar cells. Journal of Applied Physics, 32: 510-519.

Sivaraman T, Balu, AR, Nagarethinam VS. 2014. Effect of magnesium incorporation on the structural, morphological, optical and electrical properties of CdS thin films. Mater Sci Semicond Process, 27: 915-923.

Sivaraman T, Narasimman V, Nagarethinam VS, Balu AR. 2015. Effect of chlorine doping on the structural, morphological, optical and electrical properties of spray deposited CdS thin films. Progress in Natural Science: Materials International, 25(5): 392-398.

Sivaraman T, Nagarethinam VS, Balu AR, Usharani K. 2016a. Structural, morphological, optical and electrical properties of CdS thin films simultaneously doped with magnesium and chlorine. Journal of Materials Science: Materials in Electronics, 27(2): 1158-1164.

Sivaraman T, Nagarethinam VS, Balu AR. 2016b. Properties of CdS films doped with magnesium and fluorine. Surface Engineering, 32(8): 596-600.

Stokes DJ. 2008. Principles and practice of variable pressure/environmental scanning electron microscopy (VP-ESEM). John Wiley & Sons.

Vettumperumal R, Kalyanaraman S, Thangavel R. Effect of Er concentration on surface and optical properties of K doped ZnO sol-gel thin films. Superlattices Microstruct, 83: 237-250.

Wang L, Wang XA, Chen R, Wu CY, Yu YQ, Xu J, Hu JG, Luo LB. 2014. Gallium doped n-type $Zn_xCd_{1-x}S$ nanoribbons: Synthesis and photoconductivity properties. Journal of Applied Physics, 115(6): 1-6.

Wu C, Jie J, Wang L, Yu Y, Peng Q, Zhang X, Cai J, Guo H, Wu D, Jiang Y. 2010. Chlorine-doped n-type CdS nanowires with enhanced photoconductivity. Nanotechnology, 21(50): 505203.

Wu D, Jiang Y, Li S, Li F, Li J, Lan X, Zhang Y, Wu C, Luo L, Jie J. 2011. Construction of high-quality CdS:Ga nanoribbon/silicon heterojunctions and their nano-optoelectronic applications. Nanotechnology, 22(40): 405201.

Yan LL, Wang XB, Cai XJ, Li XJ. 2015. Effect of boron-doping on the luminescent and electrical properties of a CdS/Si heterostructure based on Si nanoporous pillar array. J Alloy Compd, 632: 450-455.

Yellaiah G, Hadasa K, Nagabhushanam M. 2013. Structural, optical and irrational studies of Na^+ doped $Cd_{0.8}Zn_{0.2}S$ semiconductor compounds. J Alloy Compd, 581: 805-811.

Yılmaz S. 2015a. The investigation of spray pyrolysis grown CdS thin films doped with flourine atoms. Appl Surf Sci, 357: 873-879.

Yılmaz S, Atasoy Y, Tomakin M, Bacaksız E. 2015b. Comparative studies of CdS, CdS:Al, CdS:Na and CdS:(Al-Na) thin films prepared by spray pyrolysis. Superlattices and Microstruct, 88: 299-307.

Yu PY, Cardona M. 2010. Fundamentals of semiconductors: Physics and materials properties, fourth ed. Springer.

Ziabari AA, Ghodsi FE. 2012. Growth, characterization and studying of sol-gel derived CdS nanocrystalline thin films incorporated in polyethyleneglycol: Effects of post-heat treatment. Sol Energy Mater Sol Cells, 105: 249-262.

VITA

The author was born in Mersin in 1989. After completing his secondary school education in various cities, he moved to Adana and completed his high school education in this city. Then, he continued his education at the University of Gaziantep and received his Bachelor of Science in Physics Engineering in 2014. He began Master of Science on 4 February 2015. He has been working as a research assistant at Adana Science and Technology University since September 2017.

PUBLICATIONS

A. SCI Publications

Yılmaz S, Polat İ, Olgar MA, Tomakin M, **Töreli SB**, Bacaksız E. 2017. Physical properties of CdS:Ga thin films synthesized by spray pyrolysis technique. J Mater Sci Mater Electron, 28(4): 3191-3199.

Yılmaz S, **Töreli SB**, Polat İ, Olgar MA, Tomakin M, Bacaksız E. 2017. Enhancement in the optical and electrical properties of CdS thin films through Ga and K co-doping. Mater Sci Semicond Process, 60: 45-52.

B. Proceedings

Töreli SB, Yılmaz S, Polat İ, Tomakin M, Bacaksız E. 25-27 October 2017. Preparation and characterization of CdS:Ga and CdS:(Ga, K) thin films via spray pyrolysis. 2nd International Mediterranean Science and Engineering Congress (IMSEC 2017), **(Poster Representation)**, Pages: 420-420, Adana/TURKEY.